A sensitivity study for the search for the rare $B^{-} \to \Lambda \overline{p} \nu \overline{\nu}$ decay at the *BABAR* experiment

Robert Seddon

Department of Physics
McGill University
Montreal, Canada

18th February 2015

A thesis submitted to McGill University in
partial fulfilment of the requirements
for the degree of Master of Science

Acknowledgements

With thanks to Steven Robertson for supervision; Racha Cheaib, Dana Lindemann and Sheir Yarkoni for advice and assistance; Anabel Chuinard for editing and proofreading; members of the *BaBar* Leptonic & Semi-leptonic Analysis Working Group for feedback and suggestions; and the *BaBar* collaboration for the *BaBar* experiment and dataset.

Abstract

We present a sensitivity study for the search for the semi-leptonic, flavour-changing-neutral-current decay $B^{-}\rightarrow \Lambda\overline{p}\nu\overline{\nu}$. $B^{-}\rightarrow \Lambda\overline{p}\nu\overline{\nu}$ is expected to be highly suppressed in the Standard Model and thus provides a sensitive probe to test for new physics. A branching fraction for $B^{-}\rightarrow \Lambda\overline{p}\nu\overline{\nu}$ has never been experimentally measured.

The analysis is conducted using data from the *BABAR* particle detector, based at the SLAC National Accelerator Laboratory, California, USA. The *BABAR* dataset comprises approximately 471 million $B\overline{B}$ pairs produced from $e^{-}e^{+} \rightarrow \Upsilon(4S)$ collisions and subsequently $\Upsilon(4S) \rightarrow B\overline{B}$.

Using hadronic tag reconstruction we separate the two B mesons in each event by fully reconstructing one B meson from known hadronic decay modes, we then conduct a search for $B^{-}\rightarrow \Lambda\overline{p}\nu\overline{\nu}$ in the decay of the other B meson. Using Monte-Carlo simulations of $B^{-}\rightarrow \Lambda\overline{p}\nu\overline{\nu}$ we develop a signal selection designed to isolate $B^{-}\rightarrow \Lambda\overline{p}\nu\overline{\nu}$ while suppressing potential background processes.

Data is blinded at later stages of the analysis and we provide a range of possible branching fraction upper limits as a function of the number of data events which might survive the signal selection. Assuming we observe no excess of data events over those predicted by Monte-Carlo, we predict branching fraction upper limits for $B^{-}\rightarrow \Lambda\overline{p}\nu\overline{\nu}$ at the 90% confidence level of 2.64×10^{-5} using the Barlow method and 3.10×10^{-5} using the Feldman-Cousins method.

Abrégé

La thèse propose une étude de sensibilité de la désintégration semi-leptonique à courant neutre et saveur changeante suivante : $B^- \to \Lambda\overline{p}\nu\overline{\nu}$. Le modèle standard prévoit un rapport d'embranchement très faible pour ce canal. Toute déviation par rapport à la prédiction standard pourrait attester de la présence de nouveaux phénomènes physiques. Un rapport d'embranchement pour $B^- \to \Lambda\overline{p}\nu\overline{\nu}$ n'a jamais été mesuré expérimentalement.

L'analyse a été effectuée en utilisant les données produites par le détecteur de particules *BABAR*, basé au laboratoire californien du SLAC aux Etats-Unis. L'ensemble des données de *BABAR* comprend environ 471 million des paires $B\overline{B}$ produites à partir de collisions $e^-e^+ \to \Upsilon(4S)$, la particule $\Upsilon(4S)$ se désintégrant consécutivement selon le canal $\Upsilon(4S) \to B\overline{B}$.

Les deux mésons B sont séparés par tagging hadronique. L'un des mésons est reconstruit entièrement à partir des modes de désintégration hadronique connus. Nous cherchons ensuite la présence de $B^- \to \Lambda\overline{p}\nu\overline{\nu}$ dans la désintégration de l'autre méson B. Des simulations Monte-Carlo nous ont permis de déterminer une sélection du signal optimisée pour ne garder que les événements issus de $B^- \to \Lambda\overline{p}\nu\overline{\nu}$ et rejeter le bruit.

Pour l'analyse, la valeur des observables est masquée pour éviter tout biais. Nous fournissons une gamme de limites supérieures possibles pour le rapport d'embranchement en fonction du nombre d'événements qui satisfont aux critères de sélection du signal. En supposant qu'aucun excès d'événements par rapport à ceux prédits par le Monte-Carlo ne soit observé, il est alors possible de donner des limites supérieures pour le rapport d'embranchement de $B^- \to \Lambda\overline{p}\nu\overline{\nu}$ à une valeur de 2.64×10^{-5} pour un niveau de confiance de 90% en utilisant la méthode Barlow et 3.10×10^{-5} en utilisant la méthode Feldman-Cousins.

Contents

List of Figures

List of Tables

Chapter 1

Introduction

Particle physics is the study of the most fundamental particles and forces in nature. Particle physics seeks to understand, at the most basic level, the composition of the universe and laws that govern the interactions therein.

Modern-day particle physics is described by the *Standard Model*, a theoretical model which explains and predicts the behaviour of particles constituting matter and antimatter. Despite predictive success and passing many extremely demanding experimental tests, the Standard Model is deficient. It does not explain dark matter or dark energy, which together constitute approximately 95% of our universe, it does not incorporate gravity, and it does not fully account for the matter-antimatter asymmetry which allows our matter-dominated universe to exist; it thus fails to answer the most fundamental question: why do we exist? Particle physicists therefore probe particle interactions for departures from the Standard Model, seeking to shed light on areas that the Standard Model does not currently explain.

In this thesis we examine the decay $B^- \to \Lambda\overline{p}\nu\overline{\nu}$. While this decay is expected to occur under the Standard Model, any discrepancy in branching fraction from the Standard Model prediction could be an indicator of new physics. We choose $B^- \to \Lambda\overline{p}\nu\overline{\nu}$ for study as it is predicted by the Standard Model to be highly suppressed, therefore any difference from the branching fraction predicted by the Standard Model will be very conspicuous.

Chapter 2 of this thesis provides an overview of particle physics theory in general as well as that specific to $B^- \to \Lambda\overline{p}\nu\overline{\nu}$ and similar decays. Chapter 3 describes the *BABAR* experiment where the data for this analysis was gathered. Chapter 4 explains the tools we use to conduct our analysis. Chapter 5 describes the signal selection we implement in our search for $B^- \to \Lambda\overline{p}\nu\overline{\nu}$. Chapter 6 includes our results, as well as descriptions of systematic uncertainties. Chapter 7 provides final results and the conclusion.

Chapter 2

Theory

Our current understanding of particle physics is known as the Standard Model (SM). It describes the fundamental particles that make up the matter of our universe, the force carriers that mediate their interactions and the origin of particles' mass. It has proved its validity by passing numerous, very precise tests and through its predictive powers. It is one of the most tested and validated theories in history.

Despite these successes, the SM fails to explain several important observed phenomena. In particular, it does not describe dark matter or dark energy (which constitute approximately 95% of the universe [18]), it does not explain the matter-antimatter asymmetry which permits our matter-dominated universe to exist, it does not incorporate gravity and it does not explain neutrino oscillations or masses. The SM is thus incomplete and particle physicists continue to test its limits and to explore for new physics beyond the SM.

2.1 The Standard Model

The Standard Model is a gauge theory based on the local gauge symmetry $SU(3) \times SU(2) \times U(1)$ [8]. Quantum mechanics tells us that fields can also be interpreted as particles; the particle interpretation of the gauge fields is the gauge bosons, which act as force carriers.

The electroweak force is represented by the symmetry group $SU(2) \times U(1)$ [8]. At high energies the electroweak symmetry is unbroken but at low energies the Higgs mechanism [19] causes spontaneous symmetry breaking, separating the $SU(2)$ group (weak force) from the $U(1)$ group (electromagnetic force). The strong force is represented by the symmetry group $SU(3)$ [8].

The Langrangian that satisfies the symmetries of the SM depends on 19 parameters which define particles and their interactions by specifying particle masses, mixing angles, coupling constants etc [13].

The other fundamental force we observe in nature is gravity. This is normally too weak to have a significant effect at the scale of particle physics experiments and is not included in the SM.

2.1.1 Particles of the Standard Model

The fundamental particles of the standard model are fermions (quarks and leptons), gauge bosons and the Higgs boson. There are also composite particles (hadrons) which are composed of quarks.

Fermions

Fermions are spin-1/2 particles which interact via exchange of spin-1 gauge bosons [18]. There are a total of 12 flavours of fermions which are divided into two groups - 6 leptons and 6 quarks (plus an equal number of antiparticle counterparts which carry opposite quantum numbers).

The leptons are the electron (e^-), the muon (μ^-) and the tau (τ^-), all with an electric charge of -1, and their corresponding neutrinos the electron neutrino (ν_e), the muon neutrino (ν_μ) and the tau neutrino (ν_τ), all with zero electric charge. The quarks are the up (u), down (d), charm (c), strange (s), top (t) and bottom (b). Quarks carry non-integer electric charge, as shown in Table 2.1.

The fermions are arranged into three generations (see Table 2.1), with fermions in one generation having the same properties as those in another generation with the exception of mass. Later generations have higher masses (although the mass hierarchy for neutrinos has not yet been confirmed),

Table 2.1: Fermions of the Standard Model [8]. All fermions also have antiparticle counterparts, e.g. the antiparticle counterpart to the e^- is the e^+, which has the same mass but electric charge +1.

Generation	Leptons				Quarks			
	Flavour	Symbol	Electric charge	Mass (GeV/c^2)	Flavour	Symbol	Electric charge	Mass (GeV/c^2)
1	electron	e^-	-1	0.000511	up	u	+2/3	0.0025
	e neutrino	ν_e	0	~0	down	d	$-1/3$	0.0050
2	muon	μ^-	-1	0.1057	charm	c	+2/3	1.29
	μ neutrino	ν_μ	0	~0	strange	s	$-1/3$	0.10
3	tau	τ^-	-1	0.1777	top	t	+2/3	172.9
	τ neutrino	ν_τ	0	~0	bottom	b	$-1/3$	4.19

thus the first (least massive) generation of charged leptons is stable.

Charged leptons interact via the weak and electromagnetic forces while neutral leptons (neutrinos) interact solely via the weak force. Quarks interact via the electromagnetic, weak and strong forces [18].

Quarks not only carry electric charge but also three colour charges, which are usually referred to as red, green and blue. Like electric charge, colour charge is a conserved quantum number and can be carried by gauge bosons. The phenomenon of “colour confinement” describes the fact that only colour-neutral particles are permitted, hence quarks only exist either in colour-neutral pairs (colour-anticolour) or white triplets (red, green and blue). Leptons, on the other hand, may exist in isolation [18].

Hadrons

Hadrons are composite particles comprising quarks. There are two types of hadrons; mesons, comprising two quarks (a $q\overline{q}$ pair); and baryons, comprising a colour-neutral quark triplet [18]. Due to the number of possible ways of combining quarks there is a large variety of hadrons. Those relevant to this analysis are listed in Table 2.2. Like fermions, all hadrons have antiparticle counterparts.

Table 2.2: Hadrons relevant to this analysis [8]. Like fermions, all hadrons have antiparticle counterparts, e.g. the antiparticle counterpart to the π^+ is the π^-, which has the same mass but quark content $\overline{u}d$ and electric charge -1. Note that the neutral Λ baryon is sometimes written with the symbol Λ^0; Λ (no superscript) is understood to mean Λ^0.

Name	Symbol	Quark content	Electric charge	Mass (GeV/c^2)
Upsilon(4S)	$\Upsilon(4S)$	$b\bar{b}$	0	10.579
B meson	B^+	$u\bar{b}$	+1	5.279
Lambda	Λ	uds	0	1.116
Proton	p	uud	+1	0.938
Pion	π^+	$u\bar{d}$	+1	0.140

Gauge bosons

Gauge bosons mediate interactions between particles. Gauge bosons are quanta of their relevant gauge fields and the number of gauge bosons is equal to the number of generators of the gauge field. Thus, there is one gauge boson for the $U(1)$ group (the photon, γ), three for the $SU(2)$ group ($W^\pm$, Z^0) and eight for the $SU(3)$ group (gluons) [26]. The photon and gluons are electrically neutral and massless, although gluons carry colour charge. The $W^\pm$ carry an electric charge of ±1 and have mass 80.385 GeV/c^2, the Z^0 carries an electric charge of 0 and has mass 91.1876 GeV/c^2 [8].

The photon mediates electromagnetic interactions with an unlimited range. Gluons mediate strong interactions which have a range of approximately 10^{-15} m [25]. Because gluons carry colour charge they mediate interactions only between differently-coloured quarks, although gluons are also capable of interacting with other gluons.

The $W^\pm$ and Z^0 mediate the weak force, which has a range of approximately 10^{-18} m [25]. The weak force acts between fermions and, when mediated by the $W^\pm$, can act between quarks of different flavours (see Section 2.1.2).

The Higgs boson

The gauge symmetries used to construct the SM predict that particles should be massless. This is clearly not what we observe and we thus require a spontaneous symmetry breaking of the electroweak gauge symmetry $SU(2) \times U(1)$. This is achieved via the Higgs mechanism which generates masses for the $W^\pm$ and Z^0 gauge bosons while leaving the photons massless.

The Higgs mechanism requires the existence of the scalar Higgs field which has a non-zero vacuum expectation value of 246 GeV [8]. Fermions undergo Yukawa couplings to the Higgs field which causes them to acquire mass proportional to the vacuum expectation value of the Higgs field.

The Higgs field in turn predicts the existence of another fundamental particle, the Higgs boson. The Higgs boson was discovered at CERN in July 2012 [11] and has a mass of approximately 125 GeV/c^2 [4, 10].

2.1.2 The weak force and flavour-changing-neutral-currents

$W^{\pm}$ gauge bosons are capable of mediating weak force interactions between quarks of different flavours in a process known as *quark mixing*.

For example, Fig. 2.1.1 shows a Feynman diagram for a d quark turning into a u quark via a weak decay.

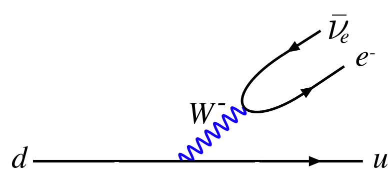

Figure 2.1.1: A flavour-changing-charged-current process involving a d quark becoming a u quark via a weak interaction. This process occurs in beta decay. Note that quarks do not exist in isolation, the d and u quarks must be part of hadrons (a neutron and a proton respectively in the case of beta decay) which are not shown here for the sake of simplicity. Figure adapted from [17].

The process shown in Fig. 2.1.1 is known as a *flavour-changing-charged-current* process because the quark changes flavour (from d to u) and changes electric charge (from $-1/3$ to $+2/3$). As we can see, this is a tree-level process - there are no quantum loops.

The strength of couplings between differently flavoured quarks (and thus the probability of the associated flavour change occurring) is described by the Cabibbo-Kobayashi-Maskawa (CKM) matrix (see Equation 2.1).

$$V_{CKM} = \begin{pmatrix} V_{ud} & V_{us} & V_{ub} \\ V_{cd} & V_{cs} & V_{cb} \\ V_{td} & V_{ts} & V_{tb} \end{pmatrix} \tag{2.1}$$

The coupling constants along the leading diagonal of the CKM matrix are near unity while those further from the diagonal are smaller (see Equation 2.2) [8], thus a flavour-changing process involving, e.g., a $u \to b$ transition is less likely to occur than one involving a $u \to d$ transition.

$$V_{CKM} = \begin{pmatrix} 0.97427 \pm 0.00015 & 0.22534 \pm 0.00065 & 0.00351^{+0.00015}_{-0.00014} \\ 0.22520 \pm 0.00065 & 0.97344 \pm 0.00016 & 0.0412^{+0.0011}_{-0.0005} \\ 0.00867^{+0.00029}_{-0.00031} & 0.0404^{+0.0011}_{-0.0005} & 0.999146^{+0.000021}_{-0.000046} \end{pmatrix} \tag{2.2}$$

A direct transition between differently-flavoured quarks is only possible between quarks of different charges, as shown in the CKM matrix (Eq. 2.1). Thus a process where the quark changes flavour but does *not* change electric charge must involve more than one transition (i.e. more than one CKM matrix element) and thus requires quantum loops.

For example, Fig. 2.1.2 shows Feynman diagrams for a b quark turning into an s quark via two different routes.

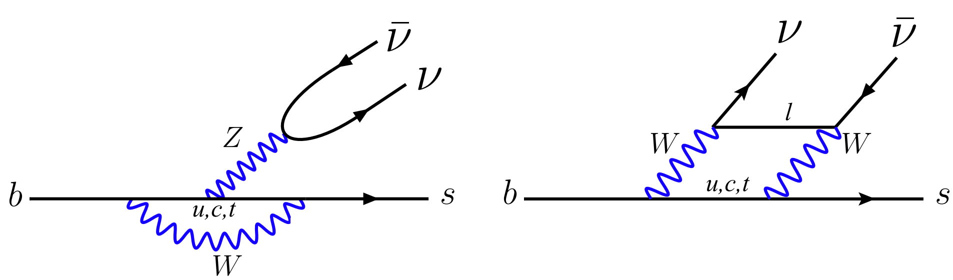

Figure 2.1.2: A flavour-changing-neutral-current (FCNC) process involving a b quark becoming an s quark via a "penguin" diagram (left) and a "box" diagram (right). Neutrinos are necessary to carry away the mass-energy lost in this process. Note that quarks do not exist in isolation, the b and s quarks must be part of hadrons which are not shown here for the sake of simplicity. Figure adapted from [17].

The process show in Fig. 2.1.2 shows a change in flavour (from b to s) but no change in electric charge (both the b and the s carry electric charge $-1/3$), this is therefore known as a *flavour-*

changing-neutral-current (FCNC) process.

We can see that an FCNC decay, where we transition between quarks of different flavours but the same electric charge, must involve higher order loop processes such as those shown in Fig. 2.1.2. Such processes require more than one flavour change, e.g. a $b \to s$ transition might occur via $b \to u$ and then $u \to s$, and also involve several weak force couplings. FCNC processes are thus heavily suppressed (or "rare") and have small branching fractions.

Due to their small branching fractions FCNC decays make excellent probes of the SM and can be used to test for new physics. For example, if there are new physics particles in the loops of FCNC processes (see Section 2.2) they will increase the branching fraction above the value predicted by the SM.

2.2 Physics beyond the Standard Model

Despite the SM's successes in explaining and predicting physical phenomena there are still many unanswered questions. Not least among these is the nature of dark matter, which constitutes a larger fraction of our universe than SM matter.

A potential, although not the only, solution to this problem lies in supersymmetry (SUSY). Supersymmetry models propose that every SM particle has a supersymmetric partner, with SM fermions partnered with superymmetric bosons and SM bosons partnered with superymmetic fermions. SUSY is motivated by an attempt to explain the hierarchy problem, i.e. explain why the weak force is so much stronger than gravity. However, SUSY models also provide a potential avenue to a Grand Unified Theory (unification of the electroweak and strong forces at high energy) and provide potential Dark Matter candidate particles.

The existence of dark matter is implied by, among other things, measurements of the orbits and rotations of galaxies, neither of which match their Newtonian predictions given the amount of luminous matter galaxies are known to contain [8]. Additional non-luminous ("dark") matter is therefore required which interacts gravitationally (but not electromagnetically) and which is massive (to allow it to collect within or near galaxies). Given a lack of evidence for dark matter particles binding to atomic nuclei, they are also believed not to interact via the strong force. It is possible that dark matter particles also do not interact via the weak force, although in this case they would be difficult (or perhaps impossible) to detect. Given our ability to probe the weak sector with our current technology, searches for, and theoretical models of, dark matter particles often work on the hypothesis that they do interact weakly. Consequently, a popular candidate for dark matter particles are the Weakly Interacting Massive Particles (WIMPs).

Further support for WIMPs as viable dark matter candidates stems from the "WIMP miracle". The early universe was in thermal equilibrium, that is, particle-antiparticle pairs were created and annihilated at equal rates thanks to the high energy density of a universe much smaller than today's. As the universe expanded the energy density decreased, breaking thermal equilibrium. Some particle-antiparticle pairs survived into the present day thanks to extremely low self-annihilation cross sections. The WIMP miracle is the observation that the self-annihilation cross section required to provide the amount of dark matter we believe exists today is consistent with a particle that interacts solely via the weak force [16].

There are no particles in the SM which meet the required characteristics of a WIMP. However, SUSY models do provide such candidate particles. The fact that we have not detected any WIMPS yet (or, for that matter, any supersymmetric partner particle) suggests that such particles, if they exist, must be very massive - beyond the reach of our current experiments. However, we are able to search for them indirectly by detecting their contributions as virtual particles in the loops of Feynman diagrams, which will cause measured branching fractions different from those predicted by the SM.

2.3 $B^- \rightarrow \Lambda\overline{p}\nu\overline{\nu}$ - details and motivation

Introduction

Flavour-changing-neutral-current (FCNC) decays such as $B^- \rightarrow \Lambda\overline{p}\nu\overline{\nu}$ [1] offer a sensitive probe of the Standard Model (SM) and an avenue to search for new physics. FCNC decays are suppressed in the SM since they cannot occur at the tree level but can only proceed via one-loop processes. They are therefore very sensitive to new physics occurring at the one-loop level as any deviation from the predicted decay mechanisms (i.e. new physics) will be evident in a branching fraction which has a large deviation from the branching fraction predicted by the SM [17].

This analysis uses data gathered at the *BABAR* particle detector which was based at the SLAC National Accelerator Laboratory. Electrons and positrons provided by the PEP-II accelerator collided at a centre-of-mass energy tuned to the mass of the $\Upsilon(4S)$ resonance which subsequently decayed to $B\overline{B}$ pairs [5]. During the lifetime of the experiment, from 1999 to 2008, *BABAR* collected approximately 471 million $B\overline{B}$ pairs [22].

Physics Motivaton

The decay $B^- \rightarrow \Lambda\overline{p}\nu\overline{\nu}$ is a one-loop, FCNC, semi-leptonic process that proceeds via the penguin- and box-diagrams shown in Fig 2.3.1.

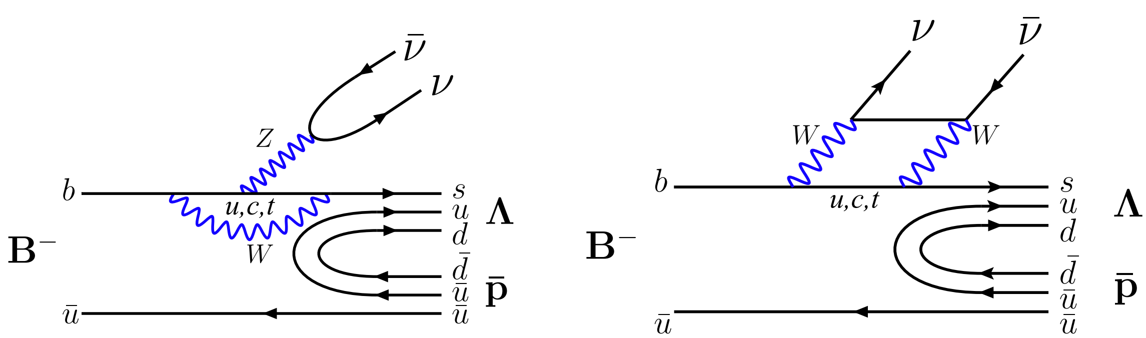

Figure 2.3.1: Feynman diagrams for the decay $B^- \rightarrow \Lambda\overline{p}\nu\overline{\nu}$. Figure adapted from [17].

The $b \rightarrow s$ transition involves off-diagonal Cabibbo-Kobayashi-Maskawa (CKM) matrix elements

[1] Unless explicitly stated otherwise, whenever a decay is given in this paper the charge-conjugate is also implied.

which are much less than one and several weak-force couplings, these processes are therefore heavily suppressed in the SM. Thanks to their common $b \to s\nu\overline{\nu}$ process, $B^{-}\!\to \Lambda\overline{p}\nu\overline{\nu}$ is the baryonic equivalent of $B\!\to K^{(*)}\nu\overline{\nu}$ (see Section 2.3 - Similar studies), which was the subject of a recent *BABAR* analysis [22]. The predicted branching fraction for $B^{-}\!\to \Lambda\overline{p}\nu\overline{\nu}$ is $(7.9 \pm 1.9) \times 10^{-7}$ [17]. An experimentally measured branching fraction different from this would imply new physics occurring at the one-loop level.

The Λ, which has a lifetime of 2.63×10^{-10} s, subsequently decays via $\Lambda \to p\pi^{-}$ with a branching fraction of $(63.9 \pm 0.5)\%$ and via $\Lambda \to n\pi^{0}$ with a branching fraction of $(35.8 \pm 0.5)\%$, all other decays modes have branching fractions of 10^{-3} or less [8].

Decays involving neutrinos, such as $B^{-}\!\to \Lambda\overline{p}\nu\overline{\nu}$, are particularly challenging to analyse because neutrinos cannot be detected, the only evidence of their presence being the missing energy and momentum in an event which they carry away. The $\Lambda \to p\pi^{-}$ mode is especially amenable to study due to the fact that the final state includes three charged tracks ($\overline{p}$ from the B^{-} and $p\pi^{-}$ from the Λ) and two neutrinos (from the B^{-}). Charged tracks are easily detected, thus aiding experimental reconstruction of the decay [17]. We can also use use these charged tracks to reconstruct the Λ, providing us with an extra means with which to suppress background. Any missing energy in the event can be ascribed to the neutrinos. This analysis therefore only studies this $\Lambda \to p\pi^{-}$ decay mode.

The $B^{-}\!\to \Lambda\overline{p}\nu\overline{\nu}$ decay also offers further opportunities for searches for new physics as well as tests of the SM. It is possible to use angular distribution asymmetries to search for beyond-SM right-handed vector and (pseudo-)scalar currents and it is also possible to construct T-odd observables which can be used to test for T-violation [17]. However, such searches would require much more data than is available in the *BABAR* dataset.

Analysis goal

The aim of this study is to act as a sensitivity study for measurement of the upper limit of the branching fraction of $B^{-}\!\to \Lambda\overline{p}\nu\overline{\nu}$. Further work on this analysis, which will take place after completion of this thesis, will involve unblinding the data and publication as a *BABAR* analysis. Although we do not expect to obtain a limit on the order of the theoretically predicted branching fraction, a limit on the branching fraction nevertheless helps place constraints on models of new physics and can serve as a basis for future studies.

Similar studies

$B^- \to \Lambda\bar{p}\nu\bar{\nu}$ has never before been experimentally measured. However, it is closely related to the decays $B \to K^{(*)}\nu\bar{\nu}$ and $B \to K^{(*)}\ell^+\ell^-$. Both of these decays also involve the FCNC $b \to s$ process and both have been the subject of analyses using *BABAR* data [21, 22].

Using the same analysis technique as in this analysis (hadronic B_{tag} reconstruction, see Section 4.1) the *BABAR* analysis of $B \to K^{(*)}\nu\bar{\nu}$ obtained an upper limit on the branching fraction of $B \to K\nu\bar{\nu}$ of 3.2×10^{-5}, with a combined limit (incorporating other analysis techniques) of 1.7×10^{-5} [22]. This contrasts with an SM-predicted branching fraction of $(4.5 \pm 0.7) \times 10^{-6}$ [3].

The gap between the experimental upper limit and the SM prediction in such decays is cited [17] as a motivating factor for investigating $B^- \to \Lambda\bar{p}\nu\bar{\nu}$ as it is possible that in this gap lies new physics, although the experimental limit could of course come down as the result of future analyses.

Analyses of $B \to K^{(*)}\nu\bar{\nu}$ and $B \to K^{(*)}\ell^+\ell^-$ also complement each other as they are sensitive to different Wilson coefficients[2]. $B \to K^{(*)}\nu\bar{\nu}$ and $B^- \to \Lambda\bar{p}\nu\bar{\nu}$ have in common the process $b \to s\nu\bar{\nu}$; their decay amplitudes are thus dependent on $|C^{\nu}_{L,R}|$ [22], the Wilson coefficients for left- and right-handed weak currents which join two quarks to two neutrinos. $B \to K^{(*)}\ell^+\ell^-$, however, proceeds via $b \to s\ell^+\ell^-$ and is thus sensitive to C_7^{eff}, C_9^{eff} and C_{10}^{eff} [21], the Wilson coefficients for the relevant electromagnetic and weak processes via which $b \to s\ell^+\ell^-$ can occur.

Although neither of the analyses $B \to K^{(*)}\nu\bar{\nu}$ or $B \to K^{(*)}\ell^+\ell^-$ observed new physics they did

[2]The Wilson coefficients describe short-distance physics in low-energy weak interactions when the amplitude, A, for such interactions is expressed using the operator product expansion [9, 29]:

$$A = \sum_i C_i(\mu, M_W)\langle Q_i(\mu)\rangle \tag{2.3}$$

where C_i are the Wilson coefficients, Q_i are the local operators (which describe long-distance physics), μ is the chosen renormalisation scale, M_W is the mass of the W boson and where we are summing over operator dimensionality [9].

place constraints on models of new physics. Similarly, if new physics is not present in $B^- \to \Lambda\overline{p}\nu\overline{\nu}$ and the SM theoretical predictions are correct then we do not expect to see any signal as our sensitivity will not be sufficient given the predicted branching fraction; however, results from this analysis can be used to constrain new physics models. $B^- \to \Lambda\overline{p}\nu\overline{\nu}$ also offers several advantages over $B \to K^{(*)}\nu\overline{\nu}$ and $B \to K^{(*)}\ell^+\ell^-$, namely two protons in the final state, allowing us to use more PID tools, and an intermediate particle which we can reconstruct (the Λ), providing an extra avenue for background suppression. These features may also lead to a different final background composition than that found in the analyses of $B \to K^{(*)}\nu\overline{\nu}$ and $B \to K^{(*)}\ell^+\ell^-$.

Chapter 3

The *BABAR* experiment

The *BABAR* particle detector operated at the SLAC National Accelerator Laboratory, California from 1999 to 2008, collecting data from e^+e^- collisions provided by the PEP-II collider. During *BABAR*'s lifetime it collected approximately 471 million $B\overline{B}$ pairs. Originally built to study CP violation in B meson decays, the high integrated luminosity provided by PEP-II allowed *BABAR*'s mission to expand to include precision measurements of the decays of bottom and charm mesons and τ leptons, searches for rare decays and limit-setting for beyond-SM physics.

3.1 The PEP-II asymmetric B-Factory

The decays detected by *BABAR* originated from e^+e^- collisions. The e^+e^- were provided by the 3 km long SLAC linear accelerator (linac) at the SLAC National Accelerator Laboratory, California. The linac accelerated the e^-'s to an energy of 9.0 GeV and the e^+'s to 3.1 GeV. They were then injected into separate storage rings of the PEP-II collider before collision at the interaction point (IP) inside the *BABAR* detector. e^+e^- colliders are well-suited to analysing decays which have missing energy (e.g in the form of neutrinos) because the initial collision energy is known. This is in contrast to hadron colliders where collisions take place between hadron constituents which carry an unknown proportion of hadron momentum.

PEP-II had a design luminsoty of 3×10^{33} cm^{2}s^{-1} and the center-of-mass (CM) energy was tuned to 10.58 GeV, the mass of the $\Upsilon(4S)$ resonance. The $\Upsilon(4S)$ decays into a $B\overline{B}$ pair more than 96% of the time [8]; approximately half of these are B^+B^- and the other half $B^0\overline{B}^0$. PEP-II, along with similar facilities, is thus known as a "B factory".

The large mass of the $B\overline{B}$ pair meant that they were created almost at rest in the CM frame. However, the asymmetric collision energy used meant that the $B\overline{B}$ pair were moving with respect to the lab frame. This motion lead to a greater separation of the B meson decay vertices than if the collision has been symmetric, thus aiding calculation of B meson decay time which is important for measuring time-dependent CP violating processes [5].

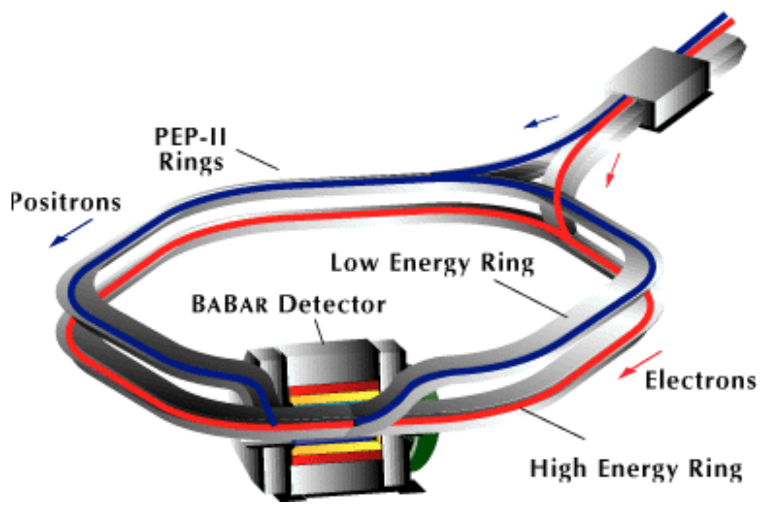

Figure 3.1.1: Diagram of the SLAC linac and PEP-II collider. Figure from [28].

3.2 The *BABAR* detector

The design of the *BABAR* detector was optimised to meet its original physics goals of measuring decays of B mesons into CP eigenstates. Such decays have very small branching fractions (~10^{-4}), and *BABAR* was required to fully reconstruct such decays. This drove the required characteristics of the detector, namely: large and uniform acceptance, good reconstruction efficiency, good momentum resolution, excellent energy and angular resolution, very good vertex resolution, and particle identification (PID) capability over a wide kinematic range [5].

The *BABAR* detector surrounds the PEP-II IP. As shown in Figure 3.2.1 the detector is hexagonal, approximately 3.5 m tall and 7 m long. Due to the asymmetric energy used at PEP-II *BABAR* was offset from the IP by 0.37 m in the direction of the lower energy beam to ensure maximum coverage.

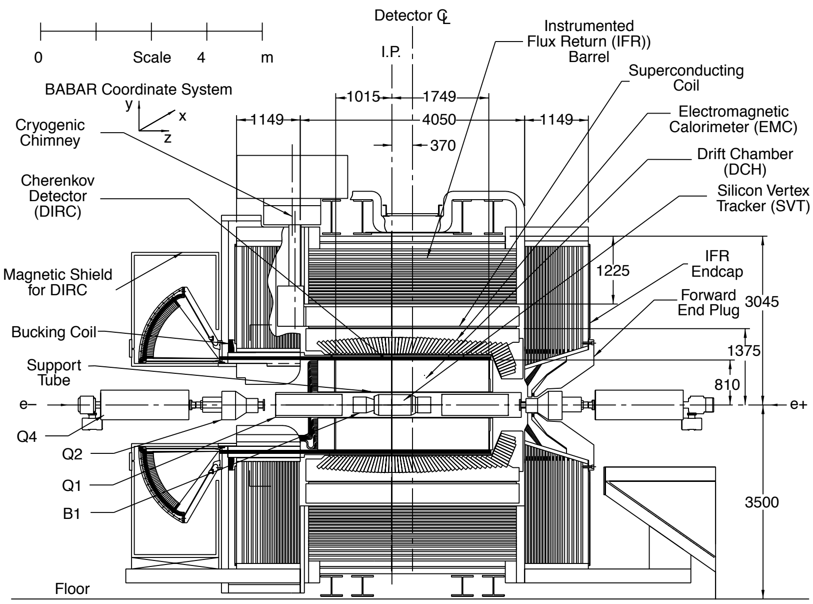

(a) *BABAR detector side view.*

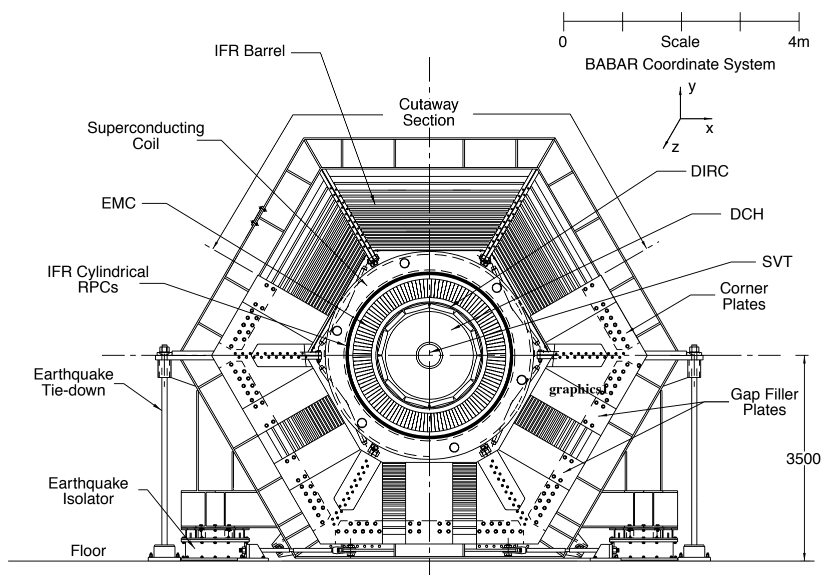

(b) *BABAR detector end view.*

Figure 3.2.1: The BABAR detector. Figure from [5].

The amount of material used in the inner parts of the detector, where tracking and calorimetry takes place, was minimised in order to reduce multiple Coulomb scattering by charged particles (which affects tracking precision) and photon absorption (which affects energy measurements of charged and neutral particles).

The *BABAR* detector is arranged in layers. The innermost parts of the detector are the silicon vertex tracker (SVT) which performs precision tracking of charged particles, the drift chamber (DCH) which measures charged-particle position and momentum, the detector of internally-reflected Cherenkov radiation (DIRC) which performs PID on charged hadrons, and the electromagnetic calorimeter (EMC) which measures particle energy. These are surrounded by a 1.5 T superconducting solenoid which is in turn surrounded by its instrumented flux return (IFR) which detects muons and neutral hadrons.

3.2.1 Silicon vertex tracker

The main purpose of the SVT (along with the DCH) is the accurate reconstruction of charged particle trajectories in order to reconstruct decay vertices. This is achieved by measuring particles' momenta, positions and angles. To provide useful data for CP asymmetry measurements the SVT must achieve resolution of ~80 μm in the z-direction and ~100 μm in the x-y plane. Due to the presence of a strong magnetic field, B meson decay products with low transverse momentum (p_T) curl around inside the SVT, never contacting the DCH or other parts of the detector. The SVT must therefore be capable by itself of providing tracking of particles with p_T of less than 120 MeV/c.

The SVT comprises five layers of double-sided silicon strip detectors. Charged particles traversing the SVT ionise the silicon, creating electron-hole pairs which move within an applied electric field and thus produce a current. This current is measured by ~150,000 readout channels at the ends of the SVT and this information is used to calculate trajectory, and thus momentum, of the particle. To achieve the aforementioned resolution requirements, the resolution of the three inner layers is 10-15 μm while the resolution of the two outer layers is ~40 μm.

The SVT must provide particle trajectory information close to the beam pipe and also tracking information to connect with tracks detected in the DCH. The three inner layers of the SVT are therefore mounted close to the beam pipe while the two outer layers are at a larger radius, close to the DCH. In order to provide 2D positional information the strips on opposite sides of each double-sided strip are orthogonal to each other.

As shown in Figure 3.2.2 the three inner layers are flat while the two outer layers are arch-shaped to provide maximum coverage whilst minimising the amount of silicon required. Layers also partially overlap (see Figure 3.2.2b) to maximise coverage. The total coverage of the SVT is 90% of solid angle in the CM frame and the material is ~4% of a radiation length.

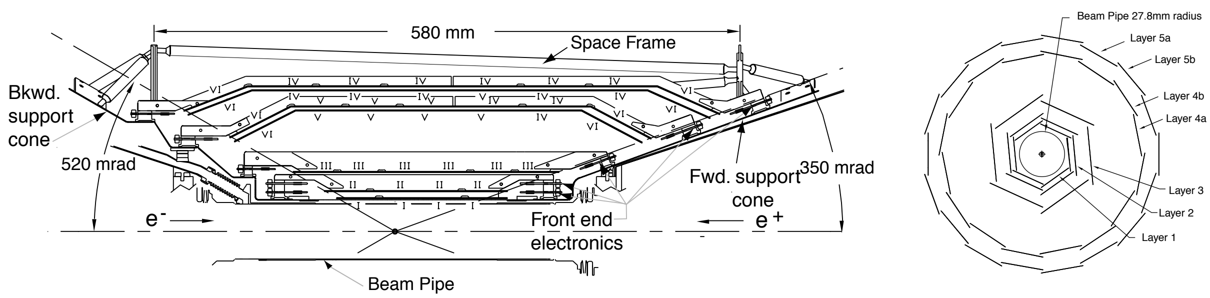

(a) *SVT detector side view. Roman numerals indicate different types of sensor.*

(b) *SVT detector end view.*

Figure 3.2.2: The silicon vertex tracker (SVT) of the BABAR detector. Figure from [5].

3.2.2 Drift chamber

Complementary to the SVT, the DCH measures charged particle momentum and angle to enable reconstruction of decay vertices. For tracks which decay outside the SVT, information from the DCH is the only way to reconstruct such vertices. The DCH must also provide PID capability using ionisation energy losses of charged particles (dE/dx), complementing the PID capability of the DIRC in the barrel region.

As shown in Figure 3.2.3a the DCH is approximately 3 m long, extends up to approximately 80 cm from the beam pipe and is offset from the IP by 37 cm. It comprises 40 layers of hexagonal cells (for a total of 7,104 cells), each delimited by field wires, with a sense wire at their centre and filled with a gas mixture (see Figure 3.2.3b). The DCH thus provides up to 40 measurements for a charged particle with sufficient momentum to pass all the way through. Longitudinal information is obtained by placing wires in 24 out of the 40 layers at a slight angle to the z-axis.

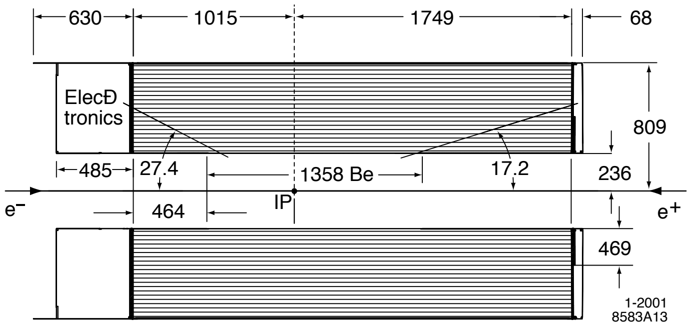

(a) *DCH side view.*

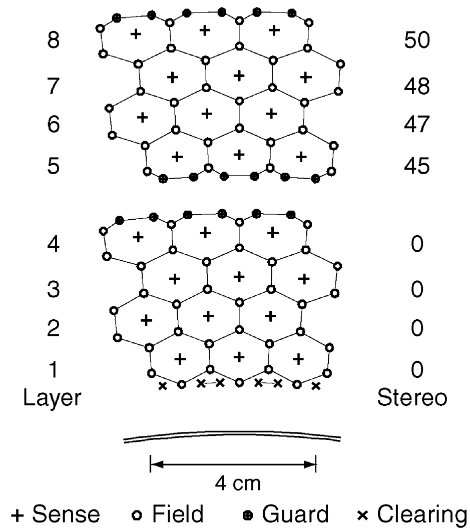

(b) *Two layers of cells within the DCH. Lines have been added between field wires to show the hexagonal shape of the cells. "Stereo" gives the angle, in mrad, between the sense wire and the z-axis.*

Figure 3.2.3: The drift chamber (DCH) of the BABAR detector. Figure from [5].

As charged particles pass through the DCH they ionise the gas inside the cells, liberating electrons and ions. Due to an applied electric field from the field wires, the liberated electrons accelerate towards the sense wire at the centre of each cell, creating an avalanche of secondary electrons and ions as they do so. When this avalanche reaches the sense wire it creates an electrical signal proportional to the energy lost by the original charged particle in the ionisation process. This energy loss measurement, which has a resolution of ~7.5% for high-momentum charged particles passing through all 40 layers, allows us to identify the particle. The DCH provides good K/π separation up to lab-momenta of 0.5 GeV/c and proton identification up to lab-momenta of 1.2 GeV/c. [6]

Due to the generally low momentum of particles resulting from B meson and D-meson decays (usually less than ~1 GeV/c) multiple scattering is a significant challenge to tracking resolution. The DCH is therefore filled with a low-mass medium of an 80:20 mixture of helium and isobutane while the field wires are made of aluminium. The walls of the DCH are also kept thin, helping to match tracks to those detected in the SVT and reducing the effect on the performance of surrounding detectors (DIRC and EMC). The readout electronics are therefore mounted on the backward end-plate of the DCH. These measures result in the DCH constituting only 1.08% of a radiation length.

3.2.3 Detector of internally-reflected Cherenkov radiation

The primary job of the DIRC is to provide π/K separation for tracks with momentum greater than 700 MeV/c up to 4.2 GeV/c (a momentum range in which the DCH does not provide good separation) and also to provide PID for muons with momentum below 750 MeV/c (where the IFR is not effective).

The DIRC is constructed of bars of synthetic fused silica, 4.9 m long, 17 mm thick and 35 mm wide. Bars are grouped into hermetically sealed bar boxes, each box containing twelve bars. There are twelve bar boxes arranged in a dodecagon around the beam pipe for a total of 144 bars. The DIRC has a total thickness of 8 cm, and is 17% of a radiation length.

Particles travelling through the DIRC's silica bars at faster than the local speed of light emit Cherenkov radiation. This radiation is emitted at a Cherenkov angle (θ_c) which is dependent on the speed of the particle. By measuring θ_c (and thus the particle's speed), and with knowledge of the particle's momentum from the inner tracking system we can calculate the particle's mass and thus determine its identity.

Fused synthetic silica was chosen for the bars due to its high index of refraction ($n = 1.473$) (and therefore small Cherenkov angle), resistance to ionising radiation, long attenuation length and low chromatic dispersion in the wavelengths of interest. The DIRC was kept as thin as possible to reduce cost and to reduce negative effects to the energy resolution of the EMC.

In order to reduce the thickness of material in the active region of the detector, the detection equipment for the DIRC is placed outside the active region in a standoff box. Cherenkov radiation emitted inside the DIRC's bars is transmitted to the standoff box via total internal reflection inside the bars, which preserves the angle of emission. The forward end of each bar is mirrored so that Cherenkov radiation emitted in the forward direction will reflect and be collected by the standoff box at the back.

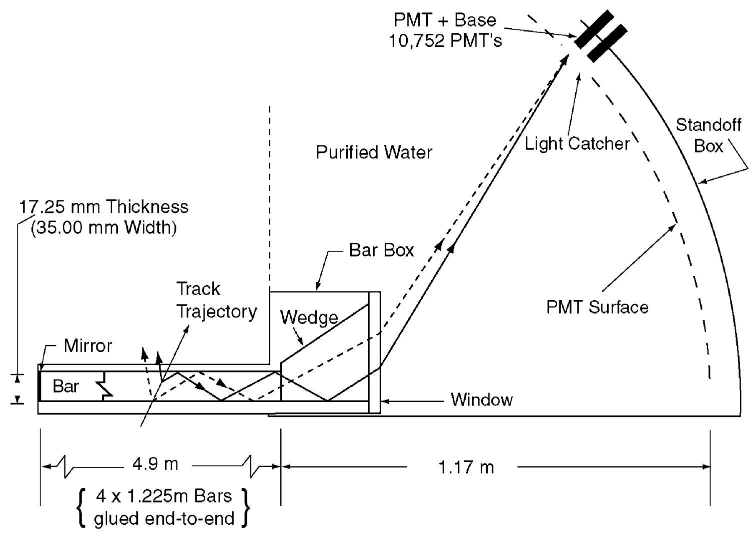

Figure 3.2.4: The detector of internally reflected Cherenkow radiation (DIRC) of the BABAR detector. Figure from [5].

The standoff box is filled with purified water (chosen due to its low cost and similar refractive index to silica) and its back face is covered with photomultiplier tubes (PMTs), approximately 1.2 m from the end of the bars. There are 12 sectors of PMTs each with 896 PMTs. The PMTs detect the Cherenkov radiation and from the shape of the cone of light are able to measure θ_c with a single-photon resolution of ~10 mrad.

3.2.4 Electromagnetic calorimeter

The purpose of the EMC is to measure energy and position of electromagnetic (EM) showers from charged and neutral particles and photons over the energy range 20 MeV to 9 GeV. The EMC is thus the innermost detector capable of detecting neutral particles. The EMC is particularly important for separating electrons from charged hadrons, where the primary discriminating feature is the ratio of EM shower energy to momentum.

As shown in Figure 3.2.5, the EMC consists of an array of thallium-doped caesium-iodide (CsI(Tl)) crystals arranged in a barrel section and a forward endcap section. The crystals are finely segmented to provide accurate position measurements - there are 5,760 crystals in the barrel region arranged in 48 rings and 820 crystals in the endcap arranged in eight rings, together providing 90% solid angle coverage in the CM frame. The crystals are trapezoidal and are longer in the forward direction to ensure containment of showers from high-energy particles. They are approximately 30 cm long, which is approximately 16 radiation lengths.

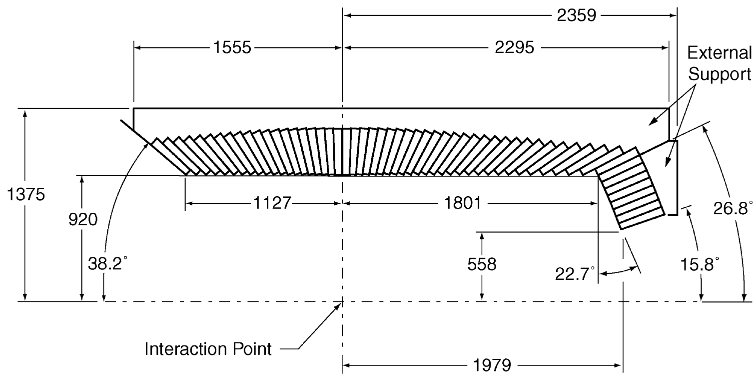

Figure 3.2.5: Crystal layout in the electromagnetic calorimeter (EMC) of the BABAR detector. Figure from [5].

When photons travel through the crystal they undergo pair production, while electrons travelling through the crystal experience Bremsstrahlung resulting in production of photons which themselves undergo pair production. These processes cause an EM cascade (or "shower") which is absorbed by the crystal. The crystal scintillates proportionally to the energy it absorbs. Collection of this scintillation light (which is contained in the crystal thanks to total internal reflection) provides a measure of the energy of the original particle.

CsI(Tl) was chosen due to its high light yield (50,000 γ/ MeV) which provides good energy resolution and small Moliére radius which provides good angular resolution. Its short radiation length also ensures good shower containment in a small size. Crystals are read out individually by photodiodes attached to the rear of the crystals. The energy resolution of the EMC ranges from ~5% at low energies to ~2% at high energies while angular resolution ranges from ~12 mrad at low energies to ~3 mrad at high energies.

3.2.5 Instrumented flux return

The IFR detects muons and neutral hadrons which escape the EMC (mostly K_L^0 and neutrons). It also serves as the flux return for the solenoid.

As shown in Figure 3.2.6a, the IFR is constructed from segmented steel sections arranged in a hexagon around the rest of the detector plus two end caps. The steel is divided into 19 layers (18 for the end caps), the nine inner plates are 2 cm thick, the outer plates 10 cm thick. In the ~3.5 cm gap between plates there are resistive plate chambers (RPCs) or limited streamer tubes (LSTs, introduced at a later date to replace aged RPCs) which detect particles.

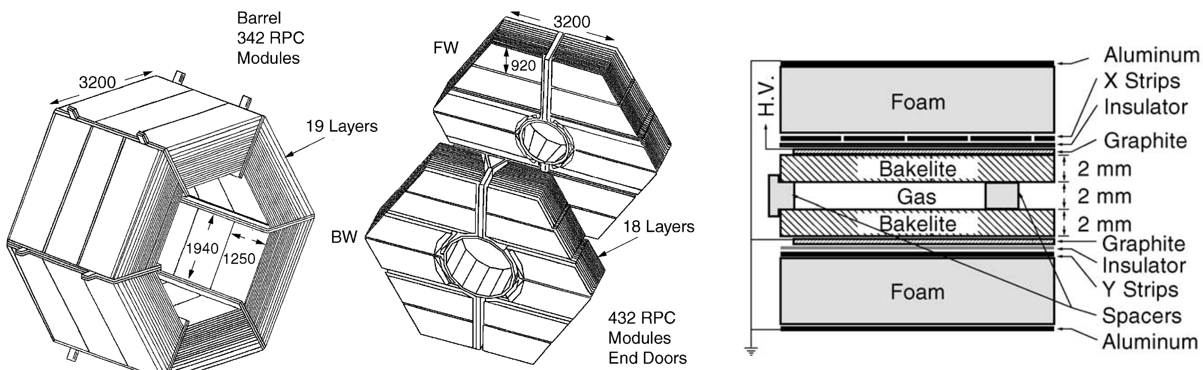

(a) *IFR barrel and end sections.*

(b) *Cross section of an RPC.*

Figure 3.2.6: The instrumented flux return (IFR) and resistive plate chamber (RPC) of the BABAR detector. Figure from [5].

RPCs were chosen due to their low cost, ease of manufacturing in different shapes, fast response time and large signal. As shown in Figure 3.2.6b, the RPCs consist of two 2 mm thick bakelite plates separated by a 2 mm gap filled with a mixture of gases (mostly argon). The external surfaces of the bakelite plates are covered in graphite which is connected to a ~8 kV potential to provide an electric field. Exterior to the graphite plates are aluminium readout strips. Strips on opposite sides of an RPC are perpendicular in order to provide position information. As particles pass through the gas they cause ionisation of the gas, and liberated electrons accelerate due to the applied potential causing an avalanche which is detected by the aluminium readout strips.

Muons penetrate further than neutral hadrons so multiple hits penetrating into the IFR which can be matched to tracks detected in the SVT and DCH are indicative of a muon, while clusters not associated with charged tracks suggest a neutral hadron. The IFR has a muon detection efficiency of close to 90% for the momentum range 1.5-3 GeV/c, K_L^0 detection efficiency ranges from 20% to 40% depending on momentum.

3.2.6 Data collected at *BaBar*

During *BaBar*'s lifetime from 1999-2008 PEP-II delivered a total integrated luminosity of 550 fb^{-1}, of which 524 fb^{-1} were recorded by the *BaBar* detector. From 1999-2007 *BaBar* ran at the $\Upsilon(4S)$ resonance before spending its last few months of operation, in 2008, running at the $\Upsilon(3S)$ and $\Upsilon(2S)$ resonance, as well as at energies above the $\Upsilon(4S)$ resonance. Approximately 471×10^6 $B\overline{B}$ pairs were recorded while running at the $\Upsilon(4S)$ resonance [6].

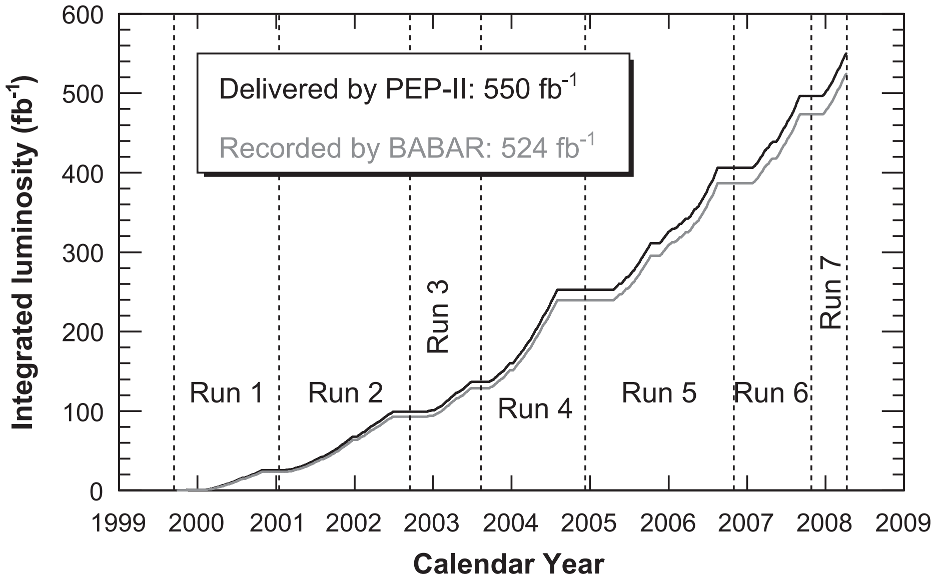

Figure 3.2.7: Integrated luminosity at BaBar during the lifetime of the experiment. Figure from [6].

Chapter 4

Analysis tools and data

4.1 Hadronic B_{tag} reconstruction

This analysis uses a technique known as hadronic B_{tag} reconstruction in order both to significantly reduce background and to provide useful kinematic information in remaining events.

The $\Upsilon(4S)$ decays mostly into $B\overline{B}$ pairs. B mesons have a lifetime of only ~1.6×10^{-12} s and thus decay very quickly via many thousands of hadronic and (semi-)leptonic decay modes. Many of these decay modes have been measured and we can therefore use them reconstruct a B meson from its decay products.

In hadronic tag reconstruction we exclusively and fully reconstruct one of the B mesons from known hadronic decay modes. This B meson is called the B_{tag}. Since the reconstruction of the B_{tag} is a full reconstruction, anything else in the event (charged tracks, clusters, missing energy) can be attributed to the other B meson, known as the B_{sig}. We conduct our analysis work on the decay of the B_{sig}.

Hadronic B_{tag} reconstruction is possible thanks to the fact that in an e^+e^- collider we know the CM energy and there is no pileup background, as there would be in a hadron collider. Furthermore, the $B\overline{B}$ pair is so massive that it is not possible for additional particles to be produced in the same event.

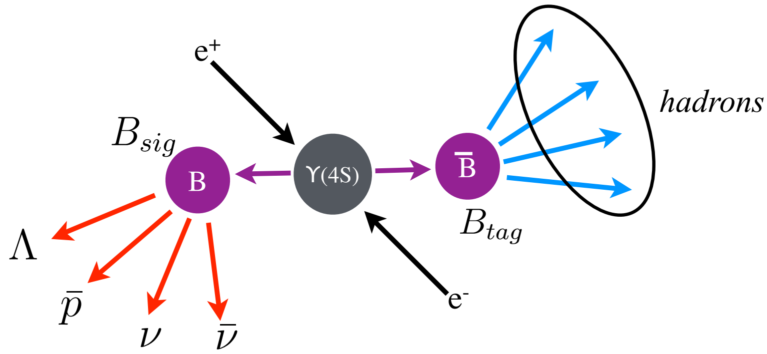

Figure 4.1.1: Cartoon of a signal event with hadronic tag reconstruction.

Since the kinematics (four-momentum) of the B_{tag} are fully known, this also determines the kinematics of the B_{sig} (thus providing us with the B_{sig}'s rest frame) which allows us to place kinematic constraints on the B_{sig}'s daughter particles.

Hadronic B_{tag} reconstruction eliminates a considerable proportion of background (particularly continuum background) compared to an inclusive analysis. It is also especially useful for analysing signal decays which involve missing energy (neutrinos) since it allows us to quantify the energy carried away by the neutrinos.

The disadvantage to using hadronic tag reconstruction is that only a small fraction of events can be reconstructed in this way, and we therefore suffer from low efficiency.

4.2 B_{tag} reconstruction modes

B mesons mostly decay into final states including charmed-mesons. Therefore, to reconstruct B_{tag} candidates, we search for events of the form $B \to D^{(*)\pm}X$ and $B \to D^{(*)0}X$ where [23]

$$X = n_1\pi^{\pm} + n_2K^{\pm} + n_3K_S^0 + n_4\pi^0$$

and

- $n_1 + n_2 \leq 5$
- $n_3, n_4 \leq 2$

- $n_1 + n_2 + n_3 + n_4 \leq 5$

The D candidate (known as a "seed") in $B \to D^{(*)\pm}X$ and $B \to D^{(*)0}X$ is reconstructed from the decays [23]:

- $D^{*0} \to D^0\pi^0$, $D^0\gamma$,
- $D^{*+} \to D^0\pi^+$,
- $D^0 \to K^-\pi^+$, $K^-\ \pi^+\pi^0$, $K^-\pi^+\pi^+\pi^-$, $K^0_S\pi^+\pi^-$, $K^0_S\pi^+\pi^-\pi^0$, K^+K^-, $\pi^+\pi^-\pi^0$, $\pi^+\pi^-$, $K^0_S\pi^0$,
- $D^+ \to K^0_S\pi^+$, $K^0_S\pi^+\pi^0$, $K^0_S\pi^+\pi^+\pi^-$, $K^-\pi^+\pi^+$, $K^-\pi^+\pi^+\pi^0$, $K^+K^-\pi^+$, $K^+K^-\pi^+\pi^0$,
- $D^+_s \to \phi\pi^+$, $K^0_S K^+$,
- $D^{*+}_s \to D^+_s\gamma$.

Once a D-seed has been reconstructed it is combined with the remaining kaons and pions (represented by X) to form a B_{tag} candidate.

The reconstructed B_{tag} is required to have a mass consistent with the known B meson mass and have a centre-of-mass (CM) energy close to half the CM energy of the colliding beams (E_{beam}). Specifically, the B_{tag} candidate must satisfy

$$5.20 \leq m_{\text{ES}} \leq 5.30\ \ \text{GeV}/c^2$$

and

$$-0.2 \leq \Delta E \leq 0.2\,\text{GeV}$$

where m_{ES} is the energy-substituted mass of the B_{tag} defined as

$$m_{\text{ES}} = \sqrt{(E_{beam}/2)^2 - p^2_{B_{\text{tag}}}} \tag{4.1}$$

and where ΔE is defined as

$$\Delta E = E_{beam}/2 - E_{B_{\text{tag}}}$$

It is possible that after these constraints have been imposed that we are left with more than one B_{tag} candidate in an event. In this case we choose the B_{tag} candidate which has the highest B-mode purity (where B-mode purity is the fraction of correctly reconstructed B_{tag} candidates with $m_{\text{ES}} \geq 5.27$ GeV for a specified decay mode as determined from MC simulation). If there is still more than one B_{tag} candidate in an event, the B_{tag} candidate with the lowest value of $|\Delta E\,|$ is chosen.

Reconstructed events are selected by and stored in the *BABAR* skims BSemiExcl and BSemiExclAdd.

4.3 *BABAR* dataset

This analysis only uses data taken at the $\Upsilon(4S)$ resonance (for details on *BABAR* data taking see Section 3.2.6) with a total integrated luminosity of ~ 424 fb^{-1}. The data are split into six runs corresponding to different detector conditions at the corresponding time periods during *BABAR*'s lifetime. Details of the integrated luminosities and B-counts (number of $B\overline{B}$ pairs) for each run are given in Table 4.1.

Table 4.1: Integrated luminosity[1] and B-count (number of $B\overline{B}$ pairs) values for the BABAR dataset. Uncertainties on the B-count values are statistical only.

Run	Data set	Integrated luminosity (pb^{-1})	B-count ($\times 10^6$)
1	Lumi-BSemiExcl-Run1-OnPeak-R24c	20373	22.557 ± 0.005
2	Lumi-BSemiExcl-Run2-OnPeak-R24c	61322	68.439 ± 0.008
3	Lumi-BSemiExcl-Run3-OnPeak-R24c	32279	35.751 ± 0.006
4	Lumi-BSemiExcl-Run4-OnPeak-R24c	99606	111.430 ± 0.003
5	Lumi-BSemiExcl-Run5-OnPeak-R24c	132372	147.620 ± 0.012
6	Lumi-BSemiExcl-Run6-OnPeak-R24c	78308	85.173 ± 0.009

[1] In particle physics, luminosity is number of events (e^+e^- collisions in the case of *BABAR*) per area per time, it thus has dimensions of m^{-2}s^{-1}. For convenience we often use barn in place of metres for specifying area, where 1 b $= 10^{-28}$ m^2, luminosity can thus be expressed in units of b^{-1}s^{-1}. Integrated luminosity is the integral of luminosity with respect to time, i.e. the total number of events per area over a given time period, and can thus be expressed in units of b^{-1}. Barn takes standard SI prefixes, e.g. picobarn (pb).

4.4 Background Monte Carlo simulations

Background Monte Carlo (MC) simulations are used to estimate expected results from the *BABAR* dataset and to estimate background contributions from different sources. Background MC is divided into five different types: B^+B^-, $B^0\overline{B}^0$, $q\overline{q}$ ($q = u$, d, s), $c\overline{c}$ and $\tau^+\tau^-$.

Monte-Carlo techniques use random numbers to simulate particle decays and particle detector responses. In *BABAR*, $B\overline{B}$ events are simulated using EvtGen [20] and $q\overline{q}$, $c\overline{c}$ and $\tau^+\tau^-$ are simulated using JETSET [27]. Particle four-vectors from these generators are then passed through a simulation of the *BABAR* detector based on the Geant4 toolkit [1, 2]. This produces simulated detector responses which are then reconstructed using the same code as is used to reconstruct events in real data.

We consider $c\overline{c}$ events separately from other $q\overline{q}$ events because $c\overline{c}$ events are capable of producing correctly-reconstructed D-meson seed candidates. For $\ell^+\ell^-$ events we only consider the $\tau^+\tau^-$ case due to the fact that τ's can decay hadronically and can thus produce misreconstructed B_{tag} candidates. However, the contribution from $\tau^+\tau^-$ events is generally so small that it is often not visible in histograms.

Each of these five types is further split into six runs, corresponding to different detector conditions at the corresponding time periods during *BABAR*'s lifetime. Each background type for each run is weighted to match data integrated luminosity. The number of generated events, weighting etc. for each type and each run is shown in Table 4.2. Later references to background yield refer to the number of background MC events after weighting to match data integrated luminosity.

4.5 Signal Monte Carlo simulation

A signal Monte Carlo sample is used for this analysis (mode number 11483) which simulates the decays $B^-\to \Lambda\overline{p}\nu\overline{\nu}$ and subsequently $\Lambda \to p\pi^-$, both with a decay fraction of 100%.

A total of 3,358,000 events were generated although 250,000 were lost due to corrupted files leaving 3,108,000 signal events.

Table 4.2: Background Monte Carlo information. For details of skim requirements see Section 4.2. Uncertainties on the skim efficiency values are statistical only.

Run #	Generated events ($\times 10^6$)	Skimmed events	Skim efficiency (%)	Cross-section (nb)	Normalization weight
			B^+B^- Monte Carlo, mode 1235		
1	113.877	42851548	37.63 $\pm$ 0.007	0.5536	0.099
2	340.106	127153897	37.39 $\pm$ 0.004	0.5580	0.101
3	176.806	67104199	37.95 $\pm$ 0.005	0.5538	0.101
4	556.454	210706801	37.87 $\pm$ 0.003	0.5594	0.100
5	724.256	270883359	37.40 $\pm$ 0.003	0.5576	0.102
6	431.176	163900008	38.01 $\pm$ 0.003	0.5438	0.099
			$B^0\overline{B}^0$ Monte Carlo, mode 1237		
1	113.501	39955536	35.20 $\pm$ 0.007	0.5536	0.099
2	349.964	122262783	34.94 $\pm$ 0.004	0.5580	0.098
3	180.262	64089470	35.55 $\pm$ 0.005	0.5538	0.099
4	553.458	195903930	35.40 $\pm$ 0.003	0.5594	0.101
5	761.07	265477026	34.88 $\pm$ 0.002	0.5576	0.097
6	429.68	152373995	35.46 $\pm$ 0.003	0.5438	0.099
			$c\overline{c}$ Monte Carlo, mode 1005		
1	266.961	69604868	26.07 $\pm$ 0.004	1.3	0.100
2	797.386	208169539	26.11 $\pm$ 0.002	1.3	0.101
3	439.931	116096984	26.39 $\pm$ 0.003	1.3	0.097
4	1297.32	346202217	26.69 $\pm$ 0.002	1.3	0.101
5	1677.53	445755971	26.57 $\pm$ 0.001	1.3	0.104
6	1017.42	278228302	27.35 $\pm$ 0.002	1.3	0.101
			uds Monte Carlo, mode 998		
1	166.591	29124036	17.48 $\pm$ 0.003	2.09	0.2584
2	482.575	84856167	17.58 $\pm$ 0.002	2.09	0.2688
3	276.381	49077341	17.76 $\pm$ 0.003	2.09	0.247
4	755.839	136791199	18.1 $\pm$ 0.002	2.09	0.2788
5	1071.84	194428338	18.14 $\pm$ 0.001	2.09	0.2611
6	647.762	121893210	18.82 $\pm$ 0.002	2.09	0.255
			$\tau^+\tau^-$ Monte Carlo, mode 3429		
1	74.665	59325	0.07945 $\pm$ 0.0003	0.94	0.2593
2	215.775	182738	0.08469 $\pm$ 0.0003	0.94	0.2704
3	117.694	100824	0.08567 $\pm$ 0.0003	0.94	0.2609
4	360.242	335622	0.09317 $\pm$ 0.0002	0.94	0.263
5	474.008	469996	0.09915 $\pm$ 0.0001	0.94	0.2655
6	363.346	384601	0.1058 $\pm$ 0.0002	0.94	0.2044

The signal MC simulations were generated using a phase space model. However, there are theoretical predictions for the distributions of four kinematic variables for the decay $B^- \rightarrow \Lambda\overline{p}\nu\overline{\nu}$:

- The invariant mass of the $\Lambda\overline{p}$ pair.

- The invariant mass of the $\nu\bar{\nu}$ pair.

- The angle between the baryon (i.e. the Λ in a B^- decay or the p in a B^+ decay) trajectory in the rest frame of the baryon-antibaryon system and the trajectory of the baryon-antibaryon system in the B meson rest frame.

- The angle between the neutrino (as opposed to the antineutrino) trajectory in the rest frame of the neutrino-antineutrino system and the trajectory of the neutrino-antineutrino system in the B meson rest frame.

The definitions of the angular variables are shown graphically in Figure 4.5.1 and the predicted distributions for all four variables in Figure 4.5.2.

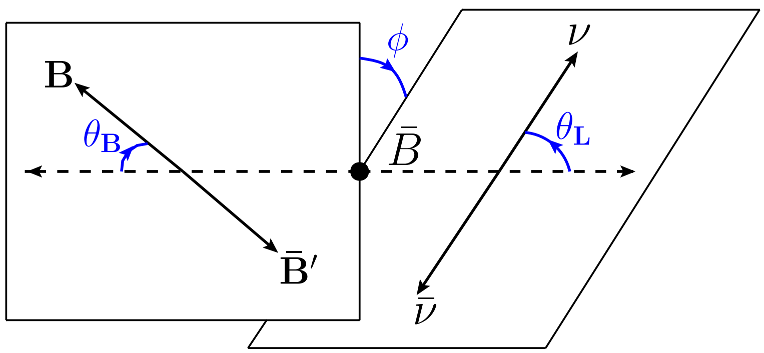

Figure 4.5.1: Definitions of angles used in Figure 4.5.2 where: $\mathbf{B}$ *is the baryon,* $\bar{\mathbf{B}}'$ *is the antibaryon and* $\bar{B}$ *is the* B *meson. Figure from [17].*

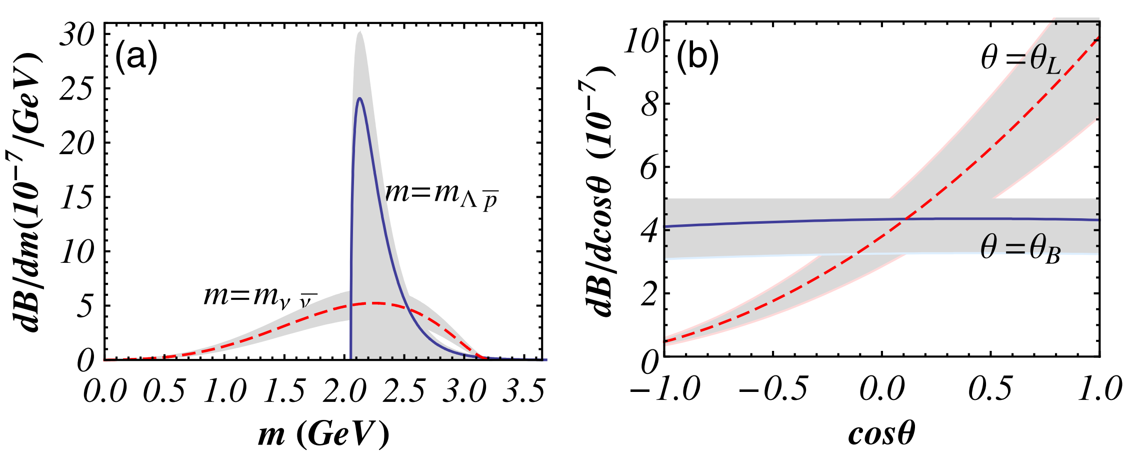

Figure 4.5.2: Predicted distributions of invariant masses and angles for $B^- \to \Lambda\bar{p}\nu\bar{\nu}$ *. Grey areas represent theoretical uncertainties. Figure from [17].*

By reweighting our signal MC it is possible to match these variables' distributions in signal MC to the theoretically-predicted distributions. It was not possible to satisfactorily match all four variables' distributions to their theoretical predictions simultaneously. However, by reweighting each variable independently (i.e. reweighing the signal MC to match the theory distribution of one variable without regard to the distributions of the remaining three variables) we could measure the effect of reweighting to each of the four variables by passing the signal MC through a nominal signal selection process (see Section 5.2) and calculating the final signal efficiency.

It was observed that the signal efficiency only showed a significant change after reweighting the signal MC to match the theoretically-predicted distribution of the $\Lambda\overline{p}$ invariant mass (see Figure 4.5.3). We believe this is due to the fact that the reweighing to the $\Lambda\overline{p}$ invariant mass distribution alters the momenta distribution of the two protons in a signal event (one proton from the Λ, the other from the B_{sig}), as shown in Figure 4.5.4. *BABAR*'s PID selectors are more efficient at lower momenta [6], thus leading to a change (increase) in signal efficiency after running reweighted events through a nominal signal selection.

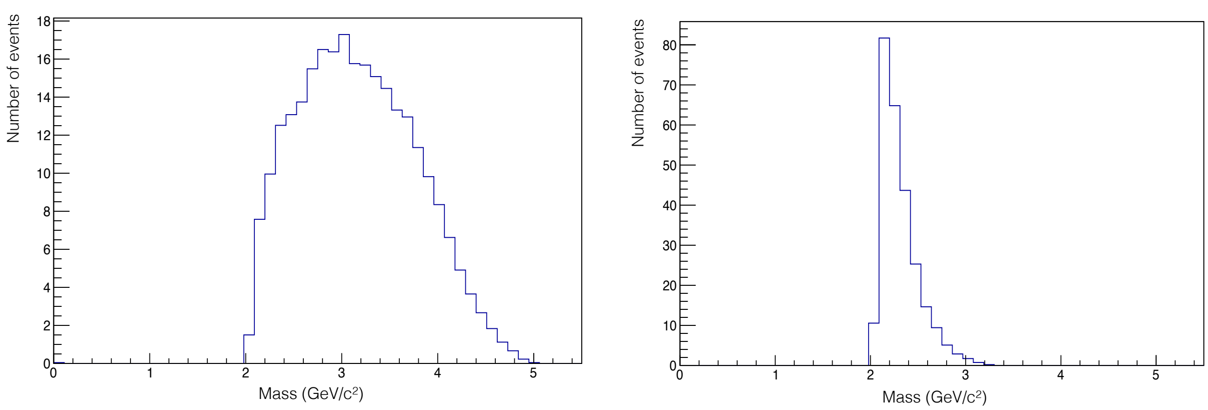

(a) *Before signal reweighting.*

(b) *After signal reweighting.*

Figure 4.5.3: $m_{\Lambda\overline{p}}$ before and after signal MC reweighting, determined from MC Truth information.

We thus chose to reweight our signal MC only to this variable. Simultaneous reweighting to the $\Lambda\overline{p}$ invariant mass and one other variable (for each of the three remaining variables in turn) caused only a small change in signal efficiency compared to reweighting to $\Lambda\overline{p}$ invariant mass alone. This discrepancy is accounted for as a systematic error (see Section 6.1.1).

In order to perform signal MC phase space reweightings we accessed and used MC truth information.

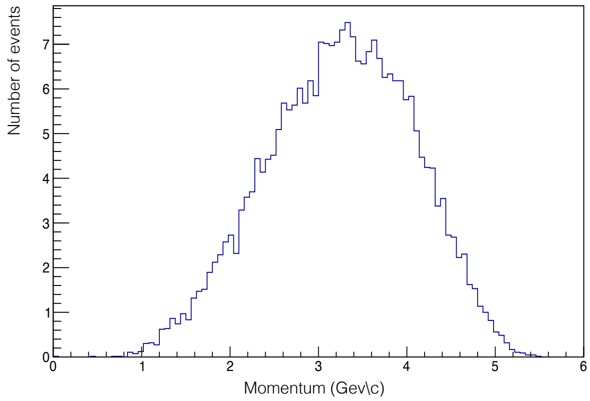

(a) *Before signal reweighting.*

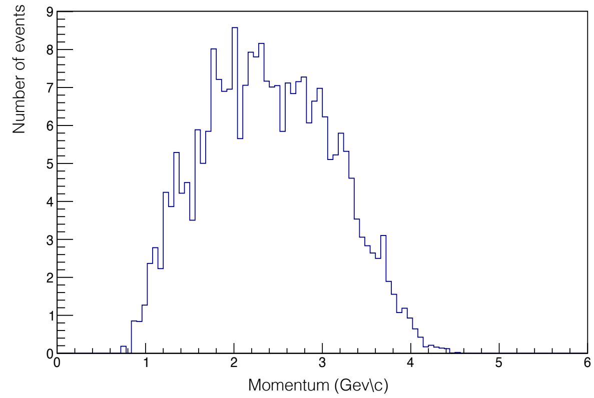

(b) *After signal reweighting.*

Figure 4.5.4: Sum of proton momenta before and after signal MC reweighting, determined from MC Truth information.

During this process it was discovered that approximately 1% of events did not contain the decay $B^{-} \to \Lambda\overline{p}\nu\overline{\nu}$ at the truth level. This is believed to be due to the event simulator simulating events with long-lived particles which interact with detector media before having the opportunity to decay via $B^{-} \to \Lambda\overline{p}\nu\overline{\nu}$. Since such events cannot be reweighted they are excluded from the analysis at the truth level and their exclusion is accounted for as a systematic uncertainty (see Section 6.1.1).

4.6 Local skimming

In addition to the *BABAR* skims mentioned in Section 4.2 we perform an additional local skim at McGill to allow us to work on a dataset more appropriate to our storage and processing capabilities. This will hereafter be referred to as the "local skim". This skim requires:

- $m_{\mathrm{ES}} > 0$,
- B_{tag} must have non-zero charge,
- total charge of B_{sig} daughters must be equal-and-opposite to charge of B_{tag},
- missing energy > 0,
- exactly three charged tracks on the B_{sig}-side.

Note that the local skim removes only events which are either misreconstructed or clearly do not conform to our signal decay and thus these cuts have almost zero effect on signal efficiency. Any signal MC that is removed by these cuts is obviously misreconstructed.

4.7 Blinding

In order to avoid experimenter bias this analysis is performed “blinded” - that is, the signal selection is tested and optimised using Monte Carlo simulations as opposed to real data. For histograms generated at earlier stages of the selection presented in this document data are visible; however, the number of events at these earlier stages means that there is no chance of observing a signal in data and thus no chance of introducing bias. At later stages, where a signal in data might potentially be visible, data are blinded and are not shown in histograms.

Note that we do validate our background MC against data but at a stage of the analysis that is sufficiently early such that there is no chance of observing signal (see Section 5.4).

Chapter 5

Analysis method

A note on plots

The majority of plots in the rest of this document will be of the format shown in Figure 5.1.1; that is, black points with error bars represent the dataset outlined in Section 4.3; solid colours represent MC background normalised to data, as explained in Section 4.4; the red line represents signal MC (with number of events shown by the red axis on the right of the figure) with an assumed branching fraction of 1×10^{-4} and reweighted to match theoretical phase space predictions, as explained in Section 4.5. Note that the assumed branching fraction for signal MC is chosen for convenience and aesthetics of the plots - it does not represent a physics assumption.

5.1 B_{tag} cuts

We make several cuts on the B_{tag} side of the decay to reduce background and separate signal from background. Specifically, we require:

- there is exactly one B_{tag},
- the B_{tag} has charge ± 1,
- the m_{ES} of the B_{tag} is consistent with the known mass of the B meson.

The requirement that the event has one B_{tag} is necessitated by the fact that there are a small number of events which pass skimming despite having zero B_{tag}'s. We require a charged (± 1) B_{tag} because we are looking for a decay from a charged B meson ($B^- \to \Lambda\bar{p}\nu\bar{\nu}$), we can therefore exclude any event with a neutral B_{tag}.

5.1.1 B_{tag} m_{ES} cut

To calculate the mass of the B_{tag} we use m_{ES}, as defined in (4.1), which comprises the CM 3-momentum of the B_{tag} and the CM energy of the beam (E_{beam}). We use E_{beam} instead of the energy of the B_{tag} in order to avoid resolution uncertainties in the measurement of $E_{B_{\mathrm{tag}}}$.

Assuming a correct reconstruction, m_{ES} should peak at the nominal B meson mass of 5.279 GeV/c^2. Figure 5.1.1 shows the m_{ES} distribution for both signal MC (red line) and background MC (solid colours), as well as data (black points with error bars).

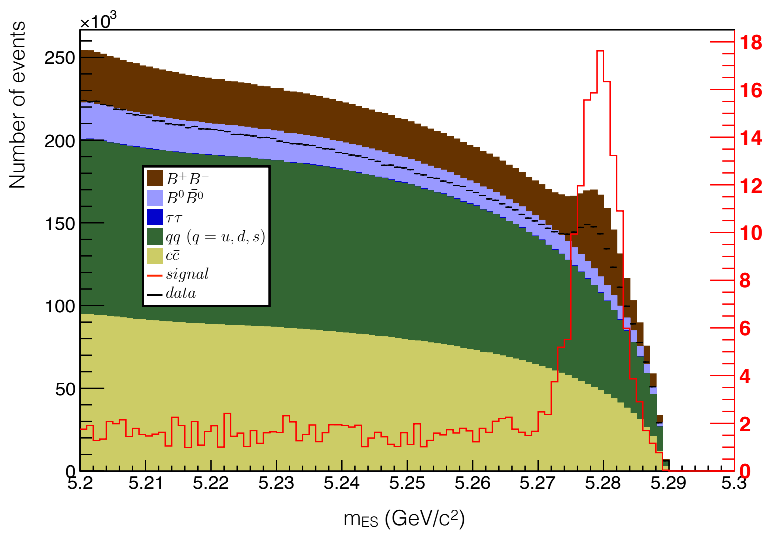

Figure 5.1.1: B_{tag} m_{ES} after hadronic tag reconstruction and after local-skim cuts.

The distributions of the different types of background events can be understood by dividing them into three categories:

- Peaking $B\overline{B}$ background: Events where $\Upsilon(4S) \to B\overline{B}$ and in which a B_{tag} is correctly reconstructed. These events peak in the m_{ES} signal region; however, the B_{sig} does not decay according to the signal decay that we are searching for ($B^- \to \Lambda\bar{p}\nu\bar{\nu}$).

- Non-peaking $B\overline{B}$ background: Events where $\Upsilon(4S) \to B\overline{B}$ and in which a B_{tag} is mis-reconstructed. Since the B_{tag} is mis-reconstructed there is no peak at the B meson mass; these events therefore do not *peak* in the m_{ES} signal region, although they will be *present* in the m_{ES} signal region.

- Continuum background: Events where $e^+e^- \not\to \Upsilon(4S)$ but instead $e^+e^- \to q\overline{q}$ ($q = u,d,s,c$) or $e^+e^- \to \tau^+\tau^-$. The decay products from these events can be mis-reconstructed into a B_{tag}. These events do not *peak* in the m_{ES} signal region, although they will be *present* in the m_{ES} signal region.

Both *non-peaking $B\overline{B}$ background* and *continuum background* are types of *combinatorial background.*

From Figure 5.1.1 we can see that signal events and B^+B^- events peak around the nominal B meson mass. The resolution of this peak is mostly due to variation in E_{beam}. Other background MC events do not peak in the region around the B meson mass and are dominated by continuum events.

For this analysis we choose a nominal B meson mass range of $5.27\ \text{GeV}/c^2 < m_{\text{ES}} < 5.29\ \text{GeV}/c^2$; this is known as the "signal region". Figure 5.1.1 also shows that there is a discrepancy between data and MC background, with the MC background overestimating the number of events. This discrepancy reduces as we make cuts on other variables. Any remaining discrepancy is dealt with at a later stage using an m_{ES} sideband substitution (see Section 5.3) which takes advantage of events in the range $5.20\ \text{GeV}/c^2 < m_{\text{ES}} < 5.26\ \text{GeV}/c^2$ (the "sideband region").

At this early stage of the analysis, after local skim cuts only, we have a total background MC yield of 1.819×10^7 events and a signal efficiency of 0.554%. The data/MC ratio is 0.867. After the B_{tag} m_{ES} cut the background yield is 2.600×10^6 events, signal efficiency is 0.312% and the data/MC ratio is 0.863.

5.1.2 B-mode purity

B-mode purity is defined as the fraction of B_{tag}'s that are correctly reconstructed for a given decay mode. Note that this differs from the conventional definition of "purity" used in particle physics, which is ordinarily a sample characteristic; in our case B-mode purity is a characteristic of a decay mode. To calculate it we examine B^+B^- and $B^0\overline{B}^0$ MC and require [23]:

- $m_{\text{ES}} > 5.273\ \text{GeV}/c^2$,
- between one and three signal-side charged tracks,
- B_{tag} charge is opposite that of total charge of B_{sig}-side tracks,
- B_{tag} charge is neutral for a $B^0\overline{B}^0$ event or charged for a B^+B^- event,
- less than 13 clusters that are not used in B_{tag} reconstruction,
- E_{miss} greater than zero.

The fraction of correctly reconstructed B_{tag}'s within a specific B_{tag} decay mode that pass these requirements is the B-mode purity. Every event can thus be assigned a B-mode purity value based on the B_{tag} decay mode of that event.

Figure 5.1.2a shows the B-mode purity of our data and signal- and background-MC after local skim cuts. At this early stage of the selection B-mode purity provides little discrimination between signal and background, and the usefulness of a cut on B-mode purity is not evident. We thus examined B-mode purity after implementing a partial nominal signal selection (see Figure 5.1.2b). B-mode purity now provides greater discrimination between signal and background. After examining the bin-by-bin ratio of signal to MC (see Appendix A.1) we implemented a cut keeping only events with B-mode purity > 0.4.

Examining a plot of m_{ES} after the B-mode purity cut (see Figure 5.1.3) and comparing with Figure 5.1.1 we can see that there has been a reduction in the number of MC background, MC signal and data events. The proportion of events in the m_{ES} peak comprising B^+B^- events has increased. In the m_{ES} signal region the background yield is now 1.780×10^6 events, signal efficiency is 0.277%

and the data/MC ratio is 0.859.

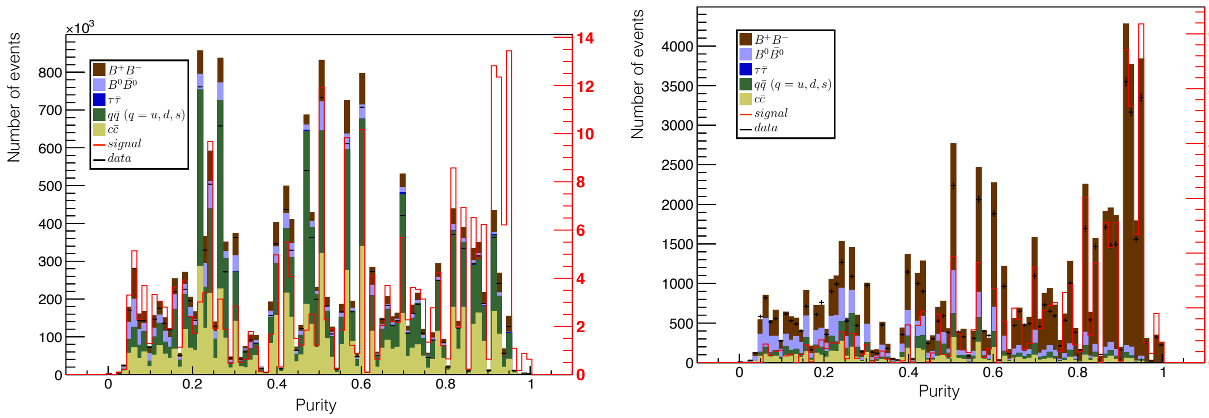

(a) *After local skim cuts only.*

(b) *After cuts on m_{ES}, continuum likelihood and E_{extra} (see Section 5.2 for details).*

Figure 5.1.2: B-mode purity at different stages of the analysis. Note that B-mode purity is a characteristic of each B_{tag} decay mode; thus each event is assigned a B-mode purity value based on the B_{tag} decay mode of that event.

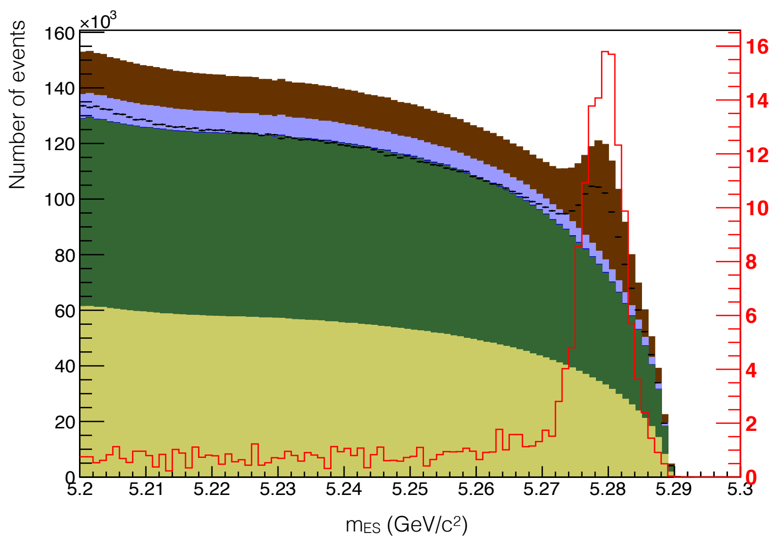

Figure 5.1.3: B_{tag} m_{ES} after local-skim and B-mode purity cuts.

5.2 Signal selection

The B_{tag}-side cuts listed above considerably reduce the amount of background; however, large numbers of events still pass these cuts. We therefore introduce more cuts on the B_{sig}-side to further reduce background.

5.2.1 Continuum suppression

In a $\Upsilon(4S) \to B\overline{B}$ decay the $B\overline{B}$ pair are produced almost at rest due to their large mass; they are also spinless. Due to these factors their decay products tend not to have a preferred direction. Such events thus tend to have spherical shapes, as shown in Figure 5.2.1.

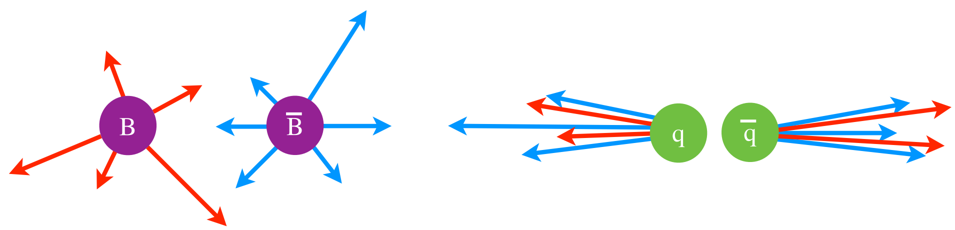

Figure 5.2.1: Cartoons of (left) a $B\overline{B}$ decay and (right) and continuum decay.

On the other hand, in continuum events ($e^+e^- \to q\overline{q}$, $\tau^+\tau^-$) the $q\overline{q}/\tau^+\tau^-$ pair are relatively light and therefore are created with high momentum, causing them to travel back-to-back at high-momentum in the CM frame. Decay and hadronisation products from continuum events thus have jet-like (collimated) shapes with directions preferentially aligned close to the beam.

We can take advantage of this difference in topology to discriminate between the two types of events. To do this we use a multivariate likelihood comprising six variables:

- R2All - the ratio of the 2^{nd} to 0^{th} Fox-Wolfram moments using all charged and neutral particles in the event. A measure of the collimation of an event (i.e. how jet-like it is), R2All ranges from 0 to 1 with 0 representing a "spherical" event and 1 representing a "jet-like" event [15]. Thus, $B\overline{B}$ events tend to have lower R2All values while continuum events tend to have higher R2All values, as shown in Figure 5.2.2a.

- Thrust magnitude - A *thrust axis* is the axis which maximises the longitudinal momenta of a given set of particles. The *thrust magnitude* is the total magnitude of the momenta of the given set of particles along the *thrust axis*. Due to their more spherical shape, $B\overline{B}$ events tend to have lower thrust magnitudes than continuum events, as shown in Figure 5.2.2b.

- $|\cos\theta_{thrust}|$ - The magnitude of the cosine of the angle between the thrust axes of the B_{sig} and the B_{tag}. Since there is no preferred direction for B meson decay products the thrust axes are uncorrelated and have a relatively flat distribution; for continuum events the decay products for the signal-side and tag-side travel in opposite directions, the thrust axes therefore tend to be back-to-back and $\cos\theta_{thrust}$ is thus peaked at 1, as shown in Figure 5.2.2c.

- Thrust$_z$- The magnitude of the z-component of the thrust (i.e. the component parallel to the beam). Due to the aforementioned differences in event shape, continuum events tend to have higher Thrust$_z$ than $B\overline{B}$ events, as shown in Figure 5.2.2d.

- $\cos\theta_B$- The cosine of the angle between the B_{tag} CM three-momentum and the z-axis (beam line). For $B\overline{B}$ events this tends to peak at zero due to the larger angular acceptance in the centre of the detector while it is mostly flat for continuum events, as shown in Figure 5.2.2e.

- $\cos\theta_{p_{miss}}$- The cosine of the angle between all missing CM three-momentum in an event and the z-axis. Missing momentum can be due to undetectable particles (e.g. neutrinos) or particles which are not detected because they travel outside the acceptance of the detector. There is no detector acceptance at small angles, hence $\cos\theta_{p_{miss}}$ peaks at ± 1, as shown in Figure 5.2.2f. However, continuum events peak more strongly at ± 1 as they tend to be at smaller angles to the beam. For signal events p_{miss} should be due to neutrinos (assuming a good B_{tag} reconstruction) so their $\cos\theta_{p_{miss}}$ is flatter.

These variables are used to calculate a multivariate likelihood known as *continuum likelihood* using:

$$\textit{continuum likelihood} = \frac{\prod_i P_{B\overline{B}}(x_i)}{\prod_i P_{B\overline{B}}(x_i) + \prod_i P_{cont}(x_i)} \tag{5.1}$$

where $P_{B\overline{B}}(x_i)$ and $P_{cont}(x_i)$ are probability density functions describing the $B\overline{B}$ and continuum events respectively for the variable x_i [23] and which are calculated only for events with $m_{\text{ES}} > 5.27\,\text{GeV}/c^2$ to ensure that we are working mostly with events with good B meson reconstruction (and thus where the shape variables are physically meaningful). Note that this formula assumes no correlation between the input variables. While this is not completely true, the variables are mostly uncorrelated and continuum likelihood provides very effective separation of continuum

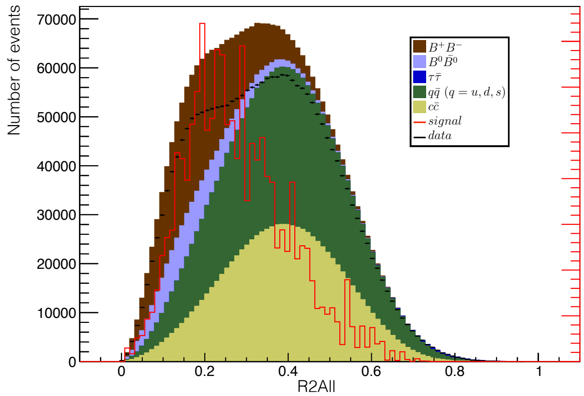

(a) *R2All after local-skim and $B_{\rm tag}$ $m_{\rm ES}$ cuts.*

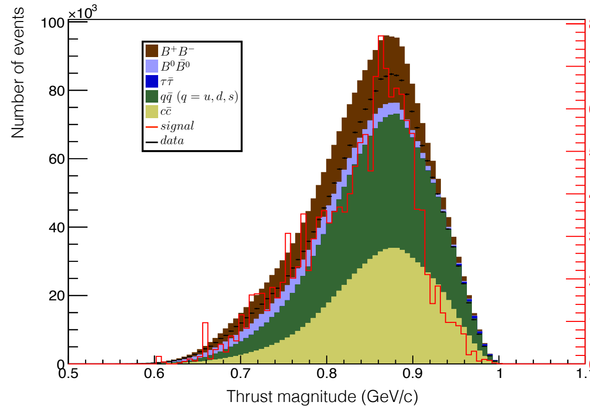

(b) *Thrust magnitude after local-skim and $B_{\rm tag}$ $m_{\rm ES}$ cuts.*

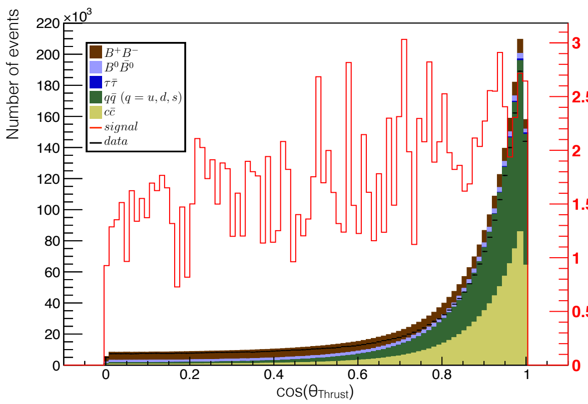

(c) *Cosine of thrust angle after local-skim and $B_{\rm tag}$ $m_{\rm ES}$ cuts.*

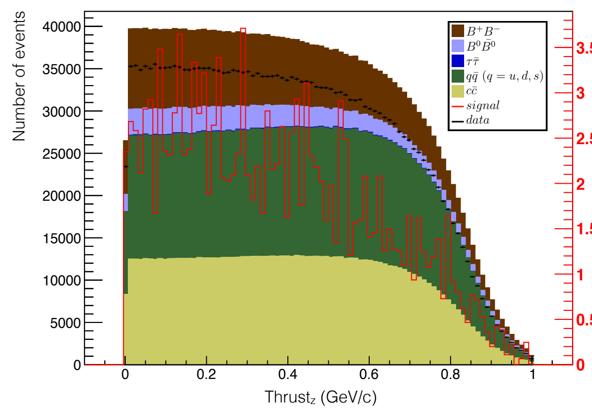

(d) *z-component of thrust after local-skim and $B_{\rm tag}$ $m_{\rm ES}$ cuts.*

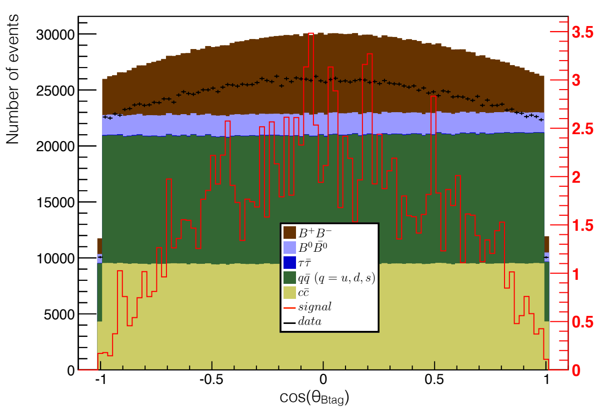

(e) *Cosine of angle between $B_{\rm tag}$ and z-axis (beam) after local-skim and $B_{\rm tag}$ $m_{\rm ES}$ cuts.*

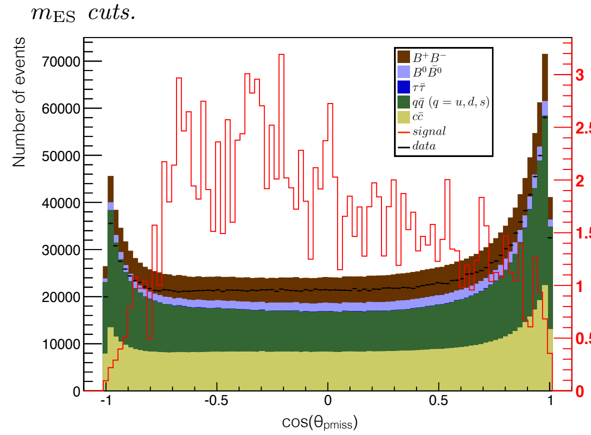

(f) *Cosine of angle between missing momentum and z-axis (beam) after local-skim and $B_{\rm tag}$ $m_{\rm ES}$ cuts.*

Figure 5.2.2: The variables used to calculate continuum likelihood.

and non-continuum events.

As shown in Figure 5.2.3, continuum likelihood for continuum events peaks at 0 while for $B\overline{B}$ events it peaks at 1. By requiring a continuum likelihood value of > 0.65 we can eliminate the majority of our continuum background. While this cut does decrease our signal efficiency, signal events with low continuum likelihood are likely to be misreconstructed anyway, as they do not display the expected topology of a signal event. The value of the cut was chosen by performing a nominal signal selection with different values of the continuum likelihood cut in place and optimising using estimated branching fraction upper limit as a figure of merit (see Appendix A.2 for details).

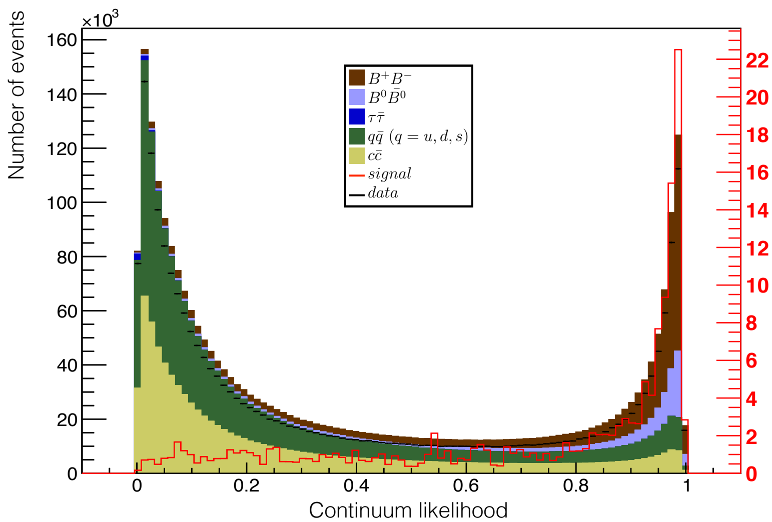

Figure 5.2.3: Continuum likelihood after local-skim and $B_{\rm tag}$ $m_{\rm ES}$ cuts.

Figure 5.2.4 shows $m_{\rm ES}$ after the continuum likelihood cut. As expected, the majority of our continuum background has been eliminated, leaving the $m_{\rm ES}$ peak dominated by B^+B^- events. In the $m_{\rm ES}$ signal region the background yield is reduced by an order of magnitude to 5.127×10^5 events, signal efficiency is 0.185% and the data/MC ratio is 0.850.

5.2.2 Extra energy

Extra energy (E_{extra}) is the sum of the energy of clusters deposited in the EMC that are not associated with charged tracks (in which case they are assumed to originate from neutral particles) and not used in $B_{\rm tag}$ reconstruction. When calculating E_{extra} for MC we adjust cluster energies by

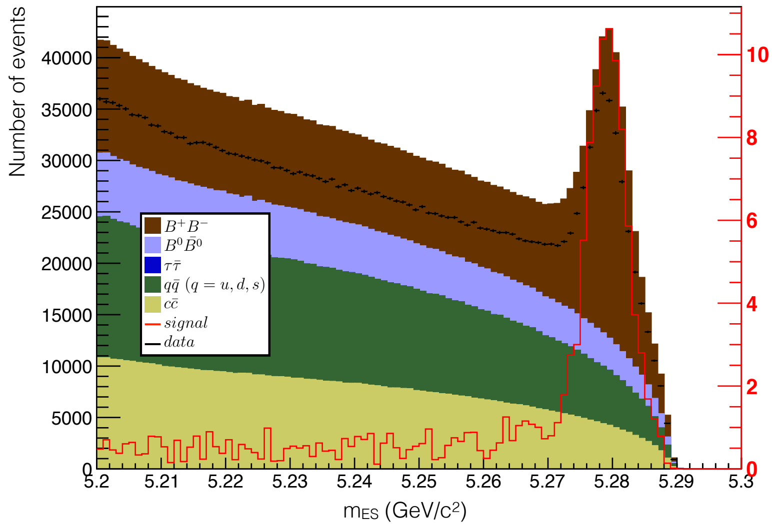

Figure 5.2.4: B_{tag} m_{ES} after local-skim, B-mode purity and continuum likelihood cuts.

-5 MeV with a minimum permitted cluster energy of 0 MeV, based on validation studies which show that this results in improved data/MC agreement (see Appendix B for details). The final state of $B^- \rightarrow \Lambda\overline{p}\nu\overline{\nu}$ does not include any neutral particles and therefore E_{extra} should be zero. However extra energy is expected to be present in signal events, and is observed in signal MC due to:

- Showers in the calorimeter from charged hadrons. When a hadron creates a shower this can lead to multiple energy deposits, some potentially far from the hadron's trajectory. If the reconstruction does not correctly match a cluster up to a charged track, it will be considered as a cluster from a neutral particle. These clusters may be high ($> 100\,\mathrm{MeV}$) or low ($< 100\,\mathrm{MeV}$) energy.

- Mis-assignment of neutral B_{tag} daughters to the B_{sig}. These clusters tend to be low energy and are typically π^0 daughter photons.

- Beam background noise. These clusters tend to be low energy.

For background MC extra energy will be observed from all of the above sources as well as real neutral particles, which tend to produce high energy ($> 100\,\mathrm{MeV}$) clusters.

To calculate E_{extra} we consider all clusters in an event that are not used in the reconstruction of the B_{tag}, that are not associated with charged tracks and that have a lab-frame energy of greater than 50 MeV and we sum their energies in the CM frame. The 50 MeV threshold provides discrimination between signal and background as signal MC clusters tend to be low energy whilst background MC clusters tend to be high energy, for the reasons described above.

As can be seen in Figure 5.2.5, E_{extra} in signal MC peaks at zero, as it should, but there is a large tail of events with non-zero E_{extra}. For background events E_{extra} peaks at $\sim 1.6\,\text{GeV}$. For commentary on the large disagreement between MC and data see Appendix B.

We can see that E_{extra} provides excellent signal-background separation, we therefore only keep events with $E_{extra} < 0.4\,\text{GeV}$. The value of the cut was chosen by performing a nominal signal selection with different values of the E_{extra} cut in place and optimising using estimated branching fraction upper limit as a figure of merit (see Appendix A.3 for details).

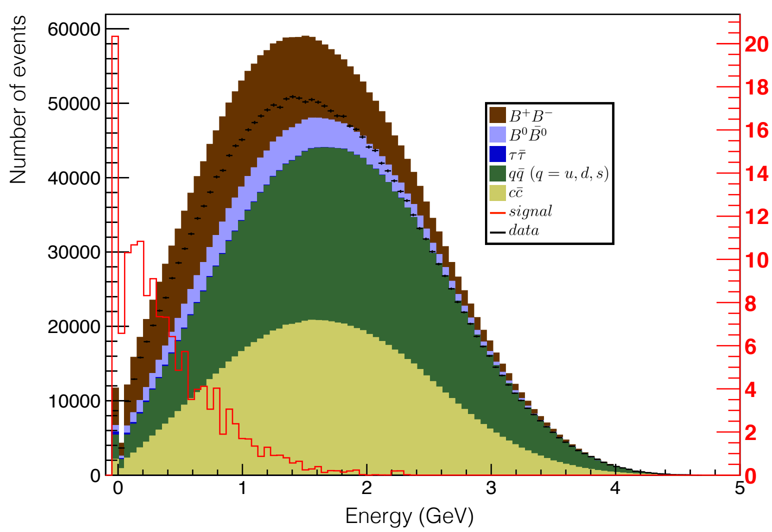

Figure 5.2.5: E_{extra} after local-skim and B_{tag} m_{ES} cuts.

The effects of the cut on E_{extra} can be seen in Figure 5.2.6. In the m_{ES} signal region there has been another order of magnitude reduction in background yield (down to 5.147×10^4 events) and the m_{ES} peak is now even more dominated by B^+B^- events. The signal efficiency is now 0.118%. The agreement between data and MC shows only a slight change, with a data/MC ratio of 0.829 in the m_{ES} signal region (0.844 over the whole m_{ES} range).

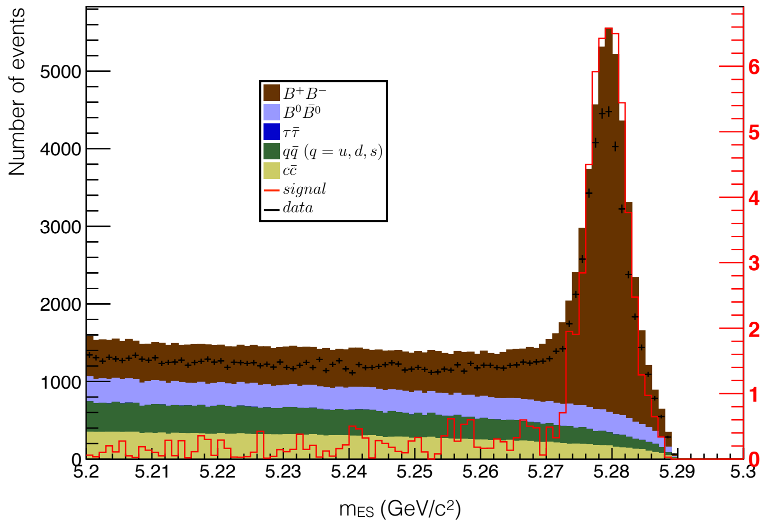

Figure 5.2.6: $B_{\rm tag}$ $m_{\rm ES}$ after local-skim, B-mode purity, continuum likelihood and E_{extra} cuts.

5.2.3 Particle identification

At this stage there are still many background events which pass all of our heretofore-implemented cuts. We therefore use particle identification (PID) selectors to select events which match our signal decay final state.

Charged tracks in *BABAR* are assumed by default to be pions, we therefore do not use pion PID selectors. The other two charged tracks in our signal decay are oppositely-charged protons[1]. We therefore use the proton PID selector KMTightProton to identity protons. KMTightProton is a PID selector based on error correcting output codes [12]. Its detector input is primarily dE/dx measurements from the DCH and at a typical proton momentum of ~1 GeV/c it has a PID efficiency of approximately 95% [6].

We first use KMTightProton to identity a proton track amongst the three charged tracks in our final state. Once a track is ID'ed as a proton, the charge of the track is compared to the charge of the $B_{\rm sig}$. If the proton has the same charge as the $B_{\rm sig}$ it is presumed to be the daughter of the $B_{\rm sig}$; if it has opposite charge as the $B_{\rm sig}$ it is presumed to be the daughter of the Λ.

We then use KMTightProton again on the remaining two charged tracks to identify the other

[1]"Proton" refers to both protons and antiprotons unless explicitly stated otherwise.

proton, which must have charge opposite to that of the previously ID'ed proton. The last remaining charged track, which must have the same charge as the B_{sig}, is presumed to be the pion from the Λ. All three charged tracks are then assigned the appropriate masses corresponding to their ID. Any event which satisfies all of these criteria (PID and appropriate charge) passes the PID cut.

Figure 5.2.7 shows the number (and, in the case of MC background, type) of events passing and failing the PID cut. Figure 5.2.7a shows that the PID cut excludes the vast majority of events which pass the local skim cuts and, as expected (see Figure 5.1.1), our backgrounds at this stage are dominated by continuum events. Figure 5.2.7b shows events passing and failing PID later in the analysis after cuts on m_{ES}, B-mode purity, continuum likelihood and E_{extra}. Although a significant number of continuum background events remain, they now constitute a much smaller proportion of events passing PID, and are approximately equal in number to events coming from $B\overline{B}$ decays.

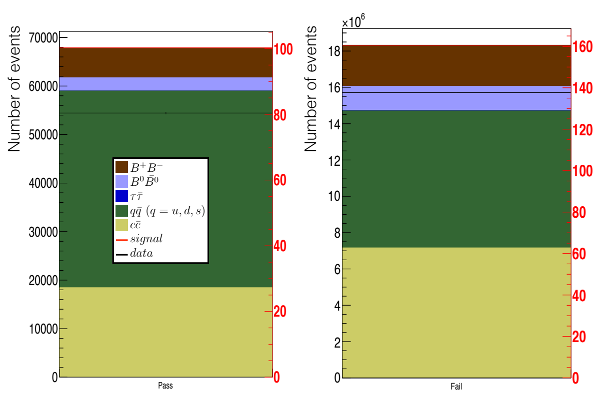

(a) *After local skim cuts only.*

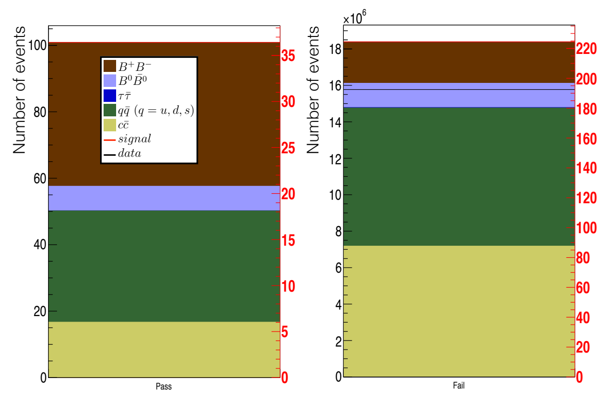

(b) *After m_{ES}, B-mode purity, continuum likelihood and E_{extra} cuts. Note that data has been blinded in the "Pass" bin due to the low number of events.*

Figure 5.2.7: Events, at different stages of the analysis, passing and failing the particle identification (PID) cut. Note the different scales for passing and failing events.

5.2.4 Λ mass reconstruction

We combine the four-momenta of the Λ daughters (the track ID'ed as a proton and which has charge oppose that of the B_{sig}, and the track presumed to be the pion) to recreate the four-momentum of the Λ, from which we extract the Λ mass. The reconstructed Λ mass can be seen in Figure

5.2.8.

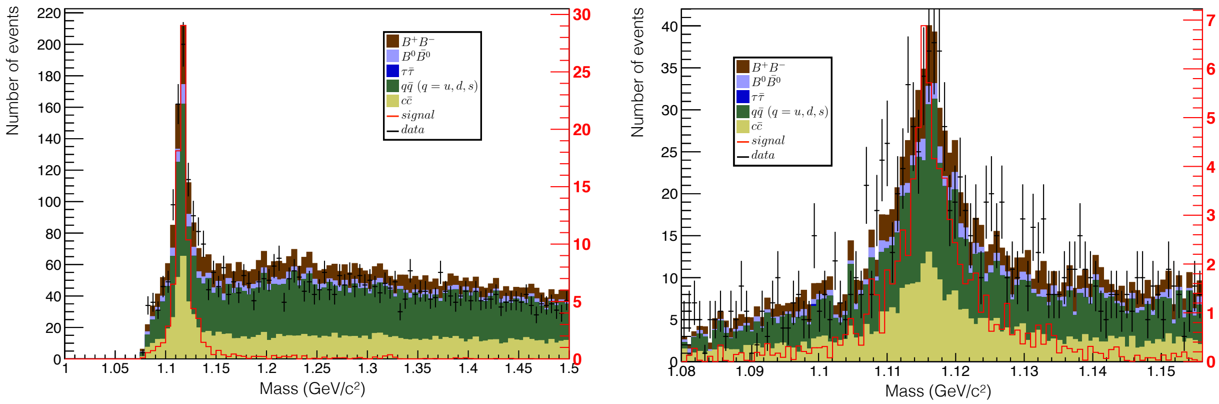

(a) Λ *mass peak with combinatorial tail.*

(b) Λ *mass peak.*

Figure 5.2.8: Λ mass after reconstruction (i.e. PID cut, mass-assignment and four-vector addition) and after local-skim and B_{tag} m_{ES} cuts.

As we can see, both signal and background MC peak strongly around the nominal Λ mass (1.115683 GeV/c^2 [8]). However, there is a small tail to the right of the peak for signal MC and a much larger tail for background MC.

Background events in the Λ mass peak comprise combinatorial background (i.e. non-Λ events which do not *peak* in the Λ mass peak region but are *present* in that region) and background events which contain real Λ baryons and therefore do peak in the Λ mass peak region.

The tail is due to mis-identification by the PID selectors, bad momentum tracking in the detector and, in the case of background MC, the event not containing a real Λ baryon. Since events in the tail do not give realistic Λ masses they are excluded by implementing a Λ mass cut of $1.085\,\text{GeV}/c^2 \leq m_\Lambda \leq 1.151\,\text{GeV}/c^2$. This preserves 98.71% of signal events in the peak region, equivalent to a cut at 2.5σ assuming a Gaussian distribution.

Note that it is possible to reconstruct Λ's using less stringent PID requirements than we have done. These options were investigated but found not to be competitive with the method we use. For more details see Appendix C.

5.2.5 Distance of closest approach

The PID algorithm can be enhanced by implementing a cut on *distance of closest approach* (DOCA). DOCA is the extrapolated distance of closest approach of a charged track to the interaction point (IP). DOCA is not necessarily the closest distance that a particle actually approaches the IP, but the closest it would have come if we trace back its trajectory, hence it is an extrapolated quantity.

DOCA is also not *vertex position*, although it does act as a rough proxy for it. This is due to the fact that displaced vertices from Λ decays can result in charged tracks which do not point back towards the IP (and therefore have higher DOCA values), we can thus use DOCA to discriminate between "real" and "fake" Λ's. We use DOCA instead of vertex position because the vertex position information is not kept during the hadronic B_{tag} reconstruction process.

In general, for our three charged tracks, we would expect the DOCA order to be as follows (see Figure 5.2.9):

- Lowest DOCA: $\overline{p}$ from the B. Because the B decays very quickly the antiproton vertex is very close to the IP and it will therefore usually have the lowest DOCA.
- Middle DOCA: p from the Λ. Because the p is much more massive than the π^- the p will carry away most of the Λ's momentum. When extrapolated backwards the trajectory of the p is therefore likely to approach closer to the IP than that of the π^-.
- Highest DOCA: π^- from the Λ.

We incorporate these requirements into the PID algorithm detailed in Section 5.2.3 by additionally requiring that all three ID'ed particles conform to the above DOCA order. The reconstructed Λ mass after PID-with-DOCA can be seen in Figure 5.2.10.

By comparing with Figure 5.2.8 we can see that incorporating DOCA has led to a significantly reduced number of events in the tail to the right of the Λ mass and the number of background events in the Λ mass peak has also been reduced. Our signal efficiency has also been reduced, evidenced by the smaller number of signal MC events in the Λ mass peak, although by a smaller proportion than background.

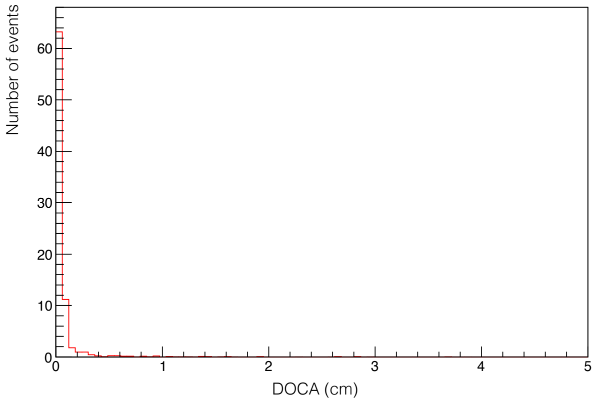

(a) *Proton that is the daughter of the B.*

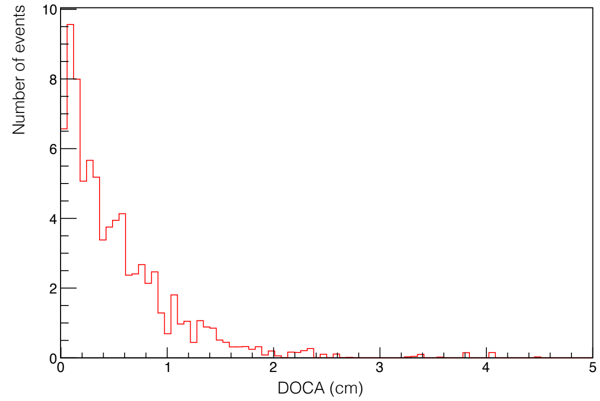

(b) *Proton that is the daughter of the Λ.*

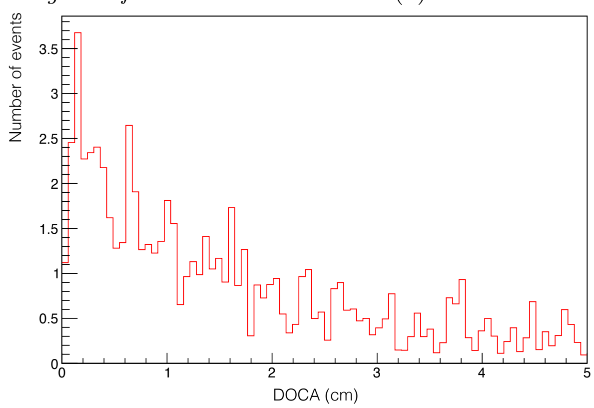

(c) *Pion that is the daughter of the Λ.*

Figure 5.2.9: Distance of closest approach (DOCA) for events in signal MC after local-skim and m_{ES} cuts and Λ reconstruction (excluding incorporation of DOCA information). Particle ID is determined by the PID process described in Section 5.2.3.

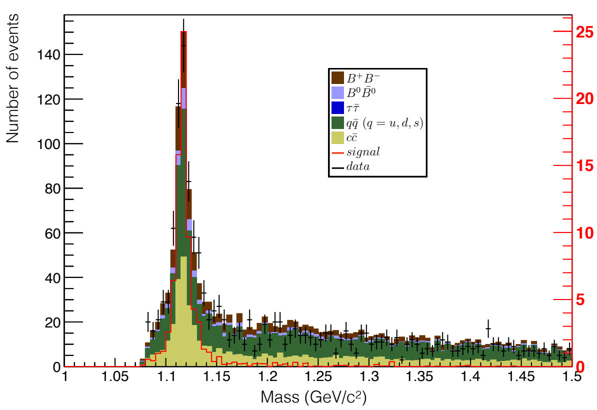

(a) Λ *mass peak with sideband.*

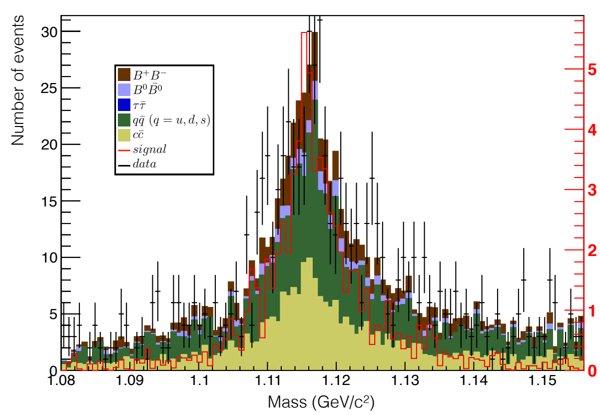

(b) Λ *mass peak.*

Figure 5.2.10: Λ mass after reconstruction and incorporating DOCA information and after local-skim and B_{tag} m_{ES} cuts.

We can quantify the efficacy of incorporating DOCA into our PID cut by examining MC truth-level information. This reveals that incorporating DOCA:

- rejects 63% of MC background events in the Λ-mass peak which do not contain a real Λ,
- retains 79% of MC background events in the Λ-mass peak which do contain a real Λ, and
- increases the percentage of MC background events in the Λ-mass peak which contain a real Λ from 55% to 73%.

Furthermore, the fact that our background is now dominated by real Λ's means that even if vertex position information were available it would not make a significant difference in background suppression.

Figure 5.2.11a shows m_{ES} after implementing the Λ reconstruction (including DOCA and m_Λ cut). Comparing with previous m_{ES} plots we can see that there has been a drastic reduction in the number of background events - in the m_{ES} signal region the background yield is now only 3.56 events; signal efficiency is 0.063%. Due to the low number of events remaining in the selection, data is blinded at this stage; however, we can observe data events in the m_{ES} sideband. As shown in Figure 5.2.11b there is now ~1 event per bin; consequently a data/MC ratio would not be comparable with earlier such measurements and would be rendered meaningless by uncertainties in the number of events.

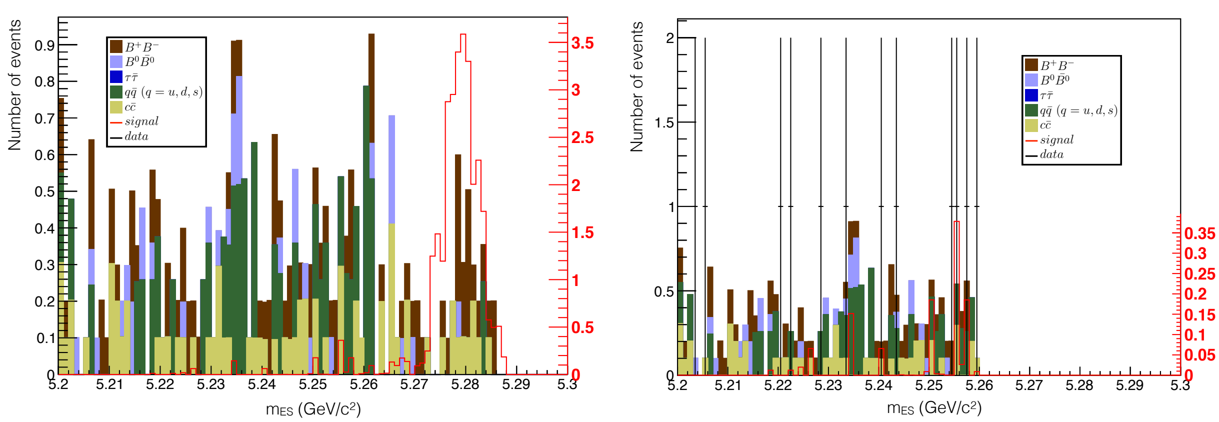

(a) *Full m_{ES} range.*

(b) *m_{ES} sideband only.*

Figure 5.2.11: m_{ES} after local-skim, B-mode purity, continuum likelihood, E_{extra}, Λ reconstruction (incorporating DOCA) and m_Λ cuts.

5.2.6 Momentum transferred to neutrinos

The square of the momentum transferred to the neutrinos in $B^{-} \rightarrow \Lambda\overline{p}\nu\overline{\nu}$ can be quantified as:

$$q^2 = (P_{B_{\mathrm{sig}}} - P_{\Lambda} - P_{\overline{p}})^2 \tag{5.2}$$

where P_x is the four-momentum of particle x. As can be seen in Figure 5.2.12 some events have negative values of q^2. This is clearly non-physical; however, it is mathematically possible to obtain negative values of squared four-vectors if a particle has more momentum than it has energy. For both signal and background MC the cause for this is thought to be misidentification by the PID selectors and/or bad momentum tracking. In either case, when we assign particle masses during the PID stage (see Section 5.2.3) this can result in incorrect/non-physical mass assignments and thus "wrong" values of energy and/or momentum.

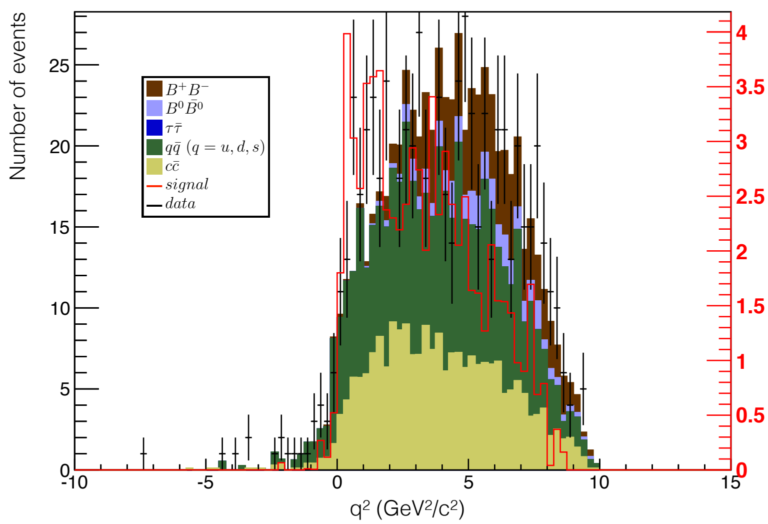

Figure 5.2.12: q^2 after local-skim, B_{tag} m_{ES}, Λ reconstruction (incorporating DOCA) and Λ mass cuts.

Figure 5.2.12 shows that q^2 provides some signal-background discrimination; however, since q^2 represents undetected, and potentially new, physics, cutting on q^2 could have an unknown impact on our sensitivity to new physics. Hence we cut out only those events with $q^2 < -2.3$ GeV$^2/c^2$ and $q^2 > 8.8$ GeV$^2/c^2$.

The cut on q^2 is very minor. After it has been implemented the background yield in the m_{ES} signal region is reduced very slightly to 3.46 events while signal efficiency remains at 0.063%. Figure 5.2.13 shows m_{ES} after implementation.

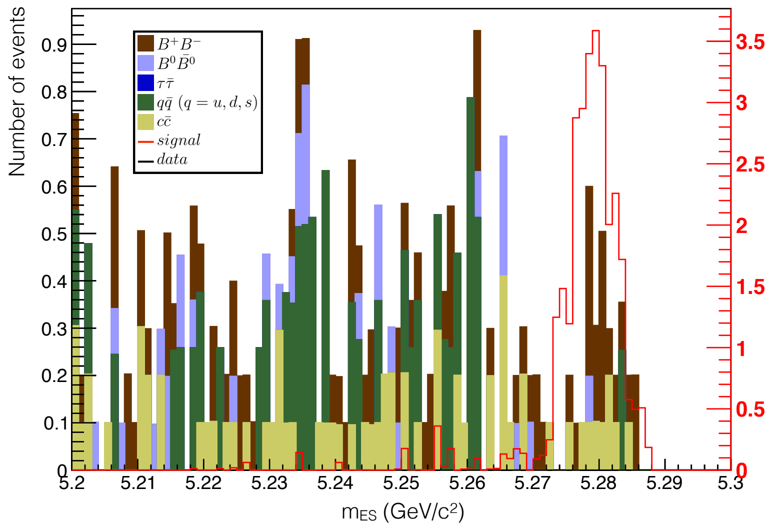

Figure 5.2.13: m_{ES} after local-skim, B-mode purity, continuum likelihood, E_{extra}, Λ reconstruction (incorporating DOCA), m_{Λ} and q^2 cuts.

5.3 m_{ES} sideband substitution

Throughout this analysis there has been a varying level of disagreement between MC background simulations and real data. If we are to make an accurate measurement of a branching fraction limit it is vital that we have a good estimate of the number of background events we should expect in our signal region at the end of the signal selection, and we must be able to make this estimate without observing the number of data events in our signal region. We must therefore compensate for the data/MC disagreement, as the MC clearly does not provide a satisfactory estimate of the number of background events we should expect.

To do this we use an m_{ES} sideband substitution which uses data in the m_{ES} sideband region ($5.20\ \text{GeV}/c^2 < m_{\text{ES}} < 5.26\ \text{GeV}/c^2$) to estimate the expected number of background events in the m_{ES} signal region ($5.27\ \text{GeV}/c^2 < m_{\text{ES}} < 5.29\ \text{GeV}/c^2$).

For the purposes of the m_{ES} sideband substitution, background MC is divided into two types: *peaking background* is background events comprising correctly reconstructed B^+B^- events which peak in the m_{ES} signal region; *combinatorial background* is everything else, i.e misreconstructed and non-peaking B^+B^- plus all $q\overline{q}$, $c\overline{c}$, $\tau^+\tau^-$ and $B^0\overline{B}^0$.

The first step of the m_{ES} sideband substitution is to estimate the combinatorial background contribution in the m_{ES} signal region using sideband data (as opposed to MC events in the signal region). To do this we determine the ratio, R_i, of signal-region to sideband-region MC events for each type of MC background i:

$$R_i = \frac{N_i^{sig}}{N_i^{side}} \tag{5.3}$$

where N_i^{sig} is the number of MC events of type i in the m_{ES} signal region and N_i^{side} is the number of MC events of type i in the m_{ES} sideband region.

This ratio works for all types of MC background except B^+B^-, since B^+B^- events in the signal region comprise both combinatorial and peaking components. For B^+B^- events we therefore assume that the combinatorial B^+B^- component in the signal region has a similar distribution to that of $B^0\overline{B}^0$ and use $R_{B^0\overline{B}^0}$ for both B^+B^- and $B^0\overline{B}^0$. We base this assumption on the similarity in their combinatorial distributions in the sideband region, visible in any m_{ES} plot with sufficient statistics.

To calculate the overall ratio of combinatorial MC sideband-region to signal-region events we must also account for the fraction, F_i, of sideband MC events represented by each MC type i as:

$$F_i = \frac{N_i^{side}}{N_{MC}^{side}} \tag{5.4}$$

where N_i^{side} is the number of sideband-region events of MC type i and N_{MC}^{side} is the total number of MC events of all types in the sideband region.

We can now calculate the ratio, R_{MC}, of combinatorial MC events in the signal region to combinatorial MC events in the sideband region as:

$$R_{MC} = ((F_{B^+B^-} + F_{B^0\overline{B}^0}) \times R_{B^0\overline{B}^0}) + (F_{\tau^+\tau^-} \times R_{\tau^+\tau^-}) + (F_{q\overline{q}} \times R_{q\overline{q}}) + (F_{c\overline{c}} \times R_{c\overline{c}}) \tag{5.5}$$

where R_i and F_i are defined in equations 5.3 and 5.4 respectively. At the end of our signal selection we can now multiply the number of data events in the sideband region by R_{MC} to provide us with a more accurate estimate of the expected number of combinatorial background events in the signal region, N^{comb}_{bkgd}, i.e.:

$$N^{comb}_{bkgd} = R_{MC} \times N^{side}_{Data} \tag{5.6}$$

where N^{side}_{Data} is the number of data events in the sideband region. Note that we are assuming that the MC accurately simulates the shape of the data distribution in the sideband region but may get the total number of events wrong.

Now that the combinatorial background in the signal region has been accounted for, the second step of the m_{ES} sideband substitution is to obtain a better estimate of peaking B^+B^- background in the signal region. This is done by calculating a peaking correction factor, C_{peak}, which corrects for the difference between the number of peaking events in B^+B^- MC and in data. C_{peak} is thus:

$$C_{peak} = \frac{N^{peak}_{Data}}{N^{peak}_{B^+B^-}} \tag{5.7}$$

where

$$N^{peak}_{Data} = N^{sig}_{Data} - N^{sig}_{c\overline{c}} - N^{sig}_{q\overline{q}} - N^{sig}_{\tau^+\tau^-} - \left(N^{sig}_{B^0\overline{B}^0} \times \frac{N^{side}_{Data} - N^{side}_{c\overline{c}} - N^{side}_{q\overline{q}} - N^{side}_{\tau^+\tau^-} -}{N^{side}_{B^0\overline{B}^0}} \right) \tag{5.8}$$

and

$$N^{peak}_{B^+B^-} = N^{sig}_{B^+B^-} - \left(N^{sig}_{B^0\overline{B}^0} \times \frac{N^{side}_{B^+B^-}}{N^{side}_{B^0\overline{B}^0}} \right). \tag{5.9}$$

In words:

- N_{Data}^{peak} is calculated as the number of data events in the signal region minus the number of MC events in the signal region, where we scale up the number of $B^0\overline{B}^0$ MC events in the signal region to account for the fact that we cannot isolate non-peaking B^+B^- MC events from peaking B^+B^- MC events and to compensate for any data/MC disagreement.
- $N_{B^+B^-}^{peak}$ is calculated as the number of B^+B^- MC events in the signal region minus the estimated number of combinatoric B^+B^- MC events, again calculated based on the assumption that combinatoric B^+B^- events have a similar distribution to combinatoric $B^0\overline{B}^0$ events.

At the end of our signal selection we can now multiply the number of peaking B^+B^- MC events (calculated according to Equation 5.9) by C_{peak} to obtain an estimate of the number of expected peaking background events, N_{bkgd}^{peak}, i.e.:

$$N_{bkgd}^{peak} = C_{peak} \times N_{B^+B^-}^{peak} \tag{5.10}$$

Thus, the total estimated number of background events in the signal region, N_{bkgd}^{total}, is:

$$N_{bkgd}^{total} = N_{bkgd}^{comb} + N_{bkgd}^{peak} \tag{5.11}$$

where N_{bkgd}^{comb} is defined in Equation 5.6 and N_{bkgd}^{peak} is defined in Equation 5.10.

In order to decide at which point in the analysis to take the values of R_{MC} and C_{peak}, an m_{ES} sideband substitution was performed after every cut. The values of R_{MC} and C_{peak} as a function of cut are shown in Figure 5.3.1; a plot of B_{tag} m_{ES} after each cut is shown in Figure 5.3.2.

Note that the purpose of the m_{ES} sideband substitution is to allow us to estimate signal-region background without observing the number of data events in the signal region; however, Equation 5.8 shows that in the process of calculating C_{peak} we do observe the number of data events in the signal region. In order to avoid any chance of experimenter bias we therefore only calculate values for C_{peak} up to and including the E_{extra} cut in the signal selection process (after which data become blinded).

We do not consider this to be a major hindrance as we expect that values of C_{peak} calculated later in the signal selection process would have large uncertainties due to the low number of events and therefore not be useful in obtaining a precise estimate of background MC yield. Indeed, this large increase in uncertainty after the E_{extra} cut can be seen in R_{MC} (whose calculation does not involve unblinding data in the signal-region) in Figure 5.3.1a.

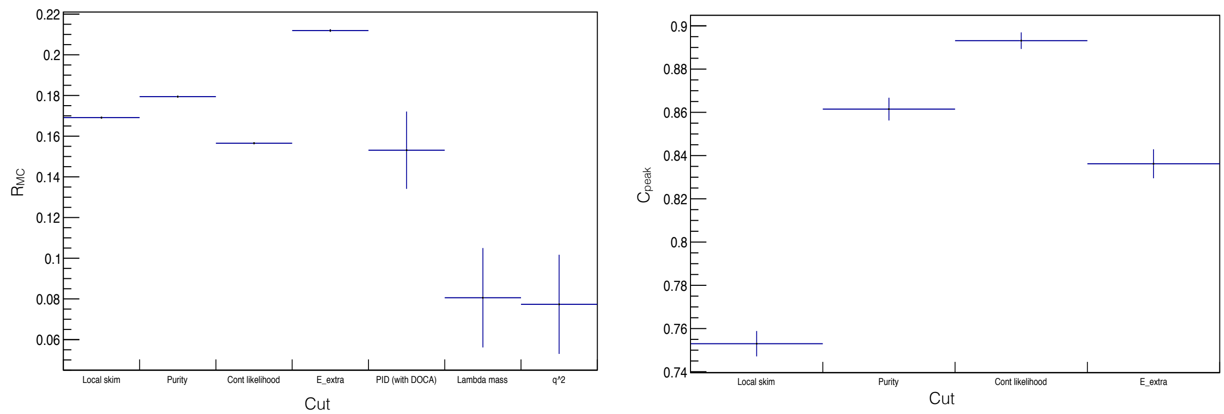

(a) R_{MC} *as a function of cut.*

(b) C_{peak} *as a function of cut.*

Figure 5.3.1: Monte Carlo ratio (R_{MC}) and peaking correction factor (C_{peak}) as a function of cut.

We can understand the behaviour of R_{MC} and C_{peak} by examining Figure 5.3.2. The proportion of signal-region to sideband-region MC remains relatively constant after the local-skim, B-mode purity and continuum likelihood cuts. However, after the E_{extra} cut the combinatorial tail to the left of the m_{ES} peak is flattened considerably, resulting in a higher signal-region to sideband-region ratio of combinatorial MC, and hence a higher value of R_{MC}. The fact that the value of C_{peak} changes only slightly during the first four cuts implies that the ratio of peaking-MC to peaking-data remains relatively constant during these cuts, although this is not as readily visible from Figure 5.3.2.

For cuts after the E_{extra} cut the MC background which remains in the signal-region becomes increasingly peaking (as opposed to combinatorial) whereas the MC background in the sideband-region remains inherently combinatorial; hence we see a large drop in the value of R_{MC}. The uncertainty on R_{MC} also increases substantially due to the small number of events (~1 event per bin) at these later stages (see Figure 5.3.2).

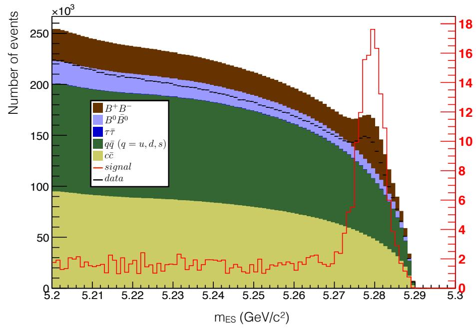

(a) B_{tag} m_{ES} *after local skim cut.*

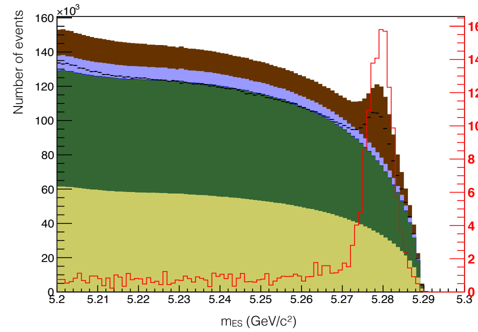

(b) B_{tag} m_{ES} *after* B*-mode purity cut.*

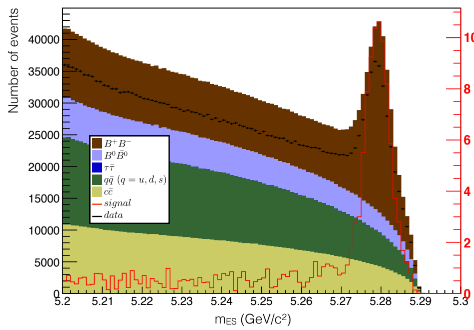

(c) B_{tag} m_{ES} *after continuum likelihood cut.*

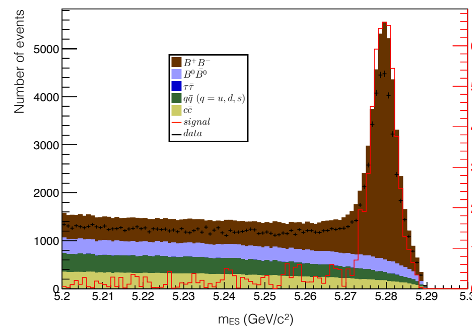

(d) B_{tag} m_{ES} *after* E_{extra} *cut.*

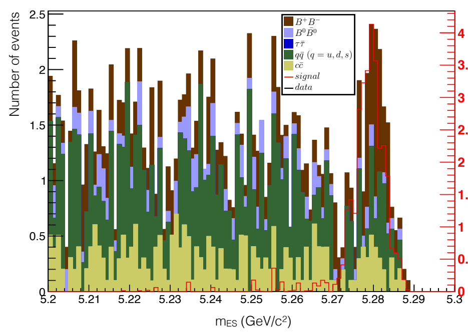

(e) B_{tag} m_{ES} *after particle identification (PID) cut (incorporating distance of closest approach (DOCA)).*

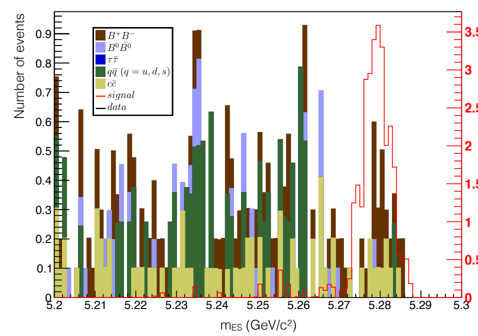

(f) B_{tag} m_{ES} *after* m_{Λ} *cut.*

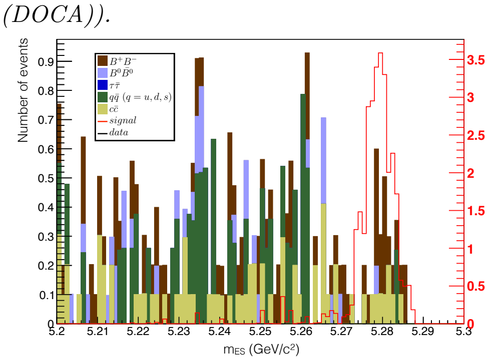

(g) B_{tag} m_{ES} *after* q^2 *cut.*

Figure 5.3.2: B_{tag} m_{ES} *after each* successive *signal selection cut.*

Due to the flat shape of the combinatorial tail and the well-defined $m_{\rm ES}$ peak immediately after the E_{extra} cut we take our values of R_{MC} and C_{peak} at this stage of the signal selection. We thus obtain $R_{MC} = 0.212$ and $C_{peak} = 0.836$. These values will be used later (see Section 6.2) to estimate our remaining background at the end of the signal selection.

Note that although the $m_{\rm ES}$ sideband subtraction improves the agreement between MC and data there is still residual disagreement. This will be accounted for as a systematic uncertainty (see Section 6.1.4).

Since background MC does not accurately estimate $B_{\rm tag}$ yield we must also assume that signal MC suffers from the same deficiency. At the end of our signal selection we therefore also scale our final signal efficiency value by C_{peak} (there is no need to use R_{MC} as the combinatorial component of signal MC at the end of the signal selection is negligible, as can be seen by examining the signal MC in Figure 5.3.2g).

5.4 Validation

We must verify that the signal selection is valid by performing it on a non-signal data and MC sample. To do this we take the portion of our data and MC which lies in the $B_{\rm tag}$ $m_{\rm ES}$ sideband region and perform a signal selection on this set of events (the "control sample") and compare to the results we see for events in the $B_{\rm tag}$ $m_{\rm ES}$ signal region (the "signal sample").

Observing Figure 5.2.6 we note that after the E_{extra} cut the MC distribution is "well behaved" - all MC event types show a relatively flat combinatorial shape in the sideband and there is a well-defined peak consisting of B^+B^- events. We consequently choose to divide our data and MC samples here and compare variables and distributions which play an important role in our signal selection. Working from this stage of the signal selection process also means we have as complete a signal selection process as possible without having entered the low-statistics regime that begins after the E_{extra} cut.

Working from this stage of the signal selection has the disadvantage that the background mix is not similar - the background in the control sample has a much higher proportion of continuum events while in the signal sample it is dominated by peaking B^+B^- events. In cases where this difference in background composition is problematic for validation purposes we can simply move back in the signal selection to a stage where the background mix is more alike.

Charged track momentum

Charged track momentum is an important variable in this analysis as it affects particle identification efficiency [6], which in turn is important in our Λ reconstruction process (see Section 5.2.3).

Comparing the distribution of the lab-frame momentum of all tracks between the control sample and the signal sample (see Figure 5.4.1) we can see that there are no notable features present in one but absent in the other. The shape of the distributions is similar, although they vary slightly due to the much higher proportion of events which are B^+B^- in the signal sample; this is confirmed by comparing the shapes with fewer cuts, and thus a smaller difference in proportion of events that are B^+B^-, where we find that the distributions' shapes match much more closely (see Figure 5.4.2). The signal MC in both the control sample and signal sample show similar distributions.

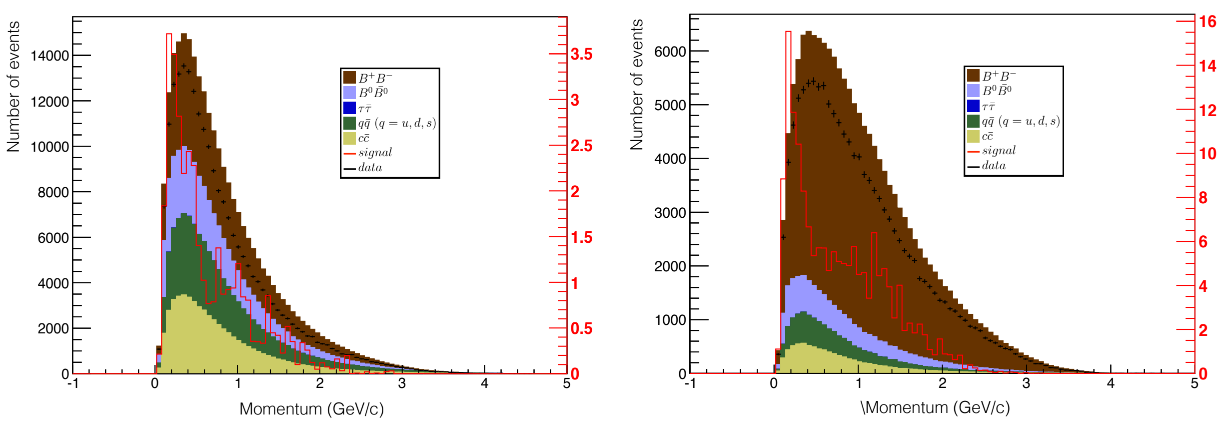

(a) *Control sample.* (b) *Signal sample.*

Figure 5.4.1: Lab-frame momentum for all charged tracks in control and signal samples after local-skim, B-mode purity, continuum likelihood and E_{extra} cuts.

The data/MC agreement is good in terms of shape but there is a discrepancy in number, as expected. By plotting the signal sample momentum distribution after an m_{ES} sideband substitution has been implemented (based on the R_{MC} and C_{peak} obtained after the implementation of the E_{extra} cut,

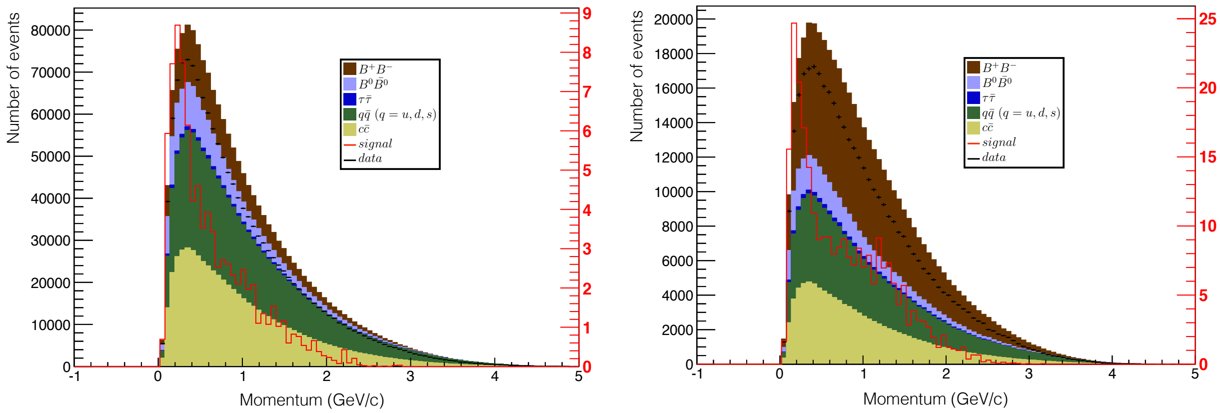

(a) *Control sample.* (b) *Signal sample.*

Figure 5.4.2: Lab-frame momentum for all charged tracks in control and signal samples, after local-skim and E_{extra} cuts only.

see Section 5.3) we observe a much improved data/MC agreement and similar shapes in data and MC, as shown in Figure 5.4.3.

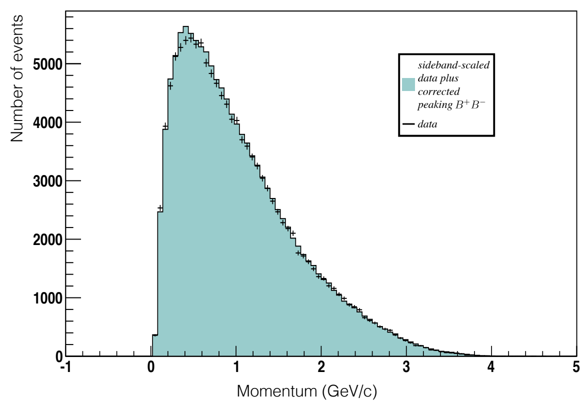

Figure 5.4.3: Lab-frame momentum for all charged tracks in signal sample, after $m_{\rm ES}$ sideband substitution and after local-skim, B-mode purity, continuum likelihood and E_{extra} cuts..

Cluster energy

Cluster energy, for clusters not associated with charged tracks and not used in the reconstruction of the $B_{\rm tag}$, is an important variable in this analysis as it correlates with E_{extra}, on which we cut during our signal selection. Comparing the control sample and signal sample (see Figure 5.4.4) we can see similarly-shaped distributions for both background and signal MC. The signal MC shape is somewhat less smooth in the control sample although this is probably due to the limited number of signal MC events in the m_{ES} sideband (and hence in the control sample).

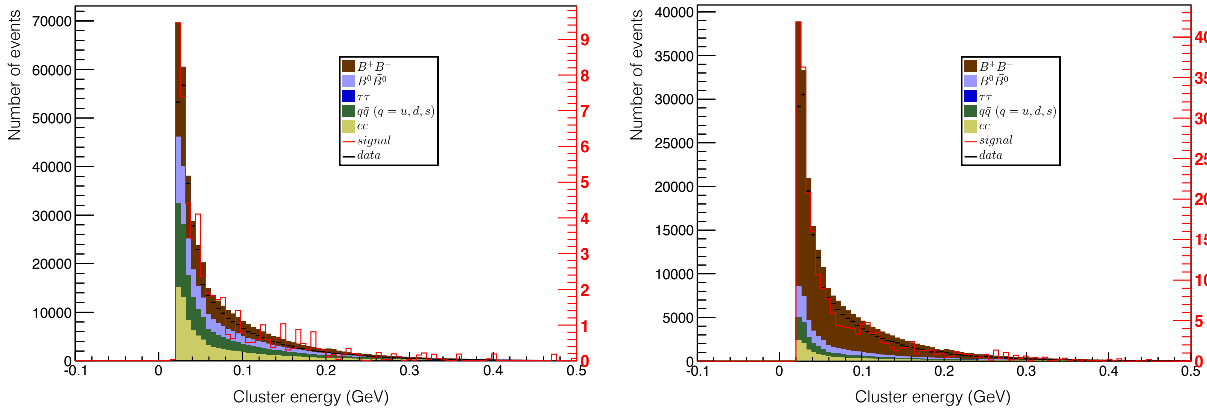

(a) *Control sample.* (b) *Signal sample.*

Figure 5.4.4: Lab-frame cluster energy for all clusters (except those associated with charged tracks and those used in B_{tag} reconstruction) in control and signal samples after local-skim, B-mode purity, continuum likelihood and E_{extra} cuts.

The MC/data agreement is good at higher energies although worsens as we approach zero energy. After implementing the same m_{ES} sideband substitution as used in the case of charged track momentum we see much better agreement and a similar shape in the data and MC distributions (see Figure 5.4.5).

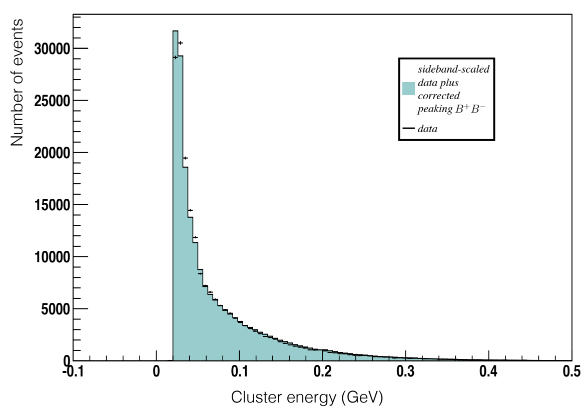

Figure 5.4.5: Lab-frame cluster energy for all clusters (except those associated with charged tracks and those used in B_{tag} reconstruction) in signal sample, after m_{ES} sideband substitution and after local-skim, B-mode purity, continuum likelihood and E_{extra} cuts.

Distance of closest approach (DOCA)

DOCA plays an important role in the Λ reconstruction process (see Section 5.2.5). Comparing DOCA between the control and signal samples, shown in Figure 5.4.6, we observe similar distributions for each in both signal MC and background MC (again, the signal MC distribution in the control sample is not as smooth as in the signal sample, presumably due to limited statistics). The data/MC agreement is similar in each case with good agreement at higher DOCA but worsening at lower DOCA; however, upon implementing the m_{ES} sideband substitution we obtain a much better agreement (see Figure 5.4.7).

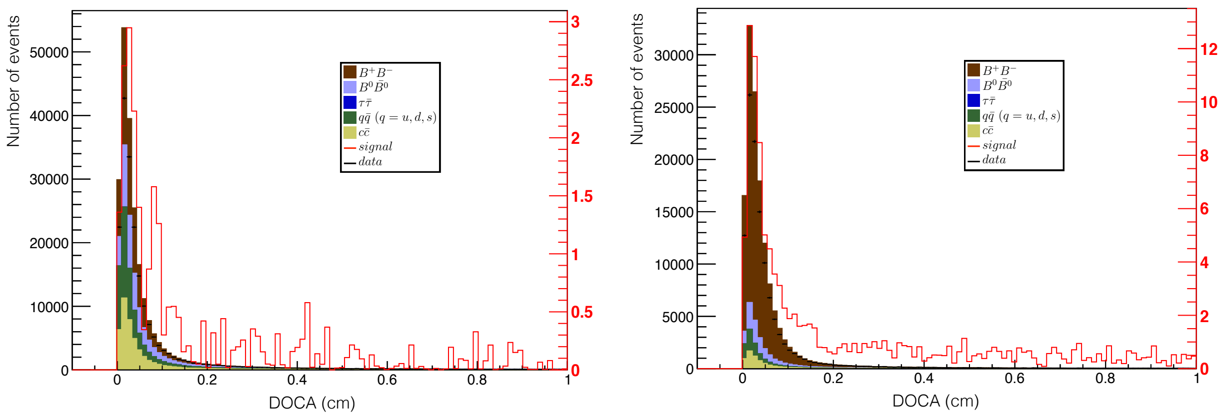

(a) *Control sample.* (b) *Signal sample.*

Figure 5.4.6: Lab-frame distance of closest approach (DOCA) for all charged tracks in control and signal samples after local-skim, B-mode purity, continuum likelihood and E_{extra} cuts.

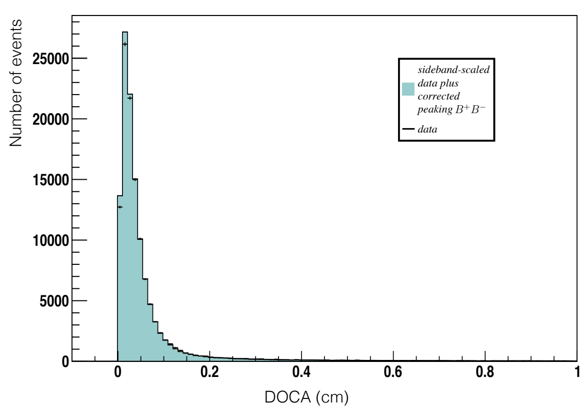

Figure 5.4.7: Lab-frame distance of closest approach (DOCA) for all charged tracks in signal sample, after m_{ES} sideband substitution and after after local-skim, B-mode purity, continuum likelihood and E_{extra} cuts.

Λ reconstruction

Reconstructing the Λ peak is important in this analysis not only because we cut around it to obtain a good Λ mass (see Section 5.2.4) but because it also provides a good validation test - assuming we have a good signal selection we should be able to recreate the Λ peak in the control sample.

We perform a Λ-mass reconstruction (including DOCA) in both the control and signal sample. Due to the very low number of events which survive this process we perform this after having implemented only the local-skim cuts; a Λ mass reconstruction done later in the analysis has insufficient events in the control and signal samples to produce comparable results. The results are shown in Figure 5.4.8 where we observe that we obtain a Λ-mass peak in the control sample very similar to that in the signal sample, for both signal MC and background MC.

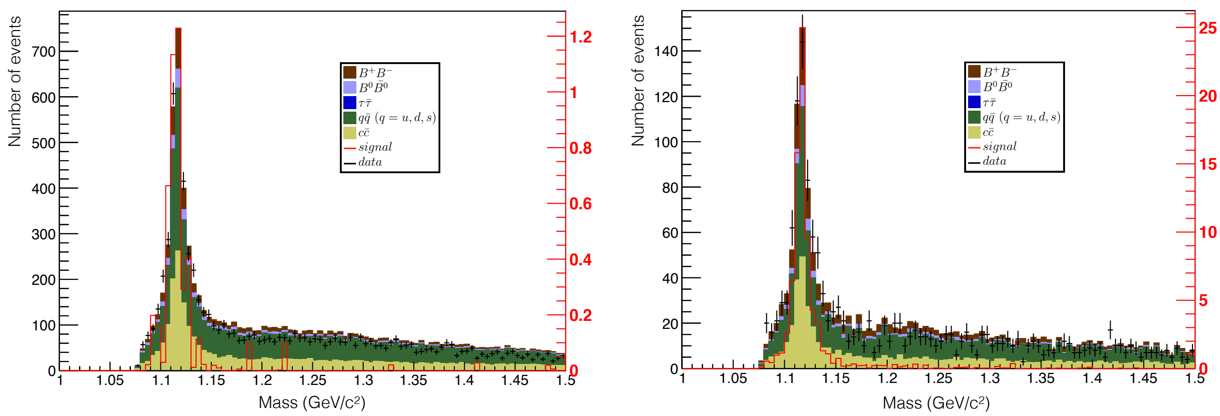

(a) *Control sample.* (b) *Signal sample.*

Figure 5.4.8: Reconstructed Λ mass in control and signal samples after local-skim cuts only.

In both cases there is good data/MC agreement, although the MC tends to slightly underestimate data in the combinatorial tail and overestimate it in the Λ-mass peak. We can perform an m_{ES} sideband substitution using the events that appear in our histograms of the Λ-mass peak; the result is shown in Figure 5.4.9 where we can see improved MC/data agreement.

Invariant mass of tracks

We can further investigate the validity of our signal selection by searching for other invariant masses using the charged tracks in our events *before* the assignment of particle masses during

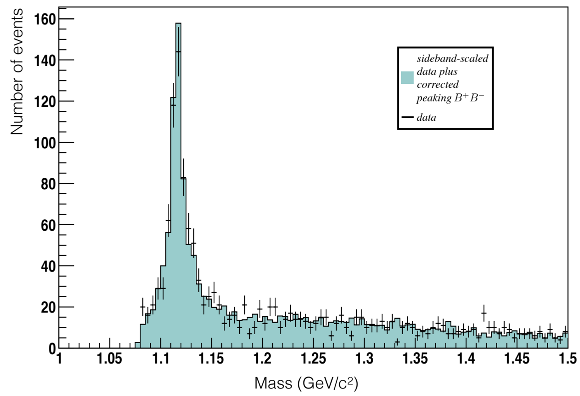

Figure 5.4.9: Reconstructed Λ mass in signal sample, after m_{ES} sideband substitution and after local-skim cuts only.

the PID process (see Section 5.2.3). Although we do not make a cut on this distribution, any feature appearing in one of our signal or control samples but not the other would be a cause for concern.

Figure 5.4.10 shows the invariant mass of all three charged tracks for each event. There are no distinguishing features (mass peaks) in either the control or signal samples. The difference in shape of the two distributions is due to the much higher proportion of events in the signal sample that are B^+B^- events. This can be confirmed by plotting the same quantity at an earlier stage of the signal selection, shown in Figure 5.4.11, where the distributions' shapes are much more similar.

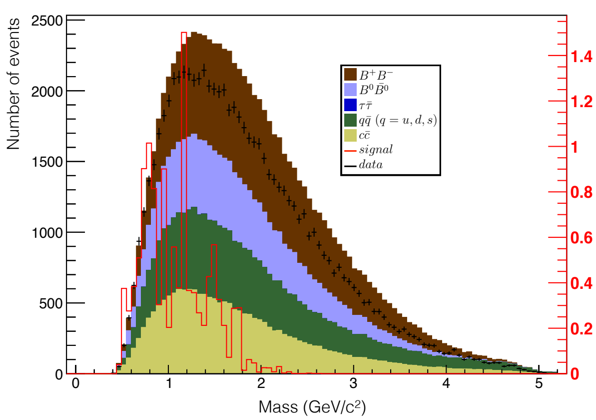

(a) *Control sample.*

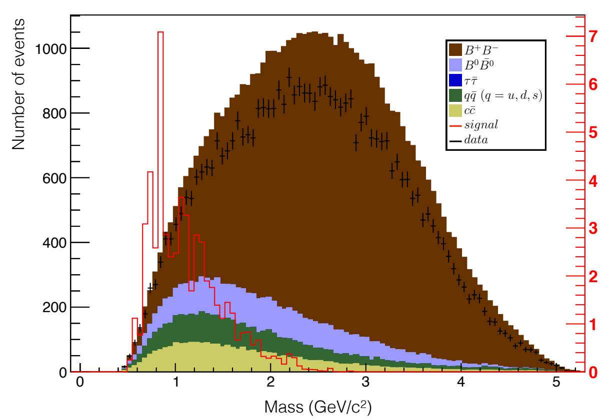

(b) *Signal sample.*

Figure 5.4.10: Invariant mass of all three tracks in an event in control and signal samples after local-skim, B-mode purity, continuum likelihood and E_{extra} cuts.

The MC/data agreement in Figure 5.4.10b is generally good, and is much improved after the

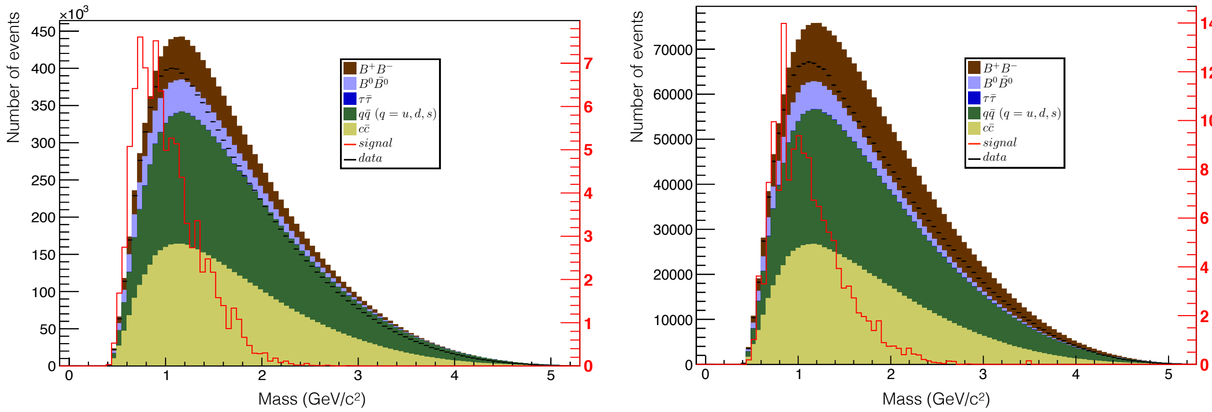

(a) *Control sample.* (b) *Signal sample.*

Figure 5.4.11: Invariant mass of all three tracks in an event in control and signal samples after local-skim cuts only.

application of an m_{ES} sideband substitution, shown in Figure 5.4.12.

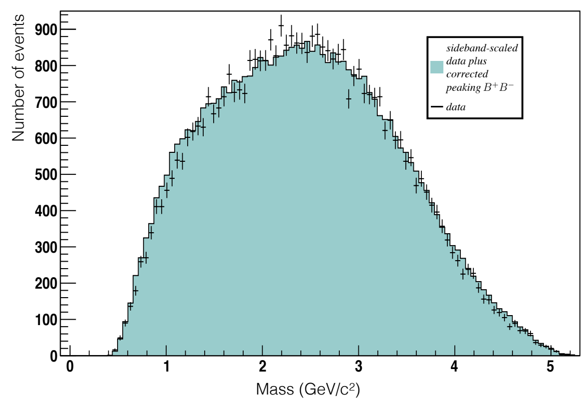

Figure 5.4.12: Invariant mass of all three tracks in an event in signal sample, after m_{ES} sideband substitution and after local-skim, B-mode purity, continuum likelihood and E_{extra} cuts.

Invariant mass of clusters

We can also plot the invariant mass of clusters in our control and signal samples. As with invariant mass of charged tracks, any unexplained mass peak which appears in one of our signal or control samples but not the other is a potential cause for concern.

Figure 5.4.13 shows the invariant mass of all possible pairs of clusters (except clusters associated with charged tracks and those used in B_{tag} reconstruction) in an event, for all events that pass local-skim cuts. We choose to plot the invariant mass of pairs of clusters as we expect to observe a π^0 mass peak (at $\sim 135\,\mathrm{MeV}/c^2$) from the decay $\pi^0 \to \gamma\gamma$, and we plot this quantity at an early stage of the selection to ensure sufficient statistics to make any peak clearly visible.

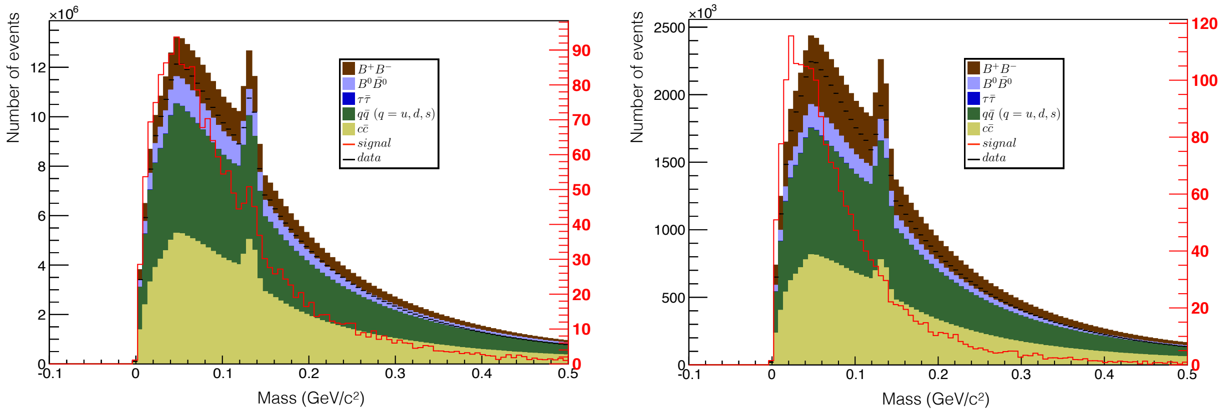

(a) *Control sample.* (b) *Signal sample.*

Figure 5.4.13: Invariant mass of all possible pairs of clusters in an event (except those associated with charged tracks and those used in B_{tag} reconstruction) in control and signal samples after local-skim cuts only.

As we can see, a π^0 peak at approximately 135 MeV/c^2 is visible in background MC and data for both the control and signal samples. The data and background MC have similar shapes, with much-improved agreement after implementation of an m_{ES} sideband substitution (see Figure 5.4.14).

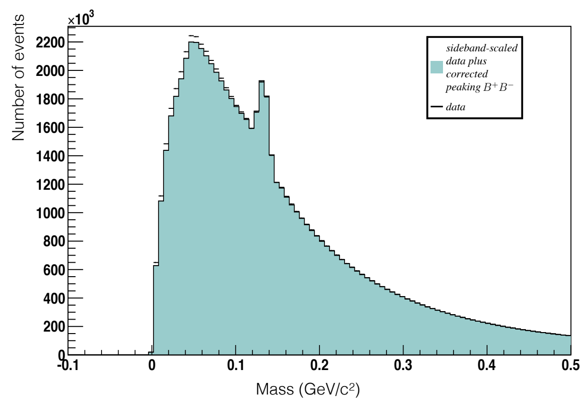

Figure 5.4.14: Invariant mass of all possible pairs of clusters in an event (except those associated with charged tracks and those used in B_{tag} reconstruction) in signal sample, after m_{ES} sideband substitution and after local-skim cuts only.

A notable difference, though, is that a π^0 peak is visible in signal MC in the control sample but not in the signal sample. This behaviour is, however, expected. Our signal MC simulates $B^- \to \Lambda\bar{p}\nu\bar{\nu}$ and we would therefore not expect to see a π^0 mass peak. However, our control sample comprises events in the m_{ES} sideband. By definition, these events have misconstructed B_{tag}'s (and B_{sig}'s), therefore it is possible for π^0's that should have been assigned to the B_{tag} to be misassigned to the B_{sig}, leading to the π^0 mass peaks in our control sample. A small combinatorial component of misreconstructed B mesons will be present even in our signal sample of our signal MC; we therefore expect π^0's to be present in the signal sample but their number is so small in comparison to correctly reconstructed events that their presence is not readily visible.

Conclusion

We have observed that a variety of important variables show similar distributions in both control and signal samples, for both signal MC and background MC. Additionally, data/MC agreement is generally good, and very good after the implementation of appropriate m_{ES} sideband substitutions. Particulalry notable is the replication of a reconstructed Λ-mass peak in our control sample. The similarities observed between the control sample and signal sample lead us to conclude that our signal selection is valid.

5.5 Summary of cuts

Table 5.1 shows a summary of the cuts made in our signal selection as well as the number of background events and the signal efficiency after each cut. For the E_{extra} cut onwards it also shows these values after the m_{ES} sideband substitution.

Table 5.2 shows the marginal effect of each cut. That is, it shows the number of MC background events and the signal efficiency at the end of the full signal selection with the specified cut removed. It therefore serves to show us which cuts have the largest effect (evidently, the PID, m_Λ and q^2 cuts, followed by the E_{extra} cut, followed by the B_{tag} m_{ES} cut etc.).

Table 5.1: *Summary of cuts, background yields and signal efficiencies. Numbers in brackets give the corresponding value after m_{ES} sideband substitution, using the values of R_{MC} and C_{peak} obtained from immediately after the E_{extra} cut in the signal selection process (see Section 5.3 for more details). Uncertainties are statistical only.*

Cut	Events in background MC [after sideband substitution]	Signal efficiency [after sideband substitution]
Local skim	$(1.8190 \pm 0.0002) \times 10^7$	$(0.554 \pm 0.004)\%$
B_{tag} m_{ES}	$(2.6005 \pm 0.0007) \times 10^6$	$(0.312 \pm 0.003)\%$
B-mode purity	$(1.7801 \pm 0.0005) \times 10^6$	$(0.277 \pm 0.003)\%$
Continuum likelihood	$(5.1268 \pm 0.0026) \times 10^5$	$(0.185 \pm 0.002)\%$
E_{extra}	$51,474 \pm 75$ $[43,277 \pm 244]$	$(0.118 \pm 0.002)\%$ $[(0.0990 \pm 0.0018)\%]$
PID (with DOCA)	22.27 ± 1.80 $[16.72 \pm 1.90]$	$(0.0682 \pm 0.0015)\%$ $[(0.0570 \pm 0.0013)\%]$
m_Λ	3.56 ± 0.63 $[4.12 \pm 0.85]$	$(0.0630 \pm 0.0014)\%$ $[(0.0527 \pm 0.0013)\%]$
q^2	3.46 ± 0.62 $[4.12 \pm 0.85]$	$(0.0630 \pm 0.0014)\%$ $[(0.0527 \pm 0.0013)\%]$

Table 5.2: *Marginal efficiencies and background yields. Shows the number of events in background MC and the signal efficiency after the full signal selection with the exception of the specified cut. Uncertainties are statistical only. Note that exclusion of the PID (with DOCA) cut requires exclusion of the m_Λ and q^2 cuts since both the m_Λ and q^2 cuts are dependent on Λ's having been identified. Similarly, exclusion of the m_Λ cut requires exclusion of the q^2 cut since q^2 is not meaningfully defined unless Λ's have been identified.*

Cut	Events in background MC	Signal efficiency
B_{tag} m_{ES}	27.38 ± 2.06	$(0.0669 \pm 0.0014)\%$
B-mode purity	5.36 ± 0.76	$(0.0672 \pm 0.0015)\%$
Continuum likelihood	20.93 ± 1.91	$(0.0930 \pm 0.0017)\%$
E_{extra}	113.2 ± 3.98	$(0.0960 \pm 0.0018)\%$
PID (with DOCA) and m_Λ and q^2	$51,474 \pm 75$	$(0.118 \pm 0.002)\%$
m_Λ and q^2	22.27 ± 1.80	$(0.0682 \pm 0.0015)\%$
q^2	3.56 ± 0.63	$(0.0630 \pm 0.0014)\%$

Chapter 6

Analysis results

6.1 Systematic uncertainties

The results of this analysis are dependent on a good understanding of how well our MC simulations represent both background and signal events. Apart from purely statistical uncertainties there are also uncertainties associated with MC phase space reweightings, B meson yields and signal selection cuts.

6.1.1 Signal Monte Carlo

As explained in Section 4.5 we reweighted our signal MC to match the predicted distribution of the invariant mass of the $\Lambda\overline{p}$ pair, resulting in a signal efficiency, after the full signal selection has been implemented, of 0.0630%. Reweighting to a combination of $\Lambda\overline{p}$ invariant mass and one other variable (see Section 4.5 for details of variables) produces signal efficiencies which differ from reweighting to $\Lambda\overline{p}$ invariant mass as shown in Table 6.1.

We average the difference between the reweighting to $m_{\Lambda\overline{p}}$ and the three combinations to arrive at a systematic uncertainty on our signal efficiency due to phase space reweighting of 4.81%.

Also, as mentioned in Section 4.5, there are a small number of signal MC events which do not

Table 6.1: Dependence of signal efficiency on phase space reweighting. Uncertainties are statistical only.

Variable(s) to reweight to	Signal efficiency after full signal selection
$m_{\Lambda\overline{p}}$	$(0.0630 \pm 0.0014)\%$
$m_{\Lambda\overline{p}}$ and θ_L	$(0.0603 \pm 0.0014)\%$
$m_{\Lambda\overline{p}}$ and $m_{\nu\overline{\nu}}$	$(0.0585 \pm 0.0014)\%$
$m_{\Lambda\overline{p}}$ and θ_B	$(0.0611 \pm 0.0014)\%$

conform to the $B^- \to \Lambda\overline{p}\nu\overline{\nu}$ decay channel at the truth level. These events constitute 1.15% of signal MC events which pass local-skim cuts. We therefore take this as an additional uncertainty on our signal efficiency.

6.1.2 $\boldsymbol{B}$-mode purity cut

Any uncertainty due to MC/data disagreement, and any uncertainty on signal efficiency, associated with the cut on B-mode purity is accounted for when we implement the $m_{\rm ES}$ sideband substitution, or is included in the $B_{\rm tag}$ yield uncertainty, which is introduced later in the analysis, after the E_{extra} cut.

6.1.3 Continuum likelihood cut

Any uncertainty due to MC/data disagreement, and any uncertainty on signal efficiency, associated with the cut on continuum likelihood is accounted for when we implement the $m_{\rm ES}$ sideband substitution, or is included in the $B_{\rm tag}$ yield uncertainty, which is introduced later in the analysis, after the E_{extra} cut.

Figure 6.1.1 shows the variables used to calculate continuum likelihood but after $m_{\rm ES}$ sideband substitution and after local-skim, B-mode purity, continuum likelihood and E_{extra} cuts. We can see that they generally show very good MC/data agreement, demonstrating that the $m_{\rm ES}$ sideband substitution adequately accounts for any difference in MC/data yield, while any remaining discrepancy will be accounted for in the $B_{\rm tag}$ yield systematic uncertainty.

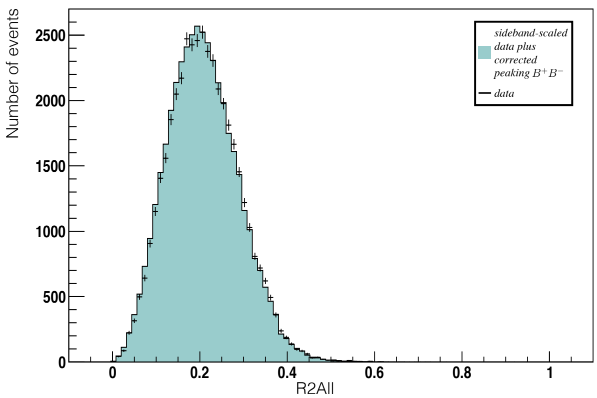

(a) *R2All.*

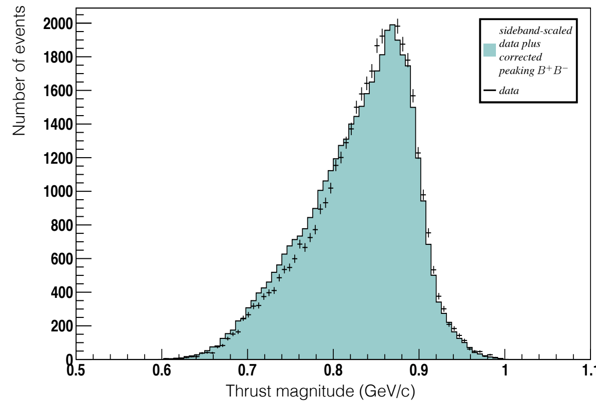

(b) *Thrust magnitude.*

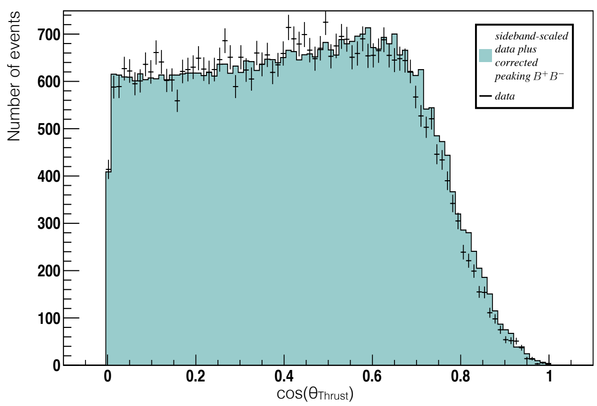

(c) *Cosine of thrust angle.*

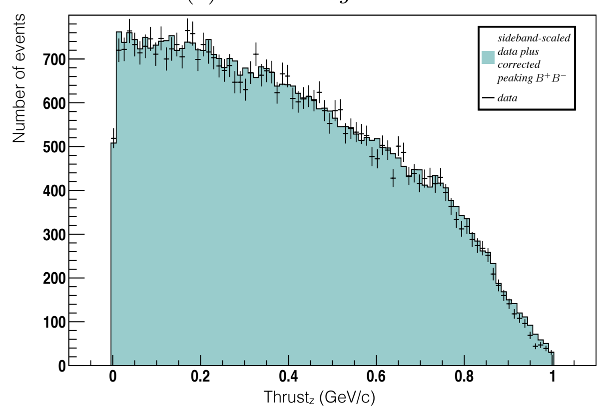

(d) *z-component of thrust.*

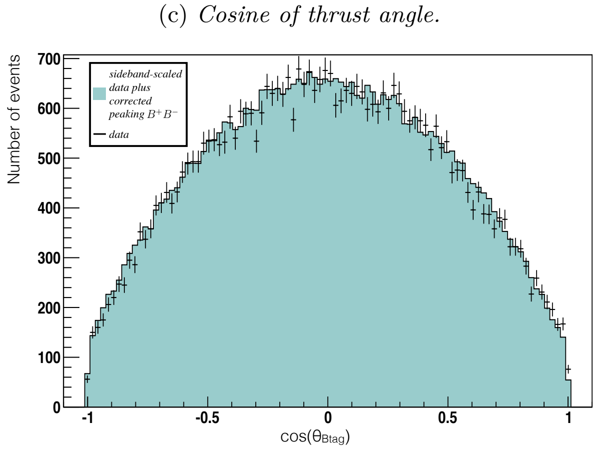

(e) *Cosine of angle between* B_{tag} *and z-axis (beam).*

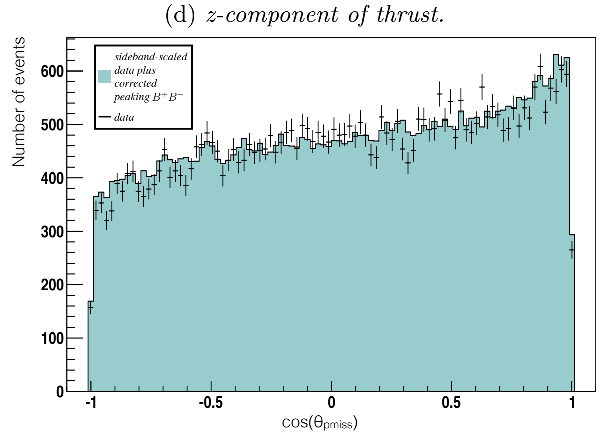

(f) *Cosine of angle between missing momentum and z-axis (beam).*

Figure 6.1.1: The variables used to calculate continuum likelihood, after m_{ES} *sideband substitution and after local-skim, B-mode purity, continuum likelihood and* E_{extra} *cuts.*

6.1.4 B_{tag} yield

Our background MC simulations do not accurately simulate the number of B mesons in data. As described in Section 5.3, we use data in the m_{ES} sideband region to estimate combinatorial B meson yield in the m_{ES} signal region and a correction factor to account for any remaining discrepancy which is due to peaking background.

Since the combinatorial and peaking components of MC background must sum to match data in the m_{ES} signal region, the systematic uncertainty on combinatorial B meson yield is anticorrelated with the systematic uncertainty on peaking B meson yield. Thus if we only evaluate a systematic uncertainty on, for example, peaking B meson yield, this accounts for the systematic uncertainty on combinatorial B meson yield.

We therefore choose to evaluate a systematic uncertainty on peaking B meson yield where we use a correction factor, $C_{peak} = 0.836 \pm 0.007$, evaluated immediately after the E_{extra} cut, to scale our peaking background MC. We take half the value of the correction as our error, i.e. $(1 - 0.836)/2 = 8.20\%$, as the systematic uncertainty associated with our calculation of the peaking B meson yield.

We consider the uncertainty on peaking B meson yield as an uncertainty both on MC background yield and on signal efficiency (this is noted in Table 6.4). It is an uncertainty on B meson yield for the obvious reason that it directly affects the number of background events in our MC. We consider it also as an uncertainty on signal efficiency due to the effect of estimated B meson yield on branching fraction (see Equation 6.1).

In the context of our total systematic uncertainty we consider this a conservative estimate because other systematic uncertainties, detailed later in this section, are calculated based on MC/data agreement, providing an element of double-counting of B meson yield uncertainty.

6.1.5 Particle identification, distance of closest approach and m_{Λ} cuts

The PID, DOCA and m_{Λ} cuts are together referred to as the "Λ reconstruction" cut.

To evaluate a systematic uncertainty on the Λ reconstruction cut we examine the data/MC ratio before and after the Λ reconstruction cut on the set of events which survive the local-skim, B_{tag} m_{ES} and continuum likelihood cuts (the E_{extra} cut is not implemented as this leads to very low statistics and the number of events in data becomes blinded). Figures 6.1.2 shows B_{tag} m_{ES}, over the full m_{ES} range, for these events before and after the Λ reconstruction cut is implemented.

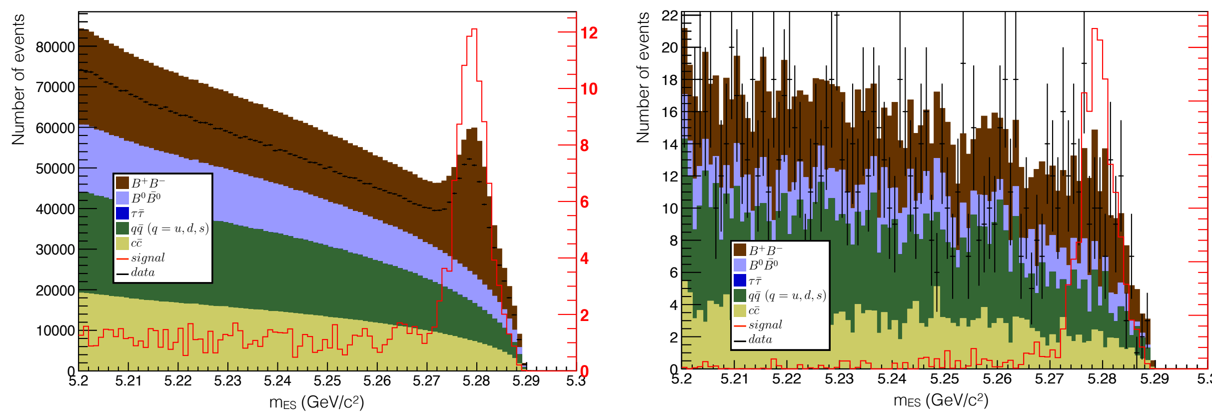

(a) *Before lambda reconstruction cut.* (b) *After lambda reconstruction cut.*

Figure 6.1.2: B_{tag} m_{ES} before and after the Λ reconstruction and after local-skim and continuum likelihood cuts.

The data/MC ratio before Λ reconstruction is 0.8589 ± 0.0011(stat.) and after is 0.9475 ± 0.0752(stat.), representing an increase in data/MC ratio of 10.32%. Although this is a large change we have confidence in our Λ reconstruction method based on our validation studies (see Section 5.4); we therefore take this as the systematic uncertainty on our MC background yield associated with the Λ reconstruction cut. We consider this to be a very conservative value as we are measuring the change in data/MC agreement between a stage of the analysis with a relatively large discrepancy and a stage with a much smaller discrepancy. We are thus in effect measuring an uncertainty on the B_{tag} yield (see Section 6.1.4), and thus there is an element of double counting when we combine the systematic uncertainties on both the B_{tag} yield and the Λ reconstruction cut.

Note that we intend to improve the Λ reconstruction method in the future (as part of a full, unblinded analysis) by incorporating vertex information; however, this conservative systematic uncertainty is sufficient for the purposes of this sensitivity study.

6.1.6 E_{extra} cut

Since the cut on E_{extra} eliminates both a considerable number of signal MC and background MC events we evaluate two uncertainties associated with the E_{extra} cut: one on the signal efficiency and one on the MC background yield.

For the uncertainty on signal efficiency we examine the signal efficiency at the end of the full signal selection but using three different definitions of E_{extra}: E_{extra} defined using unadjusted cluster energies, E_{extra} defined using cluster energies adjusted by $-5\,\mathrm{MeV}$ (which is the definition we use in our signal selection) and E_{extra} defined using cluster energies adjusted by $-10\,\mathrm{MeV}$. In both of the latter cases there is a minimum permitted cluster energy of $0\,\mathrm{MeV}$. For more details on the definition of E_{extra} and the rationale for adjusting cluster energies see Appendix B. The results are shown in Table 6.2.

Table 6.2: Signal efficiency after full signal selection with different definitions of E_{extra}. Uncertainties are statistical only. E_{extra} adjusted by $-5\,\mathrm{MeV}$ is the definition used in our signal selection. Unadjusted E_{extra} and E_{extra} adjusted by $-10\,\mathrm{MeV}$ are the limits beyond which we do not consider MC and data to have sufficiently good agreement.

E_{extra} adjustment	Signal efficiency after full signal selection	Difference from median
Unadjusted	$(0.0620 \pm 0.0014)\%$	-1.59%
$-5\,\mathrm{MeV}$	$(0.0630 \pm 0.0014)\%$	n.a.
$-10\,\mathrm{MeV}$	$(0.0643 \pm 0.0014)\%$	$+2.06\%$

The definition of E_{extra} used in the final signal selection is that adjusted by $-5\,\mathrm{MeV}$. We therefore take the average of the difference in signal efficiency between this and the two other definitions (unadjusted, and adjusted by $-10\,\mathrm{MeV}$) as the systematic uncertainty on signal efficiency associated with our E_{extra} cut, giving us an uncertainty of 1.83%.

For the uncertainty on MC background yield we examine the data/MC ratio at the stage of the signal selection immediately after the E_{extra} cut (i.e. after local-skim, B_{tag} m_{ES}, B-mode purity, continuum likelihood and E_{extra} cuts), again using the three different definitions of E_{extra}. The results are shown in Table 6.3.

As for the uncertainty on signal efficiency above, we take the average of the difference between the

Table 6.3: *Data/MC ratio after local-skim, $B_{\rm tag}$ $m_{\rm ES}$, B-mode purity, continuum likelihood and E_{extra} cuts, with different definitions of E_{extra}. Uncertainties are statistical only.*

E_{extra} adjustment	Data/MC ratio immediately after E_{extra} cut	Difference from median
Unadjusted	0.9081 ± 0.0046	$+9.55\%$
$-5\,\mathrm{MeV}$	0.8289 ± 0.0042	n.a.
$-10\,\mathrm{MeV}$	0.7606 ± 0.0038	-8.24%

definition we use in the final signal selection (adjusted by $-5\,\mathrm{MeV}$) and the other two definitions, giving us a systematic uncertainty on background MC yield due to our E_{extra} cut of 8.90%.

6.1.7 Summary of systematic uncertainties

Table 6.4 shows a summary of the systematic uncertainties discussed in this section.

Table 6.4: Summary of systematic uncertainties.

Source	Type	Value
Signal MC	signal efficiency	4.81%, 1.15%
$B_{\rm tag}$ yield	MC background yield, signal efficiency	8.20%
Λ reconstruction	MC background yield	10.32%
E_{extra} cut	signal efficiency	1.83%
E_{extra} cut	MC background yield	8.90%

6.2 Branching fraction calculation and limit setting

In order to calculate a branching fraction limit we first need to determine our estimate of both signal efficiency and MC background yield at the end of the full signal selection. This involves calculating peaking and combinatorial MC background yields and signal efficiencies, incorporating corrections from the $m_{\rm ES}$ sideband substitution, and calculating statistical and systematic uncertainties for these numbers.

The values of R_{MC} and C_{peak} chosen as a result of our $m_{\rm ES}$ sideband substitution (see Section 5.3 for details) are $R_{MC} = 0.212 \pm 0.001$ and $C_{peak} = 0.836 \pm 0.007$, where the uncertainties are statistical. For calculation of our background MC yield after implementation of the $m_{\rm ES}$ sideband substitution we use Equations 5.6, 5.7 and 5.9. The relevant input for these equations are shown in Table 6.5.

Table 6.5: Number of events in data and background MC at the end of the full signal selection that are required for calculation of the final background estimate. Superscript indicates m_{ES} signal- or sideband-region, subscript indicates type of event. Uncertainties are statistical only.

Type	Number of events
$N^{sig}_{B^+B^-}$	2.11 ± 0.46
$N^{sig}_{B^0\overline{B}^0}$	0.10 ± 0.10
$N^{side}_{B^+B^-}$	5.43 ± 0.74
$N^{side}_{B^0\overline{B}^0}$	2.36 ± 0.48
N^{side}_{Data}	12.00 ± 3.46

Using Equations 5.6, 5.7 and 5.9 we calculate the expected combinatorial and peaking background estimates; the results are shown in Table 6.6.

Table 6.6: Expected final background estimates after full signal selection and implementation of m_{ES} sideband substitution for combinatorial background, peaking background and total (combinatorial plus peaking) background. Uncertainties are calculated by the appropriate form of addition in quadrature; statistical uncertainties from the statistical uncertainties on R_{MC}, C_{peak} and those shown in Table 6.5; systematic uncertainties from the MC background yield systematic uncertainties shown in Table 6.4.

Type	Expected number of events
N^{comb}_{bkgd}	2.54 ± 0.73(stat.)
N^{peak}_{bkgd}	1.57 ± 0.43(stat.)
N^{total}_{bkgd}	4.12 ± 0.85(stat.) ± 0.65(sys.)

For comparison, the number of background MC events remaining after the full signal selection but without implementing the m_{ES} sideband substitution is 3.46 ± 0.62(stat.).

We calculate our final estimated signal efficiency by taking the signal efficiency at the end of the full signal selection, $(6.30 \pm 0.14(\text{stat.})) \times 10^{-4}$, and multiplying by C_{peak} (0.836 ± 0.007), to account for the m_{ES} sideband substitution, and by the branching fraction for $\Lambda \to p\pi^-$ (0.639 ± 0.005 [8]), to account for the fact that this analysis only searched for $B^- \to \Lambda\overline{p}\nu\overline{\nu}$ using this decay channel of the Λ. We then incorporate the signal efficiency uncertainties from Table 6.4 to obtain a final estimated signal efficiency, η^{final}_{sig}, of

$$\eta_{sig}^{final} = (3.37 \pm 0.08(\text{stat.}) \pm 0.33(\text{sys.})) \times 10^{-4}.$$

In the case of an analysis where the data have been unblinded, we would now calculate the branching fraction, $\mathcal{B}$, using

$$\mathcal{B} = \frac{N_{Data}^{obs} - N_{bkgd}^{total}}{\eta_{sig}^{final} \times N_{B\overline{B}}^{initial}} \tag{6.1}$$

where N_{Data}^{obs} is the observed number of data events and $N_{B\overline{B}}^{initial}$ is the initial number of $B\overline{B}$ pairs constituting the dataset. However, since this thesis is a sensitivity study where data remain blinded, we must calculate branching fractions for a range of possible values of N_{Data}^{obs}. We also calculate upper limits on $\mathcal{B}$ at the 90% confidence interval. To do this we use two techniques: Barlow and Feldman-Cousins.

Barlow

The Barlow method [7] works by generating a trial value for $\mathcal{B}$. This is then multiplied by "sensitivity", S, which in our case is $\eta_{sig}^{final} \times N_{B\overline{B}}^{initial}$. The value for S is generated from a Gaussian with mean S and standard deviation equal to the uncertainty on S supplied by us. This quantity ($\mathcal{B} \times S$) then has added to it a number of background events, b (in our case $b = N_{bkgd}^{total}$), again generated from a Gaussian with mean b and standard deviation equal to the uncertainty on b supplied by us. The quantity $\mathcal{B} \times S + b \equiv \mu$, where μ is now used as the mean of a Poisson distribution from which a number of events, n, is generated. The upper limit at the 90% confidence interval on $\mathcal{B}$ is the value of $\mathcal{B}$ for which 10% of MC trials give a value of n equal to or less than the number of observed events in data, N_{Data}^{obs} (although, in our case, N_{Data}^{obs} is assumed rather than observed since the data are blinded).

The Barlow method, however, does not account for the possibility that N_{Data}^{obs} is approximately equal to, or lower than, N_{bkgd}^{total}, and it can in these situations output negative values of $\mathcal{B}$, which are clearly unphysical. We therefore also make use of the Feldman-Cousins method which accounts for these scenarios.

Feldman-Cousins

The Feldman-Cousins method [14] works similarly to the Barlow method except that it requires physical (i.e. non-negative) values for $\mathcal{B}$ and it ranks simulation outputs by a likelihood ratio to determine an "acceptance region" for each given value of $\mathcal{B}$, where the acceptance region is the range of permitted values of n, and n is a possible value of the observed number of events (i.e. N^{obs}_{Data} in our case). The likelihood ratio, R, used to rank outputs is [24]

$$R = \frac{P(n|\mathcal{B})}{P(n|\mathcal{B}_{best})} \tag{6.2}$$

where $P(n|\mathcal{B})$ is the Poisson probability of observing n events given a branching fraction $\mathcal{B}$ and where the Poisson distribution has mean μ, with μ defined as for the Barlow method. [24] $P(n|\mathcal{B}_{best})$ is the same except $\mathcal{B}_{best}$ is the value of $\mathcal{B}$ which maximises $P(n|\mathcal{B})$.

For a given value of $\mathcal{B}$, values of n are added to the acceptance region in order of their rank (from highest R downwards) until the sum of their associated probabilities $P(n|\mathcal{B})$ is equal to or greater than 0.9 (for a 90% confidence interval). This is repeated for many trial values of $\mathcal{B}$. The upper limit at the 90% confidence interval on $\mathcal{B}$ is the highest value of $\mathcal{B}$ that has N^{obs}_{Data} in its acceptance region where, as before, N^{obs}_{Data} is in our case assumed rather than observed.

6.3 Final results

Table 6.7 shows the branching fraction central values and upper limits (calculated using the Barlow and Feldman-Cousins methods, see Section 6.2 for details) for $B^- \rightarrow \Lambda\bar{p}\nu\bar{\nu}$ for a range of possible values of the number of events observed in data after unblinding. Assuming we see no excess events in data (i.e. assuming $N^{obs}_{Data} = 4$ given our expected background of 4.12 events) we obtain branching fraction upper limits at the 90% confidence level of 2.64×10^{-5} (Barlow) and 3.10×10^{-5} (Feldman-Cousins). For comparison, the theoretically predicted branching fraction is $(7.9 \pm 1.9) \times 10^{-7}$ [17].

Table 6.7: Branching fraction central values and upper limits (at the 90% confidence level) for the decay $B^- \rightarrow \Lambda\bar{p}\nu\bar{\nu}$ as a function of assumed number of observed events in data, N^{obs}_{Data}. Expected background is $4.12 \pm 0.85(stat.) \pm 0.65(sys.)$ events. For details on branching-fraction limit calculation see Section 6.2.

N^{obs}_{Data}	Central value ($\times 10^{-5}$)	Barlow upper limit ($\times 10^{-5}$)	Feldman-Cousins upper limit ($\times 10^{-5}$)
0	−2.60	−0.77	0.65
1	−1.97	0.12	1.01
2	−1.34	0.97	1.62
3	−0.71	1.82	2.45
4	−0.01	2.64	3.10
5	0.55	3.39	3.96
6	1.18	4.20	4.93
7	1.81	5.02	5.76
8	2.44	5.84	6.55

Chapter 7

Conclusion

We have presented a sensitivity study for the search for the rare, flavour-changing-neutral-current decay $B^{-} \rightarrow \Lambda\overline{p}\nu\overline{\nu}$. $B^{-} \rightarrow \Lambda\overline{p}\nu\overline{\nu}$ is expected to be highly suppressed in the Standard Model and is therefore a sensitive probe for potential new physics.

Our study was conducted using data gathered at the *BABAR* experiment using a dataset of approximately 471 million $B\overline{B}$ pairs. We used hadronic B_{tag} reconstruction to isolate a B meson decay in which our search was conducted. We then implemented a signal selection based on cutting on variables in such a way as to reduce background processes while preserving signal efficiency.

Assuming that, when data are unblinded, we see no excess events in data over our final background estimate we predict branching fraction upper limits at the 90% confidence level of 2.64×10^{-5} (using the Barlow method) and 3.10×10^{-5} (using the Feldman-Cousins method). The theoretically predicted branching fraction is $(7.9 \pm 1.9) \times 10^{-7}$ [17]. A limit on the branching fraction of $B^{-} \rightarrow \Lambda\overline{p}\nu\overline{\nu}$ has never been experimentally measured before.

Given the success of this sensitivity study we intend to continue and improve this analysis, with the eventual aim of publication as a *BABAR* analysis. Our result is, however, limited by the size of the *BABAR* dataset. Future B factories, such as BelleII, will provide larger datasets and thus the opportunity for more stringent limit setting.

Bibliography

[1] S. Agostinelli et al. Geant4 — a simulation toolkit. *Nuclear Instruments and Methods in Physics Research A*, 505:250-303, 2003.

[2] J. Allison et al. Geant4 Developments and Applications. *IEEE Transactions on Nuclear Science*, 53:270-278, 2006.

[3] W. Altmannshofer et al. New strategies for new physics search in $B \to K^* \nu\overline{\nu}$, $B \to K\nu\overline{\nu}$ and $B \to X_s\nu\overline{\nu}$ decays. *Journal of High Energy Physics*, 04:022, 2009.

[4] ATLAS Collaboration. Observation of a new particle in the search for the Standard Model Higgs boson with the ATLAS detector at the LHC. *Physics Letters B*, 716:1-29, 2012.

[5] B. Aubert et al. (BaBar Collaboration). The BABAR detector. *Nuclear Instruments and Methods in Physics Research A*, 479:1-116, 2002.

[6] B. Aubert et al. (BaBar Collaboration). The BABAR detector: Upgrades, operation and performance. *Nuclear Instruments and Methods in Physics Research A*, 729:615–701, 2013.

[7] R. Barlow. A calculator for confidence intervals. *Computer Physics Communications*, 149:97-102, 2002.

[8] J. Beringer et al. (Particle Data Group). The Review of Particle Physics. *Physical Review D*, 86:010001, 2012.

[9] G. Buchalla, A.J. Buras, M.E. Lautenbacher. Weak decays beyond leading logarithms. *Reviews of Modern Physics*, 68:1125, 1996.

[10] CMS Collaboration. Observation of a new boson at a mass of 125 GeV with the CMS experiment at the LHC. *Physics Letters B*, 716:30-61, 2012.

[11] A. Cho. Higgs Boson Makes Its Debut After Decades-Long Search. *Science*, 337:141-143, 2012.

[12] T.G. Dietterich, G. Bakiri. Solving Multiclass Learning Problems via Error-Correcting Output Codes. *Journal of Articial Intelligence Research*, 2:263-286, 1995.

[13] J. Ellis. *Standard Model of Particle Physics* in P. Murdin (editor) *Encyclopedia of Astronomy & Astrophysics*. Nature Publishing Group (Basingstoke) and Institute of Physics Publishing (Bristol), 2001.

[14] G.J. Feldman, R.D. Cousins. Unified approach to the classical analysis of small signals. *Physical Review D*, 57:3873, 1998.

[15] G.C. Fox, S. Wolfram. Event shapes in e^+e^- annihilation. *Nuclear Physics B*, 149:413-496, 1979.

[16] P.J. Fox. *Supersymmetry and the MSSM* in C. Csaki and S. Dodelson (editors) *Physics of the Large and Small TASI 2009*. World Scientific Publishing (Singapore), 2011.

[17] C.Q. Geng, Y.K. Hsiao. Rare $B^- \to \Lambda\overline{p}\nu\overline{\nu}$ decay. *Physical Review D*, 85:094019, 2012.

[18] D. Griffiths. *Introduction to Elementary Particles*. Second edition. Wiley-VCH (Weinheim), 2008.

[19] P. Higgs. Broken Symmetries and the Masses of Gauge Bosons. *Physical Review Letters*, 13:508-509, 1964.

[20] D.J. Lange. The EvtGen particle decay simulation package. *Nuclear Instruments and Methods in Physics Research A*, 462:152-155, 2001.

[21] J. P. Lees et al. (BaBar Collaboration). Measurement of branching fractions and rate asymmetries in the rare decays $B \to K^{(*)}\ell^+\ell^-$. *Physical Review D*, 86:032012, 2012.

[22] J. P. Lees et al. (BaBar Collaboration). Search for $B \to K^{(*)}\nu\overline{\nu}$ and invisible quarkonium decays. *Physical Review D*, 87:112005, 2013.

[23] D. Lindemann, *The Search for Rare Non-hadronic B-meson Decays with Final-state Neutrinos using the BABAR Detector*. Thesis, McGill University, 2012.

[24] O. Long. *Search for the forbidden decay $B^\pm \to K^\pm\tau\mu$*. Internal BaBar Analysis Document #1732 version 9, 2008.

[25] B.R. Martin. *Nuclear and Particle Physics*. John Wiley & Sons (Chichester), 2006.

[26] U. Sarkar. *Particle and Astroparticle Physics*. Taylor & Francis (Boca Raton), 2008.

[27] T. Sjöstrand, S. Mrenna, P. Skands. PYTHIA 6.4 physics and manual. *Journal of High Energy Physics*, 5:26, 2006.

[28] http://www.slac.stanford.edu/BFROOT/www/Detector/Images/peprings.gif. Accessed 2014-05-16.

[29] K.G. Wilson, W. Zimmermann. Operator Product Expansions and Composite Field Operators in the General Framework of Quantum Field Theory. *Communications in Mathematical Physics*, 24:87-106, 1972.

Appendix A

Signal selection optimisation

A.1 B-mode purity cut optimisation

As mentioned in Section 5.1.2, to determine the value of the cut on B-mode purity we plot B-mode purity after B_{tag} m_{ES}, continuum likelihood and E_{extra} cuts (see Figure A.1.1a) and then plot the ratio, on a bin-by-bin basis, of signal MC to background MC (see Figure A.1.1b).

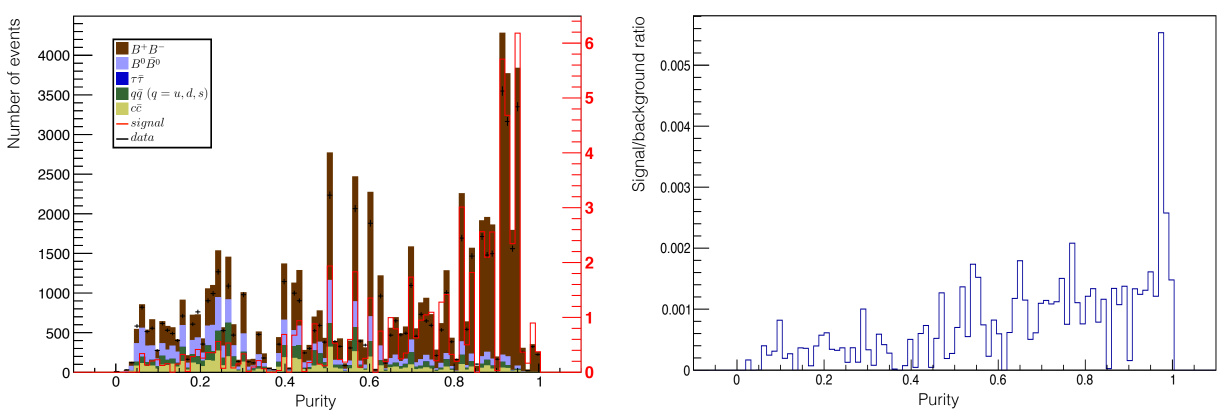

(a) *B-mode purity after cuts on m_{ES}, continuum likelihood and E_{extra}.*

(b) *The ratio of signal MC to background MC in Figure A.1.1a on a bin-by-bin basis.*

Figure A.1.1: B-mode purity cut optimisation histograms.

Although there is no mathematically obvious place to cut on B-mode purity, an examination of both histograms suggests a cut of > 0.4 improves our signal/background ratio and preserves a large proportion of signal MC.

A.2 Continuum likelihood cut optimisation

As described in Section 5.2.1, we optimise the value of the continuum likelihood cut by performing a nominal full signal selection and varying the value of the continuum likelihood cut, using branching fraction upper limit as a figure of merit. The results of this exercise are shown in Figure A.2.1.

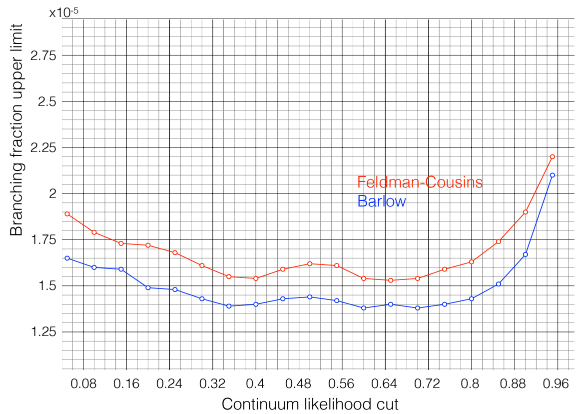

Figure A.2.1: Branching fraction upper limit according to Barlow and Feldman-Cousins techniques after a full signal selection as a function of continuum likelihood cut. For details on branching limit calculation techniques see Section 6.2.

As we can see both Barlow and Feldman-Cousins techniques give us a minimum estimated upper limit on the branching fraction when the value of the continuum likelihood cut is between approximately 0.6 and 0.7. Consequently, a cut value of > 0.65 was chosen.

A.3 E_{extra} cut optimisation

As described in Section 5.2.2, we optimise the value of the E_{extra} cut by performing a nominal full signal selection and varying the value of the E_{extra} cut, using branching fraction upper limit as a figure of merit. The results of this exercise are shown in Figure A.3.1.

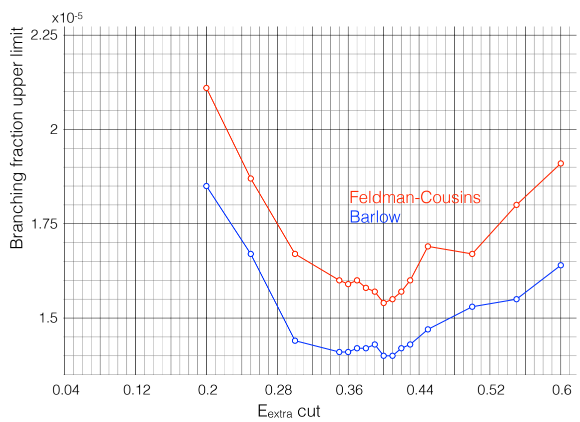

Figure A.3.1: Branching fraction upper limit according to Barlow and Feldman-Cousins techniques after a full signal selection as a function of E_{extra} cut. For details on branching limit calculation techniques see Section 6.2.

Appendix B

Definition of E_{extra}

As mentioned in Section 5.2.2, E_{extra} is defined in this analysis using cluster energies adjusted by $-5\,\mathrm{MeV}$ (with a minimum permitted cluster energy of $0\ \mathrm{MeV}$). Ordinarily one would use unadjusted cluster energies to calculate E_{extra}. The reasons for our choice of adjusted cluster energies will be explained in this appendix.

Figure B.1a shows E_{extra} when calculated using unadjusted cluster energies (which we will refer to as "unadjusted E_{extra}" for the remainder of this appendix), while Figure B.1b shows E_{extra} when calculated using clusters adjusted by $-5\,\mathrm{MeV}$ ("adjusted E_{extra}").

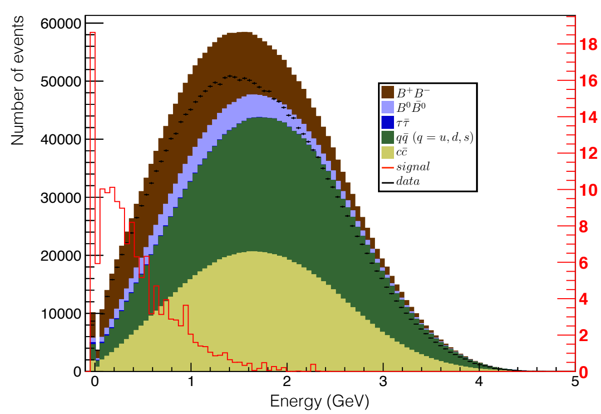

(a) *Unadjusted E_{extra}, calculated using unadjusted cluster energies.*

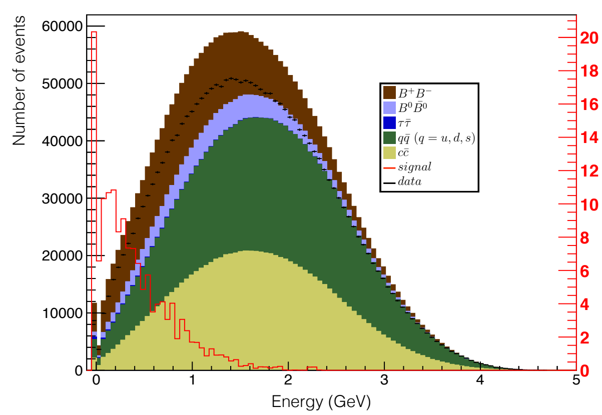

(b) *Adjusted E_{extra}, calculated using cluster energies adjusted by $-5\,\mathrm{MeV}$*

Figure B.1: Unadjusted and adjusted E_{extra} after local-skim and B_{tag} m_{ES} cuts.

Any differences between the two definitions of E_{extra} are, at this stage, difficult to see, although a higher number of events in lower bins is visible in adjusted E_{extra} compared with unadjusted E_{extra}. The reason for concern, when looking at unadjusted E_{extra}, is the considerable disagreement between data and MC. Although this disagreement is visible in many variables in this analysis, it is particularly concerning in the case of E_{extra} as the agreement is much better at lower values of E_{extra} ($\lesssim 0.4\,\mathrm{GeV}$). Thus, when a cut of $< 0.4\,\mathrm{GeV}$ is placed on E_{extra} this greatly enhances the agreement between data and MC in the remaining events.

Superficially this may appear to be a desirable effect; however, given the large change in data/MC agreement and its heavy dependence on the choice of E_{extra} cut it is important that we understand whether this change is a genuine physics phenomenon or simply a fluke thanks to our choice of E_{extra} cut.

To better understand the MC/data disagreement we plot unadjusted E_{extra} after an m_{ES} sideband substitution (see Section 5.3 for details). The result is shown in Figure B.2a. Although the MC/data agreement is much improved after the implementation of the m_{ES} sideband substitution, it is still still far from satisfactory. Furthermore, the fact that MC appears to be underestimating the data across almost the entire distribution suggest the m_{ES} sideband substitution has not worked correctly.

m_{ES} sideband substitutions work best when the correction they have to apply is small and when there is a “well-behaved” B_{tag} m_{ES} distribution; that is, an m_{ES} distribution with a flat combinatorial tail, a prominent B meson peak and a small number of combinatorial events. Other than the B_{tag} m_{ES} cut itself the only other cuts used in FigureB.1a are the local-skim cuts, therefore the corresponding B_{tag} m_{ES} distribution is that shown in FigureB.2b; this is clearly not well-behaved.

In order to provide a more well-behaved B_{tag} m_{ES} distribution we plot unadjusted E_{extra} again, but after local-skim, B-mode purity and continuum likelihood cuts. The relevant B_{tag} m_{ES} distribution is shown in FigureB.3c. Although the combinatorial tail is far from flat, the B meson peak is considerably more prominent and the cut on continuum likelihood has reduced the number of

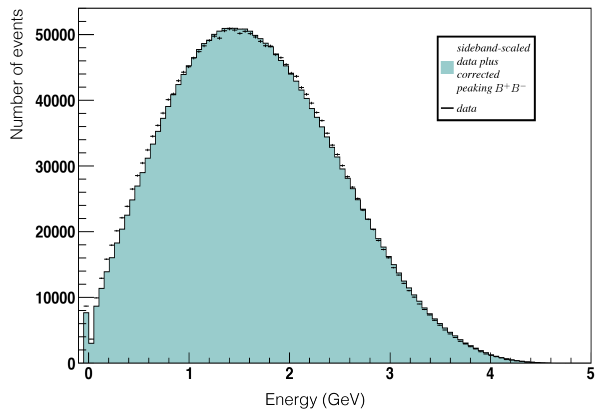

(a) *Unadjusted E_{extra} after m_{ES} sideband substitution and after local-skim and B_{tag} m_{ES} cuts.*

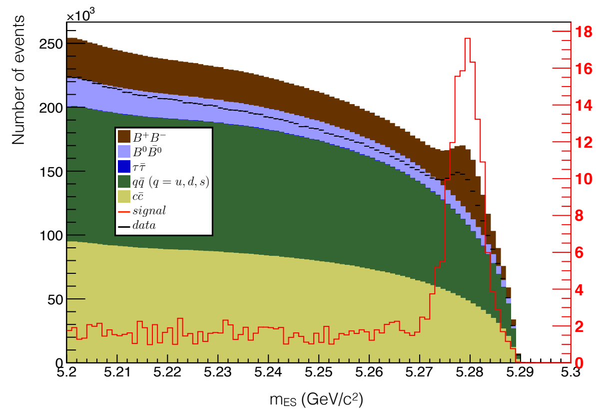

(b) *Corresponding B_{tag} m_{ES} distribution, after local-skim cuts only.*

Figure B.2: Unadjusted E_{extra} after m_{ES} sideband substitution and corresponding B_{tag} m_{ES} distribution.

combinatorial events.

Unadjusted E_{extra} after local-skim, B-mode purity and continuum likelihood cuts and before and after m_{ES} sideband substitution are shown in Figure B.3a and Figure B.3b. In terms of magnitude the agreement between data and MC in Figure B.3b is not much different than in Figure B.2a; however, the fact that MC now underestimates data in lower bins but overestimates in higher bins suggests that the sideband substitution is now working but that the MC and data distributions do not match across the E_{extra} spectrum.

To correct for this we adjust cluster energies when calculating E_{extra} by $-5\,\mathrm{MeV}$ and $-10\,\mathrm{MeV}$. The results, along with sideband-substituted versions, are shown in Figure B.4.

Figure B.4a shows that adjusted (by $-5\,\mathrm{MeV}$) E_{extra}, after a sideband substitution, corrects the overestimation by MC seen in the lower bins ($\lesssim 1\,\mathrm{GeV}$) of Figure B.2a while maintaining a relatively good agreement over the rest of the distribution. The agreement is not perfect, and there is a small overestimation by MC in some of the lowest-energy bins. Adjusting by $-10\,\mathrm{MeV}$, shown in Figure B.4d, overcompensates for the corrections needed to Figure B.2a, as can be seen in the most of the bins below $\sim 1\,\mathrm{GeV}$, where MC underestimates data.

We therefore consider adjusted (by $-5\,\mathrm{MeV}$) E_{extra} to be the best estimation of the three options presented here (unadjusted, adjusted by $-5\,\mathrm{MeV}$, and adjusted by $-10\,\mathrm{MeV}$), allowing us to achieve

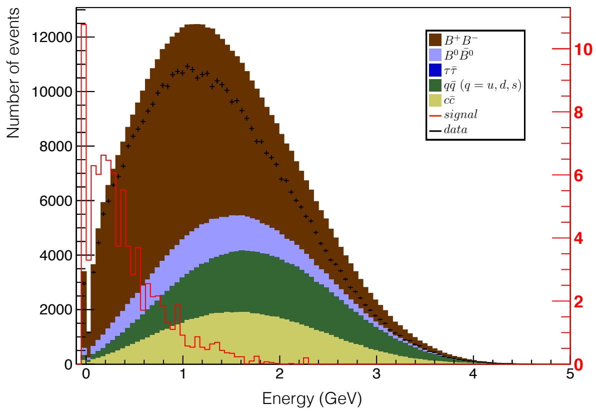

(a) *Unadjusted E_{extra} after local-skim, $B_{\rm tag}$ $m_{\rm ES}$, B-mode purity and continuum likelihood cuts.*

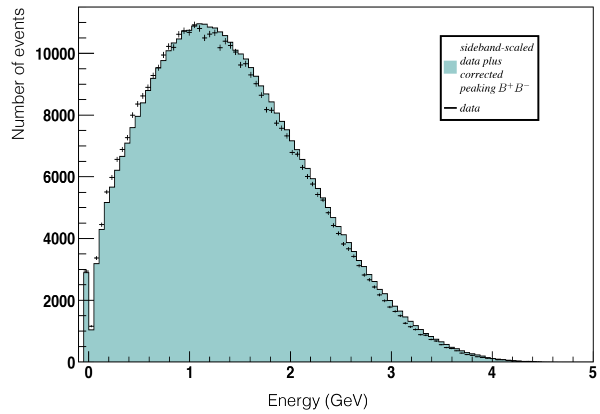

(b) *Unadjusted E_{extra} after $m_{\rm ES}$ sideband substitution and after local-skim, $B_{\rm tag}$ $m_{\rm ES}$, B-mode purity and continuum likelihood cuts.*

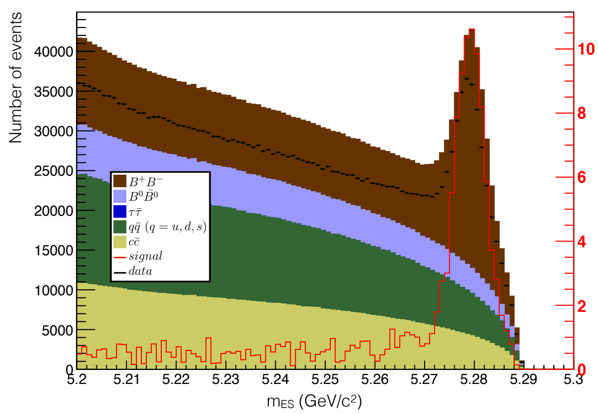

(c) *$B_{\rm tag}$ $m_{\rm ES}$ after local-skim, B-mode purity and continuum likelihood cuts.*

Figure B.3: Unadjusted E_{extra}, after local-skim, $B_{\rm tag}$ $m_{\rm ES}$, B-mode purity and continuum likelihood cuts, before and after $m_{\rm ES}$ sideband substitution; and corresponding $B_{\rm tag}$ $m_{\rm ES}$ distribution.

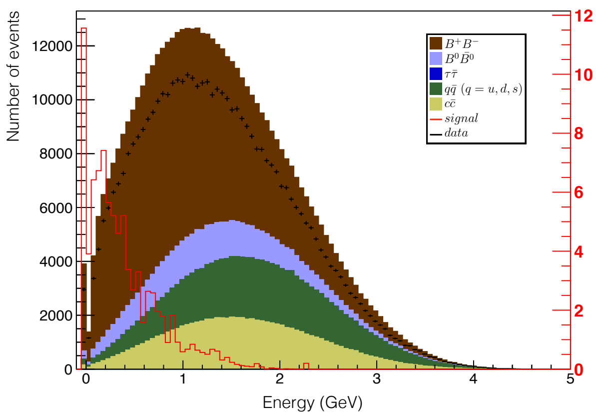

(a) E_{extra} *adjusted by* $-5\,\mathrm{MeV}$ *after local-skim,* $B_{\rm tag}$ $m_{\rm ES}$*, B-mode purity and continuum likelihood cuts.*

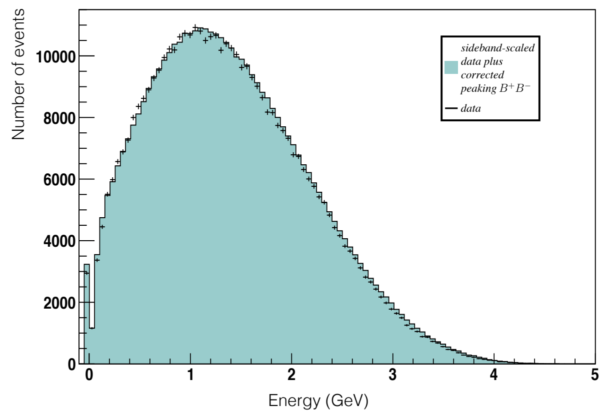

(b) E_{extra} *adjusted by* $-5\,\mathrm{MeV}$ *after* $m_{\rm ES}$ *sideband substitution and after local-skim,* $B_{\rm tag}$ $m_{\rm ES}$*, B-mode purity and continuum likelihood cuts.*

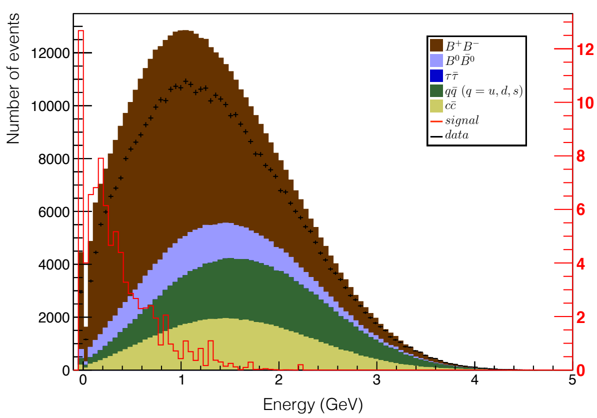

(c) E_{extra} *adjusted by* $-10\,\mathrm{MeV}$ *after local-skim,* $B_{\rm tag}$ $m_{\rm ES}$*, B-mode purity and continuum likelihood cuts.*

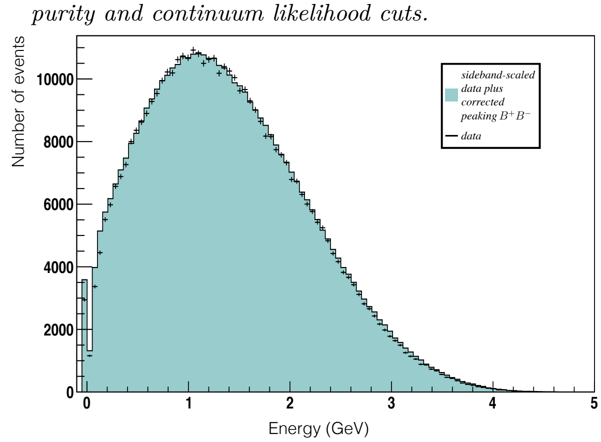

(d) E_{extra} *adjusted by* $-10\,\mathrm{MeV}$ *after* $m_{\rm ES}$ *sideband substitution and after local-skim,* $B_{\rm tag}$ $m_{\rm ES}$*, B-mode purity and continuum likelihood cuts.*

Figure B.4: E_{extra} *adjusted by* $-5\,\mathrm{MeV}$ *and* $-10\,\mathrm{MeV}$*, and* $m_{\rm ES}$ *sideband-substituted versions.*

the best agreement between MC and data. We therefore use adjusted E_{extra} in our analysis. Differences between E_{extra} adjusted by $-5\,\mathrm{MeV}$ and unadjusted E_{extra}, and between E_{extra} adjusted by $-5\,\mathrm{MeV}$ and E_{extra} adjusted by $-10\,\mathrm{MeV}$ are used to determine a systematic error on our E_{extra} cut (see Section 6.1.6).

Appendix C

Lambda reconstruction using less stringent particle identification

As explained in Sections 5.2.3 and 5.2.4 the lambda reconstruction process we use requires an event to pass two PID tests; that is, the KMTightProton PID test must be passed twice by particles of appropriate charge to identify the two protons in a signal event. We will call this method "2PID".

It is possible to reconstruct a Λ mass peak using less stringent PID requirements which we will call "1PID" and "0PID". Both of these methods were investigated but found not to be competitive with 2PID and hence were not used.

The results of Λ reconstruction using 2PID (without DOCA) are shown in Figure C.1 for comparison with the results of 1PID and 0PID.

1PID

The 1PID method is used on any event which fails to pass the 2PID cut, or which passes the 2PID cut but fails the m_Λ cut. In the 1PID method we use the proton PID selector KMTightProton to identity a proton track amongst the three charged tracks in our final state and also require that this track has the same charge as the B_{sig}. This particle is then presumed to be the daughter of

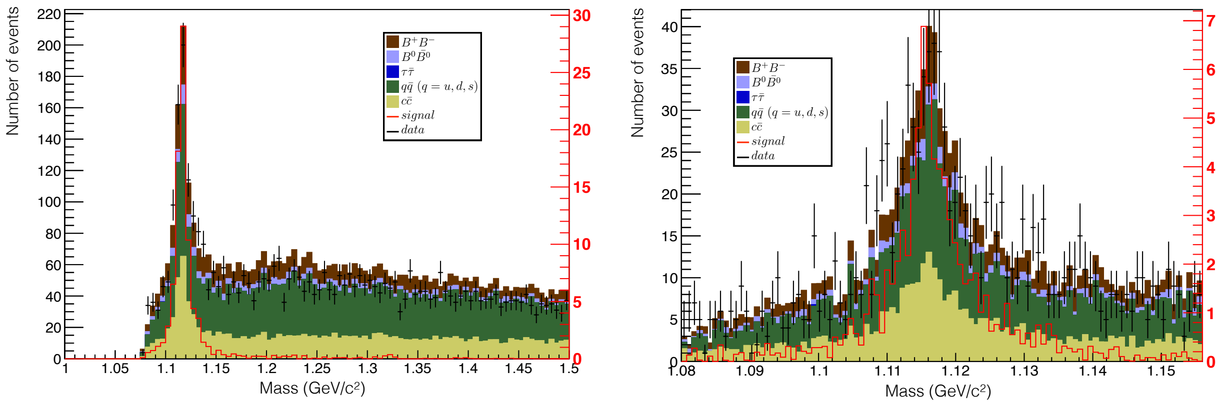

(a) Λ *mass peak with combinatorial tail.*

(b) Λ *mass peak.*

Figure C.1: Λ *mass after reconstruction using the 2PID method and after local-skim and* B_{tag} m_{ES} *cuts.*

the B_{sig}.

The other charged particle in the event which has the same charge as the B_{sig} is presumed to be the $\pi^{\pm}$ daughter of the Λ. The final charged particle in the event, which must have a charge opposite that of the B_{sig}, is presumed to be the proton daughter of the Λ. Once masses have been assigned we reconstruct a Λ mass; the results are shown in Figure C.2.

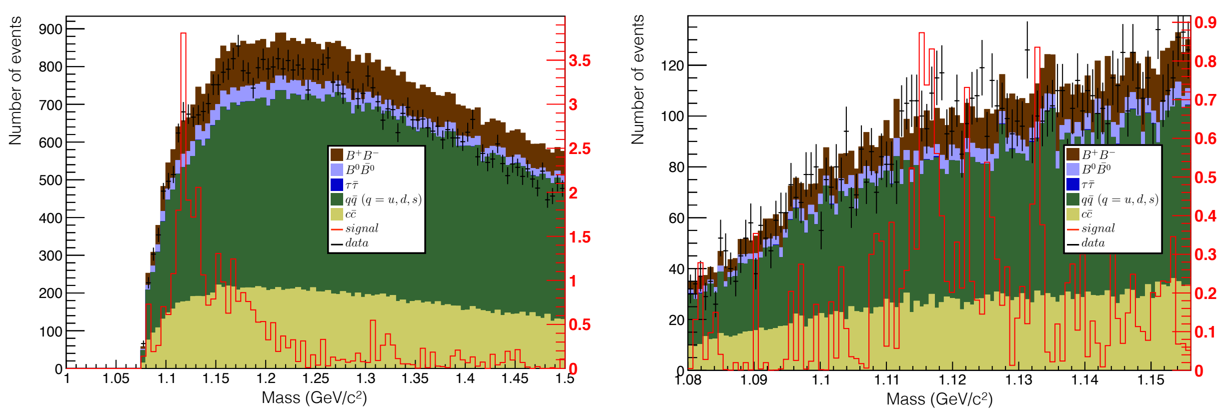

(a) Λ *mass peak with combinatorial tail visible in signal MC but not background MC.*

(b) Λ *mass peak visible in signal MC only, and less clean than that produced by 2PID (Figure C.1b).*

Figure C.2: Λ *mass after reconstruction using the 1PID method and after local-skim and* B_{tag} m_{ES} *cuts.*

By comparing Figure C.2 with Figure C.1 we can see that 1PID's performance is not comparable to that of 2PID. Although a Λ mass peak is visible in signal MC it is completely absent in background MC. Furthermore, the signal/background ratio is much lower than when using 2PID so even if we accepted the events in the m_{Λ} peak region we would be adding a considerable number of background events to our analysis for only a very small gain in signal efficiency.

0PID

The 0PID method is used on any event which fails to pass the 2PID and 1PID cuts, or which passes the 1PID cut but fails the m_Λ cut. In a signal event there are three charged tracks in the final state. Since we start with a charged B meson, the charges of the three final-state charged particles will be $++-$ or $--+$; i.e. there will be two like-charged tracks and one uniquely-charged track. In a signal event the uniquely-charged track must be the proton which is the daughter of the Λ, and is presumed to be so.

We then combine the four-vector of the presumed proton with the four-vectors of each of the two remaining charged tracks individually, creating two candidate Λ four-vectors per event. If the mass of only one of these Λ candidates passes the m_Λ cut then it is chosen as the Λ. If neither of the candidate Λ's pass the m_Λ cut then the event is excluded from the analysis - it has failed Λ reconstruction. If both the Λ candidates pass the m_Λ cut then the one with the mass closest to the PDG Λ mass is chosen; although this creates a bias in favour of "good" Λ masses the number of events in which this occurs is very low and, in any case, the 0PID method is not used in the final signal selection. The results of Λ reconstruction using 0PID are shown in Figure C.3.

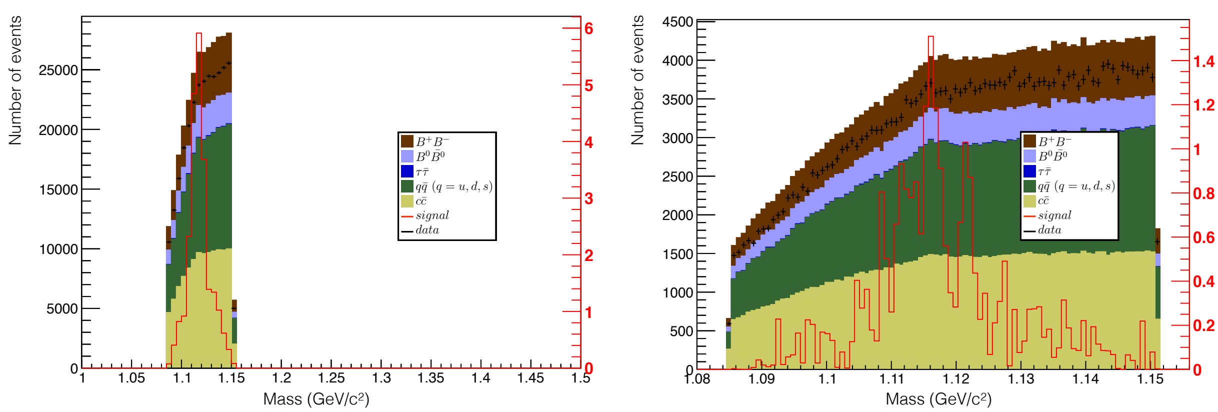

(a) Λ *mass peak visible in signal MC but not background MC.*

(b) Λ *mass peak visible in signal MC only, and less clean than that produced by 2PID (Figure C.1b).*

Figure C.3: Λ *mass after reconstruction using the 0PID method and after local-skim and* B_{tag} m_{ES} *cuts. Note that the requirement to choose a* Λ *candidate for each reconstruction using 0PID means there is no combinatorial tail to the right of the* Λ *peak.*

By comparing Figure C.3 with Figures C.2 and C.1 we can see that 0PID underperforms both 1PID and 2PID. As with 1PID, there is no Λ peak visible in background MC, and the signal/background ratio is even worse than in 1PID. The reason for the higher number of signal MC events in 0PID than 1PID is that 0PID produces a Λ reconstruction for every single event which is passed to it (with the exception of the handful of events which produce two Λ candidates both of which fail the m_Λ cut) after having failed 2PID and 1PID. However, it also produces Λ candidates for every single background event passed to it, many of which will pass the m_Λ cut despite not containing a real Λ baryon, hence the extremely low signal/background ratio and the lack of a Λ peak in background MC.

DOCA

It is possible to incorporate DOCA into both 1PID and 0PID in the same way as for 2PID (see Section 5.2.5). This was investigated and although it yielded a slight improvement of the performance of the 1PID and 0PID methods, they were still not competitive with 2PID.